SAPIENZA
Università di Roma
Facoltà di Farmacia e Medicina

Ph.D. in
MORPHOGENESIS AND TISSUE ENGINEERING

XXXVIII Ciclo
(A.A. 2024-2025)

SOLAR LIGHT-RESPONSIVE NANOMATERIALS FOR REUSABLE BIOMEDICAL APPLICATIONS

Ph.D. Student
Federica Zaccagnini

Tutor
Prof. Luciano De Sio

Coordinator
Prof. Antonio Filippini

Tutor esterno
Dr. Francesca Petronella

CONFIDENTIALITY NOTICE

Reviewers and PhD committee members are obliged to keep the files confidential and to delete all records after completing the review process.

Il ricevimento degli elaborati scientifici, per l'ottenimento del titolo di Dottore di Ricerca, in qualità di Membro del Collegio dei Docenti del Dottorato in Morfogenesi ed Ingegneria Tissutale richiede di osservare le seguenti normative:

i. considerare le Informazioni confidenziali e riservate come strettamente private e ad adottare tutte le ragionevoli misure finalizzate a mantenerle tali;

ii. utilizzare le Informazioni confidenziali e riservate unicamente allo scopo per le quali sono state fornite o rese note, impegnandosi a non divulgarle a soggetti terzi le informazioni contenute negli elaborati ricevuti;

iii. a garantire la massima riservatezza, anche in osservanza alla vigente normativa in materia di marchi, di copyright e di brevetti per invenzioni industriali e in base alla normativa sulla privacy, ai sensi del D.Lgs. 196/2003, riguardo il know-how e tutte le informazioni acquisite, che non potranno in alcun modo, in alcun caso e per alcuna ragione essere utilizzate a proprio o altrui profitto e/o essere divulgate e/o riprodotte o comunque rese note a soggetti terzi.

Index

1. Summary

Main issue: With the rapid growth of the field of nanobiophotonics, researchers have explored the development of resonant light-responsive nanomaterials for various biomedical applications, including pathogens disinfection, energy conversion and sensing. Thanks to the tunable properties of plasmonic nanoparticles, it is possible to realize exotic nanomaterials to further enhance their light harvesting capabilities and energy conversion efficiency. This thesis aims at demonstrating that the development of hybrid plasmonic nanostructures responsive to white and solar light can solve the challenges related to environmental pollution and health risks associated with the use of nanomaterials in healthcare applications.

Results: In this thesis, we first depict the structure and preparation of plasmonic hybrid nanostructures, which are arranged to enhance the optical features compared to those of their constituent individual nanoparticle. The crucial role of self-assembly and bottom-up deposition techniques is presented. The morphological, optical and photothermal characterizations highlight the specific features of the different systems properly designed for specific biomedical applications. After that, the consequently enhanced photothermal and photoelectric properties of the hybrid systems are investigated: they exhibit the improvements obtained by the coupling between the localized surface plasmon resonance phenomenon of single nanoparticles or by the surface lattice resonance phenomenon. To conclude, the hybrid nanostructures and their outstanding optical and morphological properties are exploited in different biomedical applications as white light-triggered devices. The disinfection of biomedical tools, the power supply of electronic devices, the construction of a smart reusable FFP2 face mask, and the realization of a highly sensitive biosensor are illustrated.

Conclusions: A comprehensive understanding of the capabilities of light-responsive plasmonic nanostructures is presented, highlighting the huge potential in solving healthcare challenges in

an environmentally sustainable, cost-effective, and affordable manner and improving the quality of life in less developed countries.

2. Introduction

2.1 Transforming healthcare through nanotechnology

Biophotonics is the science of using light to image, detect, and manipulate biological materials. Over the past two decades, nanomaterials have significantly advanced this field by improving the sensitivity, specificity, and durability of biotechnological tools. This field of research is called nanobiophotonics, a multidisciplinary discipline that focuses on nanomaterials, capable of absorbing, reflecting, and interacting with light, which is exploited in a wide range of applications and addresses critical issues related to safety and environmental risk.[1] Among nanomaterials, nanoparticles (NPs), ranging from 1 to 100 nm, are characterized by a high surface-to-volume ratio, giving them tunable mechanical, optical, photothermal, and electrical properties. Notably, plasmonic noble metal NPs (MNPs) are widely used due to their biocompatibility, stability, and cost-effectiveness. They play a major role in energy, environmental, and medical applications.[2] Despite the advantages brought by nanotechnology, current applications face substantial challenges, including technical issues and the strict regulations concerning the user and the environmental welfare that make these systems more complex and expensive.[3] The exploitation of renewable energy sources and the use of label-free, bottom-up techniques can facilitate a more sustainable development of nanotechnology, producing environmentally friendly, cost-effective, facile and highly efficient tools. Solar energy has attracted significant interest, as it can be harvested and converted into alternative forms of energy.[4] Plasmonic MNPs are promising candidates for solar energy conversion due to their large absorption cross-section, arising from the localized surface plasmon resonance (LSPR) phenomenon. They can convert solar energy into heat, electricity, and chemical energy via photothermal, photovoltaic (PV), and photochemical processes, respectively. They constitute a promising solution for a variety of applications ranging from photocatalysis to sensing,

bacteria-killing, and PV, emerging as an essential component in the fields of personalized medicine, energy, and information technology, with a low environmental impact. In recent years, the pivotal contribution of nanomaterials in biophotonics has completely revolutionized the field of healthcare, contributing to the development of nanomedicine and more efficient medical devices.

2.2 Plasmonic nanomaterials chemical-physical properties of biophysics interest

Plasmonic noble MNPs, such as gold (Au), silver (Ag), aluminium and platinum NPs, exhibit outstanding properties resulting from the so-called LSPR phenomenon.[5] LSPR refers to the collective oscillations of free electrons (plasmons) locally confined on the surface of MNPs interacting with the resonant incident light. This phenomenon leads to strong light scattering, produces intense surface plasmon absorption bands, and enhances the local electromagnetic fields. MNPs usually present their characteristic resonance frequency whose value depends on their constituent material, size, shape and their environmental medium. These peculiar optical features are reflected in the color of the respective colloidal dispersion, depending on the position of the resonance absorption band. Those colors have enchanted people for centuries, providing a valuable ingredient for ornamental decorations.[6] Nowadays, the extraordinary properties of these colloidal materials are widely investigated and exploited in a plethora of applications, including the biomedical field.[7] Among all the possible materials, Au, Ag and copper are commonly used metals for their applicability in visible or near-infrared (NIR) regions.[2] Furthermore, Au and Ag NPs exhibit attractive features for the biomedical sector. On the one hand, Au NPs are biocompatible, bioinert, and stable, with their friendly chemistry promoting the functionalization of their surface with biological molecules, making them fascinating for biomolecular sensing, delivery, or therapeutics.[8] According to their size and shape, the color of the

colloidal solution can be tuned from red to blue or purple, corresponding to plasmonic peaks at ~500 nm. On the other hand, Ag NPs are often involved in antibacterial and antiviral nanoformulations. Their surface oxidation and dissolution of Ag^+ ions cause low stability and toxicity effects. The colloidal dispersion color of those NPs can vary, changing their size and shape from yellow to blue, corresponding to plasmonic peaks at ~400 nm.[9] As a result, in addition to the different features given by the material composition of the NPs, their shape and size can further modify their optical properties.

Au and Ag nanospheres (NSs) exhibit a plasmonic dipole mode, as depicted in the model described by Mie theory.[10] It reveals that the absorption scales as r^3 for small particles ($r \ll \lambda$) dominating over the scattering contribution that scales as r^6 and that dominates, instead, for larger NSs. Indeed, for spheres having a size smaller than 15 nm, the light absorption becomes dominant, while for higher sizes, the scattering increases, becoming evident for 50 nm NSs and dominating for 100 nm NSs. The LSPR peak position red-shifts and broadens for larger NS sizes. Moreover, an Au NS size of 15/20 nm is ideal for maximising hot electron generation, as small NSs have high energy levels. MNSs are exceptional photo-thermal transducers converting the incident light into a heating effect.[11, 12] The generated heating depends on the absorption cross section; however the photothermal efficiency depends on the ratio of the scattering cross section to the absorption cross section. As a result, the total produced heat may be higher in larger NSs because they exhibit a higher absorption cross section, but the photothermal efficiency is lower due to the reduced absorption portion in the total extinction. However, the spherical symmetry of their geometry results in poor tunability of their optical properties, a feature highly demanded in practical bio-related applications, such as the detection of cancer cells or thermal treatment. For this reason, anisotropic geometries have been studied and realized. Au and Ag nanorods (NRs) are rod-like NPs that present two plasmonic bands described by the Gans theory[10] : the weak

transverse band (LSPRt) and the strong longitudinal one (LSPRl). As the aspect ratio, defined as the length-to-diameter ratio increases, the LSPRl linearly moves from the visible to the NIR range. The peculiar morphology of these NPs produces an enhancement of the electromagnetic field at the ends on the scale of over 10^3 times higher than that of NSs and an extremely large extinction cross section. As a result, the NR's linewidth is narrower, leading to a high quality factor, Q, defined as the ratio between the resonant peak wavelength and its full width at the half maximum. The light scattering decreases with higher aspect ratios while the absorption increases. These optical features can be synthetically controlled. Both Au NRs and Ag NRs present an excellent plasmonic heating effect due to their high absorption ratio (~90%).[13] The optical tunability, high sensitivity to changes in the surrounding medium, and the enhanced photothermal response make Ag NRs, especially Au NRs, functional materials in sensing, delivery, photothermal therapy, and imaging.[14, 15]

Au and Ag nanocubes (NCs) present a more sophisticated geometry. They show higher modes in addition to the dipole mode. For NCs having a smaller size than the wavelength of the incident light, the plasmon dipole mode prevails. However, for dimensions higher than 140 nm, these NCs can produce higher order plasmonic modes such as electric quadrupole or magnetic dipole modes. As a result, the optical spectrum shows multiple SPR peaks. This geometry is highly flexible. Raising the NC size or sharpening the corner leads to a red shift of the plasmon resonance and broadening of the peak. Moreover, they exhibit a greater intensity of the electromagnetic enhancement near the sharp edges and corners.[16]

Other geometries are available, such as nanocages or nanostars, that define their optical properties according to their selected morphology.[17]

Plasmonic NPs can be deposited and assembled on substrates to realize 2D plasmonic nanostructures and thus obtain compact, easy to use and efficient devices. Different techniques can be employed: lithography-based (top-down approach) and self-assembly-based

(bottom-up approach) methods.[18] The former ones exhibit high sensitivity but require high costs for the production process and maintenance. As a result, self-assembly methods are being widely investigated to overcome these limitations and achieve scalable production of the so-called plasmonic metasurfaces.[18] The ordered or disordered NPs array, constituting the meta-atoms, can be deposited on both dielectric and metal substrates. The arrangement of plasmonic NPs in a periodic lattice may encounter manufacturing issues. For this reason, disordered metasurfaces have garnered the attention of researchers. The local long-range coupling among plasmonic NPs gives rise to new hybridised modes, and their interaction with the substrate leads to the amplification of electromagnetic fields and reduced absorption losses. Considering the minimum distance among the NPs comparable to the incident radiation wavelength, innovative combinations of the materials are obtained. For example, the combination of thin metallic layers that produce the SPR mode with an array of plasmonic NPs that produce the LSPR mode gives rise to plasmonic surface lattice resonances (SLRs). SLRs exhibit narrower spectral line widths and high-quality factors.[19]

2.3 Biomedical technologies based on plasmonic nanomaterials

The described high quality plasmonic nanomaterials exhibit fascinating properties with significant potential in the biomedical field to address the issues presented by the conventional used techniques. The significant impact of nanotechnology in healthcare is discussed in the following paragraphs, considering some of the main applications and approaches, ranging from disinfection to energy conversion, innovative personal protective equipment (PPE) and sensing.

2.3.1 Disinfection

Pathogen disinfection is a crucial task to address to prevent healthcare issues in indoor facilities and prevent the spread of infectious diseases. Both the 2022 and 2024 Healthcare Cleaning

Forums have highlighted the tangible possibility of achieving automated disinfection, digitalization, and antimicrobial surfaces through the support of artificial intelligence, novel technologies, and materials.[20] Future initiatives should aim to realize sustainable and affordable procedures. The Covid-19 pandemic underlined the importance of environmental hygiene to preserve human safety hindering the viral spread through contact transmission. Consequently, antimicrobial mechanisms are widely investigated to construct reusable surfaces that could support and improve the routine cleaning procedures of healthcare structures and instruments.[21]

Disinfection procedures can be classified into two main categories: chemical and physical methods. The former ones involve the use of chemical agents, i.e. biocides or germicides, that are used to kill microorganisms by interfering with their essential enzymes. The drawbacks of chemical disinfection methods include the safety risks to users and materials, as chemical agents can cause skin and mucosal irritation, unpleasant odours, flammability, and corrosion or deterioration of metals. Furthermore, prolonged exposure to chemical disinfectants contributes to the development of antimicrobial resistance, a severe threat to public health.[22] The environmental impact of residual disinfectants also becomes an increasing concern. In contrast, physical disinfection methods such as thermal treatment (e.g. autoclaving, pasteurization) and ionizing/non-ionizing radiation (e.g. gamma rays, ultraviolet UV-C light) can eliminate microorganisms, producing irreversible structural and molecular damage.[23] These methods are usually free of chemical residues and reduce the risk of resistance development. However, physical methods often require significant energy input, specialized equipment, safety controls as well as specialized staff rising the costs and limiting their accessibility. Hybrid physical-chemical disinfection technologies such as ozonation, chlorine dioxide treatment, UV/H_2O_2 oxidation[24], Fenton and photo-Fenton reactions[25], and semiconductor-based photocatalysis[26] rely on the generation of reactive oxygen species (ROS) and superoxide

anions (O_2^-).[27] Despite their high disinfection efficiency, they still require high energy input and chemical reagents or catalysts, limiting the scalability of the procedure and rising the environmental impact.

The concept of thermal disinfection was revolutionized by Louis Pasteur in the 19th century, demonstrating the efficacy of controlled heating in eliminating pathogens in clinical and food environments.[27] Recent advancements in nanotechnology have enabled the development of MNPs as photothermal agents. Noble MNPs, usually Au and Ag NPs, exhibit the thermoplasmonic effect whereby incident light of a specific resonant wavelength is converted into localized thermal energy. When irradiated, these NPs produce highly localized heating capable of inducing hyperthermia resulting in protein denaturation, membrane disruption and microbial inactivation.[28] This process minimizes damages to surrounding materials and allows the spatial and temporal control of disinfection. Additionally, such nanomaterials can be functionalized with bio-entities for targeted treatments enhancing their practical utility. This is a sustainable and cost-effective physical method that benefits from the versatility of the plasmonic nanocompounds.[29] Researchers have investigated the effectiveness of photothermal disinfection treatment using different types of plasmonic NPs. It is worth noting that, due to varying size, shape, and composition, the light-to-heat conversion efficiency can be improved and modified. Au NPs are often selected because of their biocompatibility and stability. Moreover, while Au NSs exhibit strong absorption in the visible range, anisotropic Au NPs, such as Au NRs, show enhanced absorption in the NIR range, allowing for greater penetration into tissues.[30] As a result, Au NRs have been widely used to realize nano-devices for photothermal disinfection. Indeed, Fang et al. embedded Au NRs in an optically transparent and non-toxic silicone polymer, polydimethylsiloxane, to create microfluidic channels with high photothermal performance and achieve water photothermal disinfection.[31] To achieve better antibacterial properties hybridized Au

nanostructures were realized combining the stability of Au NPs with the antibacterial properties of Ag NPs. Zhang et al. constructure Au@Ag core-shell NPs with different thickness of Ag layer. They find out that 5 nm of shell thickness exhibit the best antibacterial performances with great biocompatibility.[32]
The evolution of disinfection technologies reflects a continuous balancing between efficacy, safety, cost and environmental impact. The integration of nanomaterials holds significant promise for the development of next-generation disinfection systems. These emerging technologies not only address the limitations of traditional approaches but also align with global priorities related to antimicrobial management, sustainability, and public health protection.

2.3.2 Energy conversion

The World Health Organisation (WHO) has declared that the consequences on human health of the climate change represent an urgent task to be addressed and promotes environmental sustainable practices to prepare for health risks associated with the climate change and energy crisis.[33] Similarly, 2024 Healthcare Cleaning Forums have highlighted the crucial importance of environmental sustainability in all health and care settings. Some strategies to mitigate the health impact aim to the modernization of facilities with new ecological technologies.[34] To overcome the issues related to fossil fuel dependence for energy supply, which has led to climate change and air pollution, renewable energy sources are becoming essential. PV systems can convert solar light into electricity, obtaining an eco-friendly, renewable and abundant energy source. Among existing technologies, expensive silicon-based solar cells exhibit the highest efficiencies (15-24%). However, a plethora of different alternatives provide PV systems with lower costs and easier production processes. However, they are still hardly affordable, such as semiconductor-based thin-film solar cells that achieve an efficiency of ~20%. Novel approaches are the object of research for sustainable, low-cost, and high-

efficiency devices. Even if these emerging concepts still do not fulfil all the requirements to enter the market, the most attractive option is the perovskite PV cells that exhibit the highest energy conversion efficiency of 26.1% [35], low cost and affordable production process. Despite their exceptional performance, they still present structural issues due to the high instability of perovskites, sensitive to multiple environmental factors, thus preventing their trade. Also dye-sensitized solar cells (DSSCs) are valuable devices offering unique opportunities with a versatile, facile and low-cost production process, eco-friendly materials and the capability of harnessing energy even under low light intensity conditions.[36] These devices exploit photosensitized agents to absorb light, namely organic dyes. The excited electrons are then injected into the conduction band of a semiconductor layer. Their main drawbacks involve the short-term stability of the organic dyes which compromises the entire mechanism. For these reasons, several studies are devoted to strengthen the performance of existing PV technologies.

Plasmonic NPs possess great potential in this field, due to their LSPR phenomenon that boost the light absorption and the charge transfer processes in the PV cells. Indeed, latest research focuses on the improvement of the perovskite solar cells' energy conversion efficiency by integrating MNPs. Both the LSPR effect and the improved crystallization of the perovskite films boost their stability and performance.[37]

Several studies reported the efficacy of MNPs incorporated into the semiconductor of DSSCs taking advantage of the versatility of their optical properties based on their chemistry, size and shape. Indeed, the combination of sensitizer dyes with bare MNPs, core-shell MNPs or ion-implanted MNPs in DSSCs have been investigated and have highlighted a great enhancement of the DSSCs efficiency.[38] Despite the achievements of these studies, organic dyes still exhibit high instability over time and easy degradation. Yen-Hsun Su et al. have reported in 2012 the construction of plasmon-sensitized solar cells (PSSCs) composed

of an active anode whose sensitizer agent are Au NPs instead of organic dyes. The Au NPs were deposited through the bottom-up Layer-by-Layer technique, reaching an efficiency of $\eta = 0.016\%$ for a single Au NPs layer and of $\eta = 0.750\%$ for five Au NP layers.

2.3.3 Innovative personal protective equipment

The production of PPE is a constantly developing sector. The goal is to protect people from various hazards as far as possible by developing novel strategies based on the combination of multiple disciplines, such as materials science, textile engineering, and medical science.[39] PPE equipped with mechanical, thermal, electric or chemical functional materials were introduced in recent years and still great efforts are devoted for novel materials and advanced PPE designs. Covid-19 pandemic has further stressed PPE crucial role in controlling viral transmission. Among various protective measures, face masks became essential tools in reducing airborne spread in public and indoor environments. In particular FFP2 respirators, due to their 94% filtration efficiency, offers significant protection against airborne pathogens such as viruses and bacteria according to the EN149 regulation.[40]

In response to WHO guidelines mandating the use of masks, face mask production in Europe increased by a factor of 20 compared to pre-pandemic levels. To enhance the comfort and functionality of the face masks, advanced novel materials were incorporated into the fabrication process. Multifunctional devices were realised, integrating energy harvesters for the power supply of electronic devices or biosensors for healthcare monitoring of the wearer or of the environment. Indeed, the face mask structure and design are optimised to isolate the virus, avoiding inhalation; however, the pathogens remain stuck on the outside of the face mask, causing potential infections to the wearer. For this reason, FFP2 face masks must be changed daily or more frequently once their fibres become contaminated or damaged. They are composed of multiple plastic fibres, such as polypropylene PP and polyethene PE which make the face masks difficult to dispose of, contributing to

environmental pollution. As a result, sensing mechanisms and disinfection procedures were widely investigated.
Different approaches and technologies have been employed to mitigate the environmental impact and the related toxic effects.[41] Biodegradable materials have been employed to realize sustainable, skin-friendly and antimicrobial face masks.[42] However, those materials present structural issues that make it difficult to reduce the pore size and enhance the filtration efficiency against pathogens. Additionally, thermoplastic materials can be recycled through mechanical, thermal and chemical processes that present significant financial barriers and require complex instruments as well as specialized staff.[43] Commonly used techniques employed for face masks disinfection involve organic solvents, UV radiation, hydrogen peroxide steam and hot water. The latter one is the most user-friendly technique for home settings involving a 30 min immersion in hot water and a subsequent drying step, crucial for maintaining the ability to trap pathogens through the recovered electrostatic charge. The reusability is assured after 10 cycles of the treatment.[44] A comparison of the commonly employed disinfection techniques was reported by Liao et al. evaluating the filtration efficiency after the treatments.[45] As an example, UV light exposure exhibits excellent disinfection capability but also damaging the treated materials. Then, the best approach was the heating treatment that present a filtration efficiency ≥95% after 20 cycles including temperatures close to 100°C. In such a context, MNPs have proven essential to the evolution of the thermal method. The photothermal properties of Au and Ag NPs rising from the LSPR phenomenon are widely investigated to ameliorate and further the thermal pathogens killing on face masks. The strongly localized heating close to the NPs surface promotes a targeted and enhanced photothermal treatment. Moreover, Au and Ag are also ideal candidates for bio-related applications (see **Section 2.3.2**) avoiding the use of organic solvents. As a result, researchers have further investigated the Au and Ag NPs involvement in face mask disinfection. Functionalization of the

face masks with MNPs is a commonly employed strategy to exploit their multiple features. Valdez-Salas et al. promoted the decontamination process of a surgical face mask by impregnating it with Ag NPs exploiting their antimicrobial properties.[46] De Sio et al. demonstrated the capability of a face mask functionalized with Au NRs to reach high temperatures when irradiated under a proper NIR laser source, thereby achieving thermal pathogen disinfection.[47] Indeed Bayan et al. exploited the electrospinning technique to functionalize a surgical face mask with Au NRs to obtain a self-sterilizing device under the proper NIR light irradiation and added PAN electrospun nanofibers to improve the bacterial filtration efficiency.[48]
Noble MNPs can be used to realize novel materials and structures to be introduced in PPE. Their versatility and excellent properties can improve the PPE performances such as for shielding pathogens and for disinfection capabilities. Despite the huge possibilities, there are still some concerns involving the durability of the protection performances with the applied disinfection techniques and the costs required for production and maintenance processes.

2.3.4 Metasurface-based biosensor

Metasurfaces are 2D metamaterials composed of a rational assembly of nanostructures (meta-atoms) in a specific in-plane arrangement. They possess unique optical properties resulting from the arrangement of meta-atoms and their stimuli-responsiveness, as well as their chemical structure. Metasurfaces' optical range spans the entire electromagnetic spectrum. They are realised through top-down methods that confer extreme precision with high production process and maintenance costs, or bottom-up methods that are suitable for the scalability of the devices. Plasmonic optical metasurfaces are composed of ordered or disordered MNPs arrays distributed on a metallic substrate. The rising SLR modes[19] exhibit extraordinary sensitivity to variations in the metasurfaces' structural parameters, such as the meta-atoms' shape, size, and constituent material, their interparticle distance, the dielectric

spacer height between the atoms and the substrate, and the substrate thickness. Metasurface structures with different designs are constructed and compared to calculate the quality factor of the fundamental gap mode. For example, Rozin et al. have investigated how the shape of the nanocrystals affects the overall metasurface efficiency.[49] Comparing the effect of NSs, nanooctaedra and NCs array they found out the highest efficiency factor in the case of NCs due to the well-defined parallel cavity formed with the metal substrate. For this reason, NCs are often selected to construct highly efficient metasurfaces.[50, 51] In addition to the metasurfaces' versatility due to the tunability of their optical properties through structural changes, these devices exhibit tunable SLR modes that can shift according to the variation of the metasurface's surrounding medium. These unique optical properties of metasurfaces make them ideal candidates in biosensing applications. Researchers have widely exploited the high sensitivity of these optical devices to realize highly efficient biosensors. A biosensor can detect a target, an analyte molecule, through its specific interaction with the recognition element that undergoes a variation of its physical or chemical properties such as refractive index, pH value and so on. The use of a transducer enables the conversion of this variation into a readable electrical, thermal, piezoelectric or optical signal.[52] The versatility of metasurfaces enables multiple readout methods. As an example, LSPR-based technique is used to realize plasmonic sensors, namely plasmonic metasurfaces. Ordered and non ordered metasurfaces show wide applicability in fabricating biosensors for health and environmental monitoring. These miniature devices ensure high levels of sensitivity and selectivity, multiplexing capabilities along with real-time responsiveness.

Wang et al. realized plasmonic metasurfaces for the detection of lung tumor markers in serum.[53] They demonstrated the enhanced sensitivity of high-roughness Au nanohole metasurfaces decorated with Au nanobumps. The platforms are constructed through nanoimprint lithography. The presence of Au nanobumps

introduces a red shift of the starting plasmonic resonance wavelength. Both bulk and surface refractive index sensitivities reach higher values compared to low-roughness metasurfaces, making the former ones ideal candidates for immunosensing. Indeed, label-free immunosensing of three different tumor merkers for early diagnosis lung cancer, was conducted at different concentrations measuring the corrisponding wavelength dip shift. The superior sensitivity of high-roughness metasurfaces enables clinical serum sample detection even below the clinical diagnosis threshold.
Qiu et al. realized Au nanoisland chips through thermal dewetting. The bottom-up self-assembly technique produced a highly sensitive device capable to detect bioaerosols once it is covalently bioactivated with succinimidyl-ester groups. This system enables both SERS and immune-LSPR analyses for the detection of different bioaerosols. The improved sensitivity of this device compared to the bare Au platform (SPR sensing) has been proved. The calibration of the device was performed at first with standard bacteria strains and then the real applicability of the sensor was tested by analysing real-word environmental aerosol samples.[54]

2.4 Broadband light-responsive nanostructures for wide-ranging biomedical applications

Inexhaustible energy sources play a key role in tackling climate change and the energy crisis. For this reason, solar light conversion technologies are widely investigated and have become crucial in multiple healthcare-related fields to guarantee sustainable and efficient tools. The outstanding properties of plasmonic nanomaterials and nanostructures properly fit in this context, opening up new possibilities for photothermal, PV or photoelectric-derived applications. MNPs are an excellent choice as solar light absorbers because their resonance frequencies lay in the sunlight range (300-2500 nm) and in particular, Au and Ag NPs exhibit the greatest performance due to their large absorption cross sections that can further enhance broadband solar energy

conversion.[55] Researchers have explored different approaches to generate improved plasmonic devices for light harvesting. The first attempt involves the deposition of NPs or nanostructures array on dielectric or metallic substrates. These ordered or disordered plasmonic metasurfaces exhibit hybridized photonic-plasmonic modes (SPR) having narrower spectral line width and higher quality factors compared to the individual NP ones.[18] Different compositions, geometries and alignments of the meta-atoms can alter the resulting optical properties. Loeb et al. realized a photothermal film to improve the performances of a water heating treatment system. In this work, Au NRs and carbon black NPs were embedded in a transparent curable polymer, NOA-61, in direct contact with the flowing water channel. The enhanced solar light harvesting was sufficient to generate high temperature values sufficient for disinfection. Despite these great advancements, this technology still faces some challenges: the pivotal contribution of the carbon black double layer entails higher opacity that prevent a good light absorbance and optical output signal, and also the required high concentration of Au NRs leads to aggregates as well as high production costs. For this reason, researchers started to work on bimetallic NPs and on more exotic shapes in order to reach improved light conversion efficiencies of better plasmonic mata-atoms. Au and Ag were investigated as photothermal agents in an alloy or in core@shell structures.[56] The latter ones show better photothermal properties giving rise to further studies. Karam et al. investigate the photothermal properties of Au@Ag@Au core@shell@shell NPs under NIR irradiation.[57] This geometry enables a highly improved performance compared to the Au NR and Au NS ones. Hu et al. realized a NR-like Au@Ag@Au core@shell@shell structure with photothermal response highly better than Au@Ag NRs.[58] They prove the effective 100% bacterial killing of *E. coli* cells ($1x10^3$ cfu ml^{-1}) after 20 min of NIR laser irradiation with a Au@Ag@Au concentration of 10 μg ml^{-1}. A step forward was taken by Liu et al. that demonstrated the superior and excellent photothermal properties of hyperbranched

NPs, exceeding the spheroidal core@shell geometry.[59] They realized CAg@Au NPs having Ag NCs as a core and amino acid-encoded hyperbranched Au NRs as the shells. They present a photothermal efficiency of 87.28% under NIR irradiation and proven efficacy in photothermal therapy of tumors. As a consequence, these improved structural geometries are widely applied for solar light harvesting, with the material composition and shape according to the selected application. Yang et al. constructed spherical ternary core@shell nanostructures featuring a core of Ag NPs surrounded by a shell of TiO_2, decorated with Au NPs to enhance sunlight photocatalytic activity. Indeed, while the Au NPs improve the light absorbance in the visible and NIR range, Ag NPs reduce the charge recombination.[60]

3. Aims of the work

This doctoral project aimed to provide sustainable, easy to use, cost-effective and highly efficient nanotechnology tools to be used in different healthcare-related applications. To do so, hybrid nanostructures sensitive to broadband light sources such as white light lamp or solar light are constructed through label-free bottom-up techniques. The realized hybrid nanostructures present improved optical, photothermal and photoelectric performances compared to the individual MNPs constituting them. Reusable tools for biomedical applications are here presented:

i. Au NRs array used as a photothermal transducer for the white light-triggered disinfection of biomedical tools,
ii. Ag@Au core-shell NPs array deposited on semiconductor TiO_2 layer used as the counter electrode of innovative PSSCs,
iii. FFP2 face mask functionalized with Ag@Au core-shell NPs array for the white light-triggered disinfection of pathogens,
iv. Ag NCs array deposited on a Au thin layer to realize a highly sensitive optical metasurface for the specific recognition of pathogens.

The listed hybrid nanostructures present hybridized modes due to the local long-range coupling among plasmonic NPs and the amplification of electromagnetic fields due to the NPs interaction with the substrate. The versatile label-free bottom-up deposition methods produce dense and even distributions of MNPs on both rigid and flexible substrates.

Combining nanotechnology and biomedical research fields, this project aimed to highlight the significant contribution of broadband light-responsive plasmonic nanostructures as environmentally friendly, efficient and easy to use devices for healthcare related fields such as disinfection, energy supply and biosensing. This research is pioneering a new opportunity for healthcare facilities transforming the complicated and expensive laser driven techniques into sustainable and non-hazardous procedures. The

reported findings pave the way for a more sustainable, cost-effective and afforbable nanobiotechnology.

4. Results and discussion

4.1 Preparation and optimization of plasmonic nanostructures

This work relies on bottom-up and self-assembly methods for the construction of hybrid metal nanostructures and colloidal heterostructures. These label-free techniques were selected to guarantee the scalability of the devices, reduced costs and simple preparation procedures without altering the properties of the involved MNPs.

4.1.1 Gold nanorods array construction with optical and morphological characterization

The first hybrid plasmonic nanostructure that we illustrate in this work is the array of Au NRs deposited on rigid glass substrates. Au NRs were selected for their superior photothermal efficiency (near 100%), the high tunability of their optical properties, their friendly chemistry and biocompatibility that make them ideal candidates as light-responsive materials for biomedical application. The aim is to maintain and replicate the outstanding properties of the Au NRs colloidal solution also in the dry state. The electrostatic Layer-by-Layer (eLbL) assembly method was selected for the construction of the plasmonic platform to guarantee high sensitivity and high fill fraction values of the devices. It is a bottom-up technique that relies on the controlled assembly of individual components, namely NPs, obtaining reproducibility and scalability of the nanostructures. The high versatility of this technique enables the deposition of multiple MNPs with different geometries, sizes and constituent materials on different dielectric or metallic, rigid or flexible substrates simply by varying the duration of the immersive steps and the number of the polyelectrolyte layers.

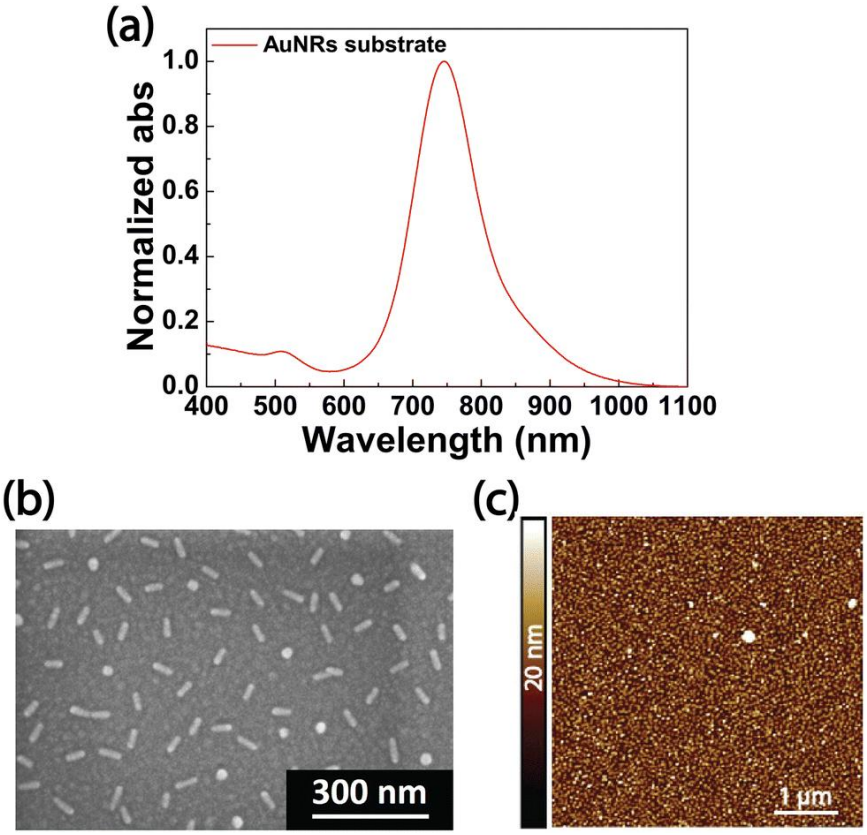

Figure 1: Morphological and optical characterization of Au NR plasmonic substrates. (a) Absorption spectrum of the Au NR substrates. (b) SEM of the Au NR substrates. (c) 2D AFM of the plasmonic Au NR substrates. Reproduced under terms of the CC-BY-NC 3.0 license. [61] 2023, Zaccagnini et al., published by Royal Society of Chemistry (RSC).

The first step in the eLbL assembly is the activation of a bare glass substrate through chemical etching. After that, the polyelectrolyte multilayer is constructed immersing the activated glass substrate in alternatively charged polyelectrolyte solutions, PAH (+) and PSS (-). As a result, PAH and PSS layers are sequentially deposited on the glass substrate (PAH-PSS-PAH). Employing a multilayer

system, rather than a single polyelectrolyte layer, has been shown to significantly increase the density of adsorbed NPs. This is due to both the enhanced surface roughness and the greater number of charged sites available for AuNR binding. Furthermore, the multilayer architecture benefits from the overcompensation effect, where each additional PE layer introduces excess surface charge, facilitating more efficient NP anchoring. The final overnight immersive step in Au NRs dispersion enables the AuNRs immobilization and thus confers the reddish hue to the plasmonic substrates that were arbitrarily realized 1 cm x 1 cm. Preliminary tests were performed using different Au NR concentrations. The deposition conditions were optimized selecting optical density O.D. of 1. Lower or higher concentrations led to poor coverage or aggregates. This saturation threshold depends on the PAH limited number of Au NRs that it can accommodate under the given conditions.

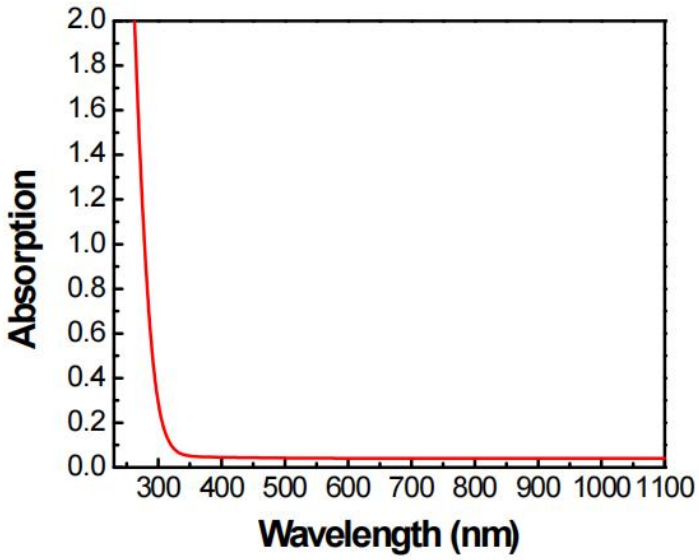

Figure 2: Absorption spectrum of a glass substrate using air as baseline. It shows intense absorption below 300 nm. Reproduced under terms of the CC-BY-NC 3.0 license. [61] 2023, Zaccagnini et al., published by Royal Society of Chemistry (RSC).

The optical characterization of the plasmonic platforms was performed through UV-visible absorbance spectroscopy. The absorption spectrum of the AuNRs substrate in **Figure 1a** clearly shows two peaks corresponding to the LSPRt and LSPRl plasmon modes rising from the LSPR phenomenon and due to their anisotropic shape. The LSPRl peak is more intense and centered at lower energies, at 764 nm while the LSPRt peak is located at 515 nm. The optical features of the Au NRs colloidal solution are almost perfectly transferred also to the dry state. The deposition of Au NRs array on the rigid glass substrate does not affect the optical and structural stability of the involved NPs. The absorption spectra were acquired using the glass substrate as the baseline. The polyelectrolyte multilayer contribute was negligible compared to the glass absorption below 300 nm (**Figure 2**) and did not affect the optical output.
The morphological characterization has been performed through Scanning electron microscopy (SEM) and Atomic force microscopy (AFM). SEM analysis of Au NR substrates (**Figure 1b**) reveals an even, dense and monodispersed distribution of plasmonic NRs revealing a fill fraction and an interparticle distance of 5.9% ± 0.3% and 120 nm ± 22 nm respectively. The absence of aggregates and the homogeneity of the distribution is attributed to the presence of the polyelectrolyte multilayer that provides a consistent surface charge across the glass substrate. The stretched conformation of the PAH facilitates the immobilization of AuNRs via electrostatic interaction between the positively charged amino groups of PAH and the negatively charged citrate-stabilized AuNR surfaces. The 2D AFM micrograph (**Figure 1c**) depicts a uniformly distributed topography, characterized by surface asperities with an average height of ~10 nm corresponding to the short axis of AuNRs and thus confirming the formation of a monolayer of AuNRs, mostly lying on the long side while a minority is vertically oriented as highlighted by the presence of spherical objects.

The sensitivity of these plasmonic substrates to the refractive index variation of their surrounding medium is investigated creating an ad hoc system.

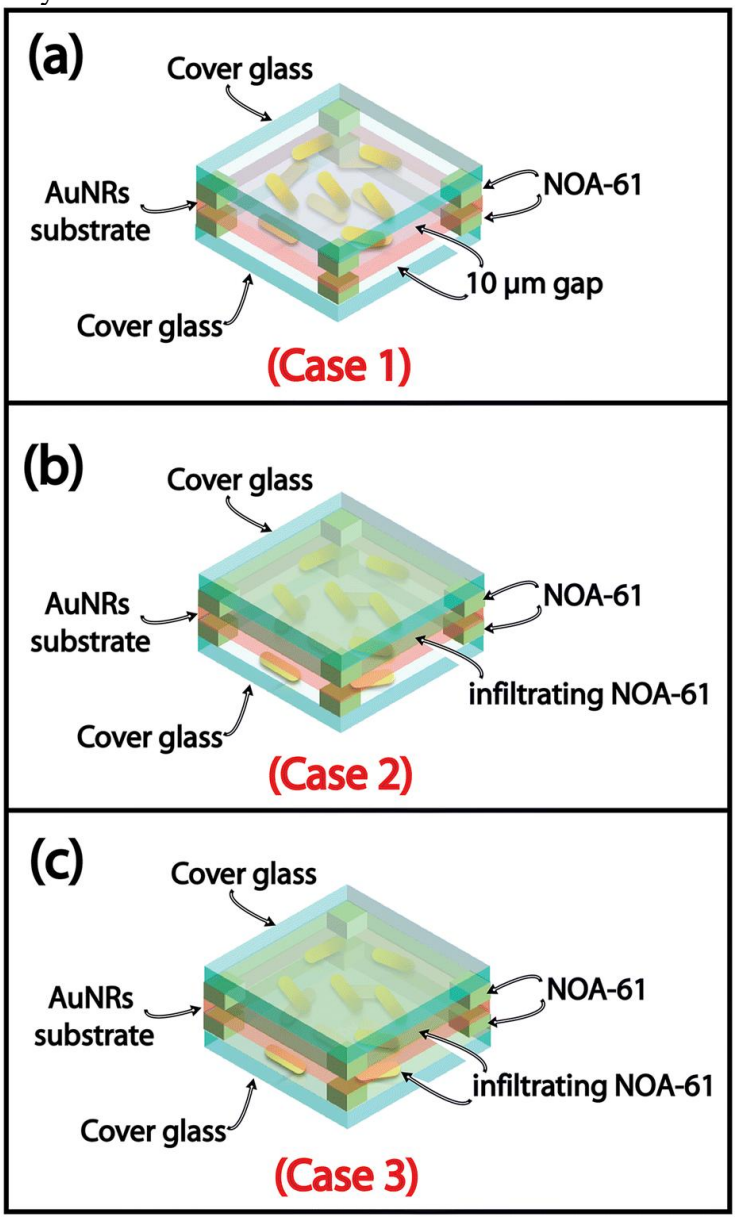

Figure 3: Schematic of the Au NR functionalized substrate with double sided glass cells for the sensitivity investigation to refractive index change. In Case 1 both the cells are empty (air, n~1). In Case 2 only one cell is filled with glue NOA-61 (n~1.56). In Case 3 both the cells are filled with glue NOA-61. The sample was optically characterized in each of these conditions. Reproduced under terms of the CC-BY-NC 3.0 license. [61] 2023, Zaccagnini et al., published by Royal Society of Chemistry (RSC).

In particular, the aim is to evaluate the effect of the immersive deposition method on both the sides of the functionalized substrate. For this reason, two glass cells are realized depositing a glass slide on each side of the plasmonic platform using 10 μm microbeads as spacers. **Figure 3** depicts the three different cases that were optically investigated. In the first case, the cells are left empty so that Au NRs substrate can feel the refractive index of air (n~1) on both sides. Subsequently, only one of the cells was filled with NOA-61. In this case, the plasmonic substrate can feel the refractive index of air on one side and of NOA-61 (n~1.56) on the other. In the third and last case, both the cells are filled with NOA-61, thus both the Au NRs substrate sides can feel the same refractive index of ~1.56. The UV-visible absorption spectra are collected in each configuration and overlapped (**Figure 4**). The absorption spectrum acquired for the Case 1, shows the LSPRl peak at 766 nm. This value is slightly redshifted of 14 nm for Case 2, when only one of the two sides feel a variation in the refractive index of the surrounding medium. Moreover, an evident shoulder appears at 882 nm. When both faces were infiltrated with NOA-61, the LSPRl peak completely redshifted of 118 nm. These data reveal that the absorption spectrum of the sample results from the combination of the contributions of both sides. The spectrum of Case 2 is the only configuration characterized by two different refractive indexes: the appearance of the shoulder reflects the optical output of the side in contact with NOA-61. Only when also the second glass cell is filled with the same compound, the LSPRl peak is completely redshift to 884 nm.

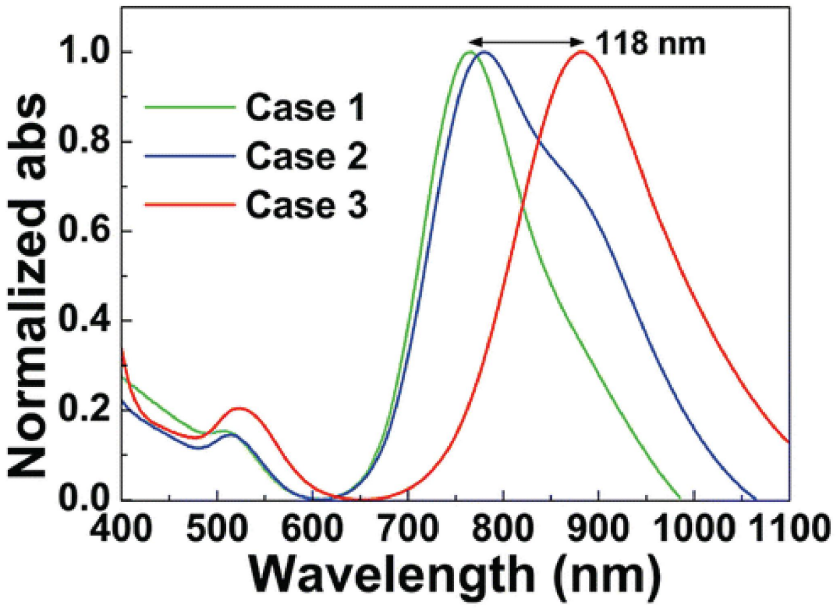

Figure 4: Optical characterization of Au NRs substrate investigated varying the experimental conditions depicted in Figure 3. The absorption spectra are overlapped to compare the LSPRl peaks. Reproduced under terms of the CC-BY-NC 3.0 license. [61] 2023, Zaccagnini et al., published by Royal Society of Chemistry (RSC).

4.1.2 Plasmonic hybrid heterostructures construction with optical and morphological characterization

Given the excellent optical features of Au NRs as optical absorber in the NIR range, a novel hybrid heterostructure was conceived to extend its optical response also in the visible range. Inspired by the work of Liu et al.[59] , a hyperbranched core@shell geometry was designed to preserve the optical features of the individual components, achieve broadband absorption to consequently

enhance the photothermal efficiency compared to the individual components and guarantee chemical stability.

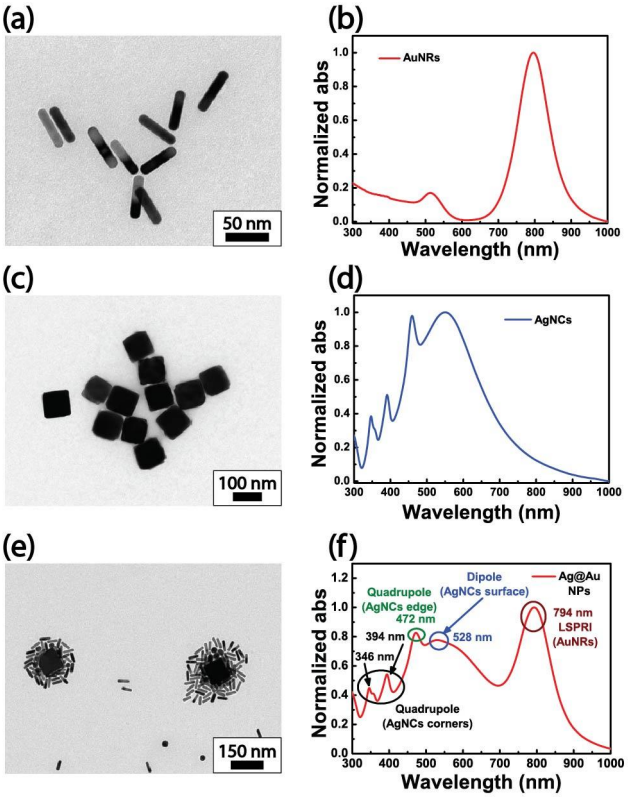

Figure 5: Morphological and optical characterization of the Au NR, Ag NC and Ag@Au NP dispersions. (a, c, e) TEM micrographs and (b, d, f) optical absorption spectra of the colloidal dispersions are shown. Reproduced with permission. [62] 2024, Wiley-VCH GmbH.

To do so, Au NRs and Ag NCs were selected to combine their morphological and optical characteristics. The morphological properties of Au NRs are examined through transmission electron microscopy, TEM (**Figure 5a**). The measured length and the width sizes of the Au NRs are 47.5 nm ± 3.2 nm and 11.2 ± 1.0 nm

respectively. The resulting high aspect ratio of 4.24 ± 0.66 was purposely selected to obtain high sensitivity and thus high tunability of the optical features according to the surrounding medium changes. This feature is highly demanded for the optical analysis of the heterostructure occurrence. The optical spectrum of the Au NRs dispersion (**Figure 5b**) presents the LSPRt and the more pronounced LSPRl at 513 nm and 793 nm. Ag NCs were used as the core of the hybrid heterostructure: their anisotropic shape produces interesting optical properties and the high contact of their faces boosts the Au NR bondings. TEM micrograph (**Figure 5c**) reveals the size of the NCs of 95 nm ± 5 nm with a slight deformation of ~4%. The optical absorption spectroscopy (**Figure 5d**) depicts the dipolar contribution related to the cubes' sides with a peak at 570 nm and the quadrupolar contribution of the corners and edges with peaks at 472 nm, 394 nm and 346 nm. The final optimized hybrid heterostructures are depicted in the TEM micrograph of **Figure 5e** where the distinguishable nanostructures are composed by the Ag NC as a core, surrounded by several layers of Au NRs assembly. It is worth noting that the majority of Au NRs relies on their long side. The combination of the two species not only enables to collect the wavelengths of the visible and NIR ranges but, at the same time, the optical response of the heterostructure reveals the mutual interaction between them. **Figure 5f** shows the absorption spectrum of the realized Ag@Au NPs pointing out that the optical features of the two species are still visible. The Au NRs LSPRl peak is located at 794 nm while the LSPRt peak is not visible because it is embedded in the dipolar mode of the Ag NCs (related to the facets of the NCs), visible at 528 nm with an evident distortion that suggests the interaction between the Au NRs and Ag NCs. The quadrupole peaks are still visible at 472 nm (related to edges of the NCs) and at 394 nm and 346 nm (related to the corners of the NCs).

Sample label	*Ag@Au_1*	*Ag@Au_2*	*Ag@Au_3*
Au:Ag volume ratio	0.5	2	1
Au:Ag OD ratio	0.6855	1.981	1.287
Au:Ag nanoparticle ratio	1.753	175.3	87.64
Au:Ag mass ratio	0.411	1.645	0.822

Table 1: Ag:Au volume ratios investigated to optimize the hybrid heterostructure colloidal solution. OD, volume and NP ratios were calculated for each value. Reproduced with permission. [62] 2024, Wiley-VCH GmbH.

The final protocol for the construction of the hybrid heterostructures was obtained optimizing the volume of the Au NRs to add to a defined volume of Ag NCs. Three different attempts were produced, namely Ag@Au_1, Ag@Au_2 and Ag@Au_3. The resulting Au:Ag volume ratios of 0.411, 1.645 and 0.822 are schematized in **Table 1** and correspond to distinct spectroscopic properties. **Figure 6a** shows the overlapped absorption spectra of the Ag@Au_1, 2 and 3. We could identify Ag@Au_3 as the optimized heterostructures considering its condition of iso-absorption (Au:Ag OD ratio of 1.287) and the nearly equally contributes of Au NRs and Ag NCs to the total mass (54.9% and 45.1% Au). **Figure 6b** highlights the quadratic growth of the OD as a function of the mass ratio in the various attempts.

Samples (dilution volumes)	**Zeta Average (nm)**	**PDI**	**ZP (mV) Vol.50_650 H_2O.**
AuNRs peak 1	2.07 ± 0.03	0.45	-21.10 ± 0.7
AuNRs peak 2	41.4 ± 0.1	0.45	-21.10 ± 0.7
AgNCs	161 ± 6	0.03	-20.97 ± 0.84
AuNRs + AgNCs	154 ± 3	0.03	-26.97 ± 3.19

Table 2: DLS measurements performed on Au NR, Ag NC and Ag@Au NP colloidal dispersions. The low values of the polydispersity index assess the

goodness of the obtained data. Reproduced with permission. [62] 2024, Wiley-VCH GmbH.

Ag@Au_3 was further examined comparing its DLS analysis with the bare Au NRs (**Figure 6c**) and Ag NCs (**Figure 6d**). The hydrodynamic diameters were 161 nm ± 6 nm and 154 nm ± 3 nm for Ag NC and Ag@Au NP (**Figure 6e**) dispersions (see **Table 2**). Their hydrodynamic sizes are comparable because, for geometrical reasons, the equivalent sphere of Ag NCs (**Figure 7**, on the left) and Ag@Au NPs (**Figure 7**, on the right) are expected to have a comparable hydrodynamic radius (R_H). However, the variation of the radius (R_M) of an equivalent sphere with the same mass specific volume rises from the bare Ag NCs to the Ag@Au NPs. The intensity peak values of the latter two mentioned colloidal dispersions are of 21.3 a.u. and 23.4 a.u. These values are highy higher than the intensity peak corresponding to the Au NRs dispersions; indeed, the reduced dimensions of the NRs do not permit the proper detection producing low scattering intensity.[63]

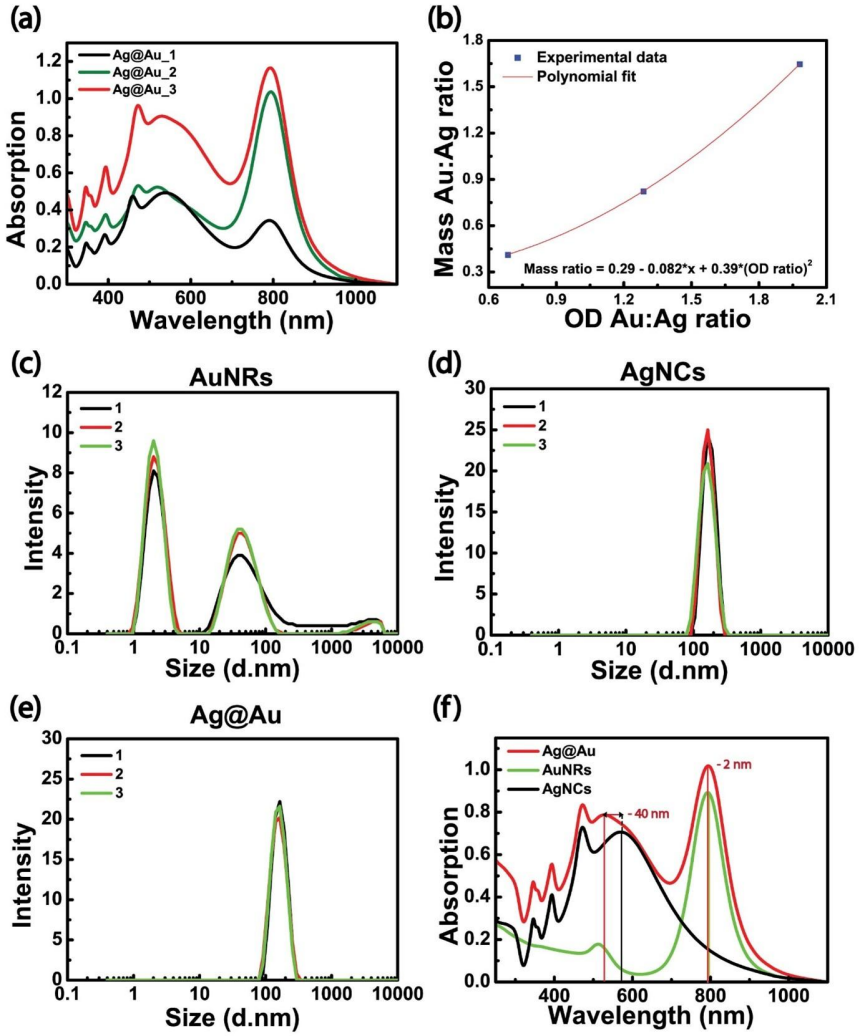

Figure 6: Optical characterization and DLS analysis of the dispersions having different Au:Ag mass ratios. (a) Absorption spectra of the colloidal solutions having Au:Ag mass ratios of 0.411, 1.645 and 0.822. (b) Mass Au:Ag ratio as a function of the OD Au:Ag ratio. (c, d, e) DLS measurements of the Au NRs, Ag NCs and Ag@Au NPs. (f) Overlapped absorption spectra of the Au NR, Ag NC and Ag@Au NP colloidal dispersions. Reproduced with permission. [62] 2024, Wiley-VCH GmbH.

Figure 6f illustrates the overlapping of the absorption spectra of the Au NR, Ag NC and Ag@Au NP colloidal dispersions to better visualize the similarities and differences in the heterostructure optical properties compared to the dispersions of the individual species. Compared to the optical features depicted in **Figure 5b** and **5d**, the LSPRl position of Au NRs has a blue shift of ~2 nm, the dipole peak of Ag NCs has a blue shift of 40 nm while the quadrupole peaks do not vary their positions. These data suggest that the Au NRs on the Ag NC facets produce an alteration of the optical features highlighting the occurring interaction between the Au NRs and Ag NCs. Moreover, the blue shift of the LSPRl peak of Au NRs is consistent with a side-by-side assembly where the Au NRs assembly occurs along the length of the NPs[64, 65] as already shown by the TEM micrograph of **Figure 5e**.

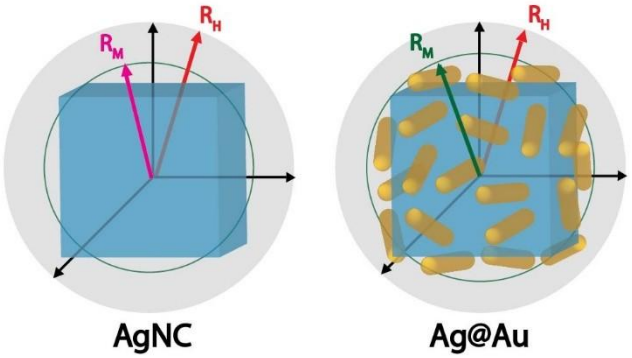

Figure 7: Schematics of the equivalent spheres in DLS measurements for bare Ag NCs (on the left) and Ag@Au NPs (on the right). Reproduced with permission. [62] 2024, Wiley-VCH GmbH.

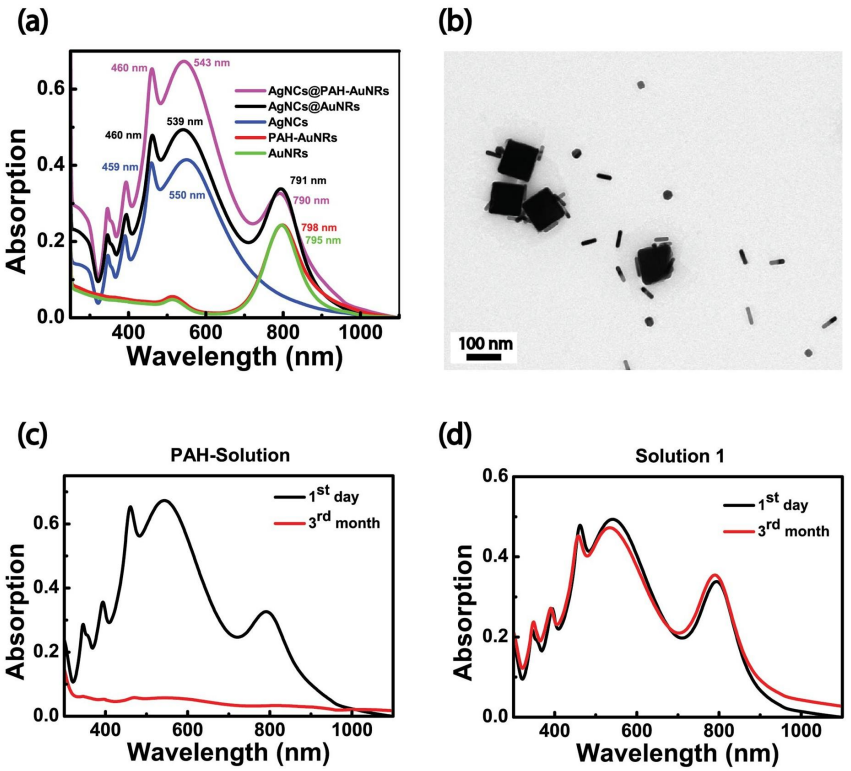

Figure 8: Optical and morphological characterization of the PAH-functionalized dispersions for electrostatic enhancement. (a) Absorption spectra of Au NR, PAH-Au NR, Ag NC, Ag@Au NP, Ag@PAH-Au NP colloidal dispersions. (b) TEM micrograph of the Ag@PAH-Au NPs. Stability of the optical features of the (c) Ag@PAH-Au NP and (d) Ag@Au NPs collecting the absorption spectra the first day and after three months after the production process. Reproduced with permission. [62] 2024, Wiley-VCH GmbH.

The assembly of the Au NRs on the Ag NCs facets can be attributed to Van der Waals forces interactions between the citrate ions of the stabilizing agent on the Au NRs and the PVP on the Ag NCs surface. The dipole-dipole interactions occur between the intense dipole associated to the citrate molecules, deprotonated at pH 7,[66] and the dipole of the lactam rings of the PVP. The

absorption spectroscopy supports this hypothesis since the spectrum of the heterostructures (**Figure 8a**, black curve) presents a significant contribute of the Au NRs, exceeding the one of the individual Au NRs dispersion (**Figure 8a**, green curve). The enhancement of the electric field is a direct consequence of the attraction among Au NRs guided by Van der Waals forces. Since the negative zeta potential values of both the Au NRs and Ag NCs dispersions are of -21 mV and -20 mV respectively (**Table 2**), the hypothesis of an electrostatic binding isn't supported. Indeed, several attempts are here presented to verify the possibility to realize an equivalent heterostructure exploiting electrostatic interactions. To do so, the cationic polyelectrolyte PAH was selected as a linker between negatively charged NPs. It was used to functionalize the Au NRs. Consequently, the absorption spectrum of Ag@PAH-Au NPs (**Figure 8a**, pink curve) shows a 8 nm blue-shift of the LSPRl peak compared to the PAH-Au NRs one (**Figure 8a**, red curve). The blue-shift suggests the Au NRs assembly along their long sides. However, the Ag NCs dipole peak does not appear distorted since the presence of the PAH alters the steric footprint of the Au NRs, preventing the assembly of more layers on the Ag NCs surface due to the charging repulsions among the PAH surrounding the Au NRs. The TEM analysis in **Figure 8b** supports this statement as it shows an abundance of Au NRs as isolated NPs and few of them bound to the Ag NCs surface mainly along their long side. Stability tests were performed by collecting the absorption spectra of the Ag@PAH-Au NP and Ag@Au NP dispersions the first day and three months after the preparation process. The spectra of the Ag@PAH-Au NPs in **Figure 8c**, clearly demonstrate that the geometric structure tends to collapse assessing that the introduction of PAH leads to temporal instability. On the contrary a more stable configuration is observed without the PAH addition. **Figure 8d** highlights the temporal stability of Ag@Au NPs dispersion. Furthermore, the zeta potential measurement on Ag@Au NPs dispersion further confirms the high

stability of the hybrid heterostructures that reaches -26.97 mV ± 0.84 mV (**Table 2**).

4.1.3 Hybrid heterostructures array deposition for plasmon-sensitized solar cells with optical and morphological characterization

The exceptional improvement carried out by the hybrid heterostructures in terms of broadband light absorption, distinguishable optical features and stability over time finds application in many different biomedical fields involving the exploitation of broadband light sources. Among them, the construction of a PV system is of primary importance to promote environmentally sustainable practices to prepare for health risks associated with the climate change and energy crisis. In light of this background, we aim to realize innovative, sustainable, highly efficient, affordable and stable PSSCs, taking advantage of the outstanding optical properties of the Ag@Au NPs dispersion. The structure of the PSSCs is inspired by the equivalent structure of DSSCs (**Figure 9a**): a working electrode (anode) with an embedded photosensitized layer is sealed with a counter electrode (cathode) to be filled with a redox-mediator (electrolyte). As a control experiment and to compare the functioning of the PSSCs, the DSSCs are realized using the organic dye Rhodamine B (RhB) as photosensitizer agent. It exhibits an absorption depth at 548 nm enabling the absorption of visible light (**Figure 9b**). Moreover the RhB dye confers a pink hue to the final DSSC (insert in **Figure 9b**).

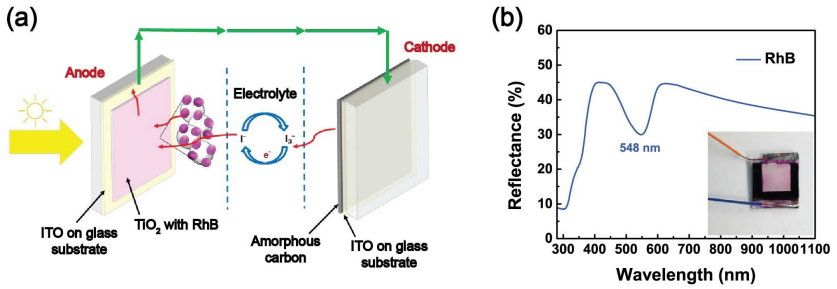

Figure 9: DSSC mechanism. (a) Schematic of the DSSC functioning. (b) Absorption spectrum of the organic dye RhB with representative photo as the inset.

In this work the commonly employed organic dyes, that are easily degradable over time, are substituted by the hybrid heterostructures, more efficient and stable over time, to form the photosensitized layer. To do so, the first main step of this work is the fabrication of the Ag@Au NPs-functionalized anode. An ITO substrate was used as support, properly chosen for its high visible light transparency (>80%) and electrical conductivity. On the top, an adhesive tape was used to delineate the borders of a sufficiently large square area and then a thin layer of the semiconductor TiO_2 [67] was spread over the entire squared area by a rolling motion of a glass pipette. The sample was stored for 15 min on a heating plate at 70 °C to dry and then the tape was removed. In order to achieve an even and dense distribution of Ag@Au NPs on the thin TiO_2 layer, the hybrid heterostructures were deposited through the previously mentioned immersive eLbL technique (**Figure 10a**).

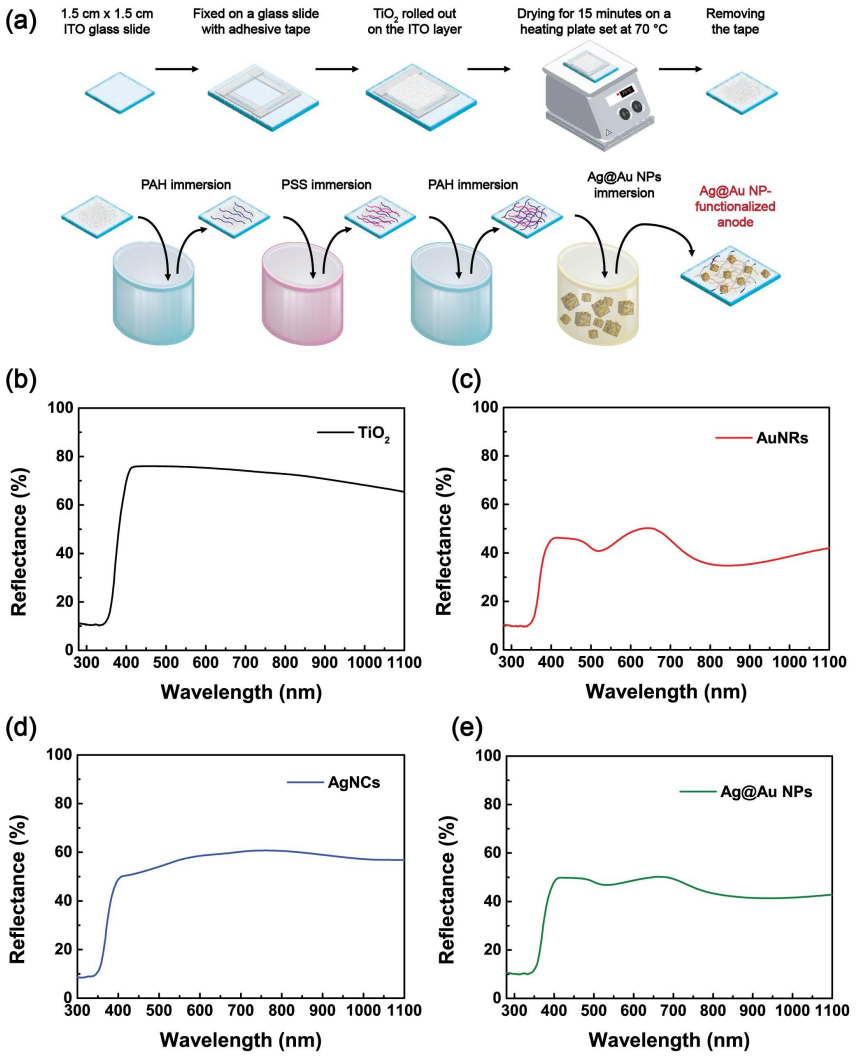

Figure 10: PSSC anode construction with optical characterization. (a) Schematic of the functionalized anode fabrication through the immersive eLbL method. Collected diffuse reflectance spectra of (b) the anode with the bare TiO_2 layer and of the (c) Au NRs-, (d) Ag NCs- and of (e) the Ag@Au NPs-functionalized anodes.

After the activation of the TiO_2 substrate through the oxygen plasma treatment, it was sequentially immersed in PAH-PASS-PAH solutions to construct the polyelectrolyte multilayer. After that, the sample was immersed overnight in a MNPs colloidal dispersion to enable their immobilization. This bottom-up technique enables the self-assembly of MNPs resulting in a randomly arranged array decorating the porous structure of the semiconductor that further provides a larger surface area for effective NPs binding.
Initially the anode with the bare TiO_2 thin layer was analyzed through optical characterization (**Figure 10b**). The UV-visible diffuse reflectance spectrum shows that the TiO_2 exhibits enhanced absorption only for wavelengths < 430 nm while, for higher wavelengths, the radiation is completely reflected conferring its typical white hue. The recorded data were employed to estimate, through the Tauc method,[68] the bandgap energy (E_g) of the TiO_2 semiconductor: the energy needed to excite an electron from the valence to the conduction band. Since E_g = 3.170 eV ± 0.003 eV, the electron-hole pair generation can occur when the semiconductor is irradiated at a wavelength lower than 391 nm. Commonly, the addition of the photosensitizer agent improves the light absorption in the visible range. In this work, the functionalization of the TiO_2 anodes with three different NP species, Au NRs, Ag NCs and Ag@Au NPs, highlights this aspect. Indeed, the diffuse reflectance spectra of the functionalized anodes are depicted to analyze their optical properties. Indeed, the deposition of Au NRs on the TiO_2 anode induces changes in the optical properties evidenced by the emergence of the LSPRt and LSPRl absorption peaks at 519 nm and 845 nm in the diffuse reflection spectrum (**Figure 10c**) that undergo a redshift of 7 nm and 45 nm, due to the higher refractive index of the TiO_2 of ~2.6 [69] compared to air, ~1. Similarly, the presence of Ag NCs on the TiO_2 layer also affects the second functionalized anode spectrum (**Figure 10d**). The dipolar resonance peak appears redshifted while the quadrupolar peaks remain unvaried. However, the exact

wavelength positioning values are difficult to detect since the thick TiO_2 layer results in an increase of the cross-section of the quadrupolar resonance.[70] As a result, the weakly pronounced dipolar resonance peak is redshifted to ~1070 nm [71] while the quadrupolar resonance peak is revealed by a shoulder located at ~480 nm, partially covered by the TiO_2 layer absorbance. The third anode functionalized with Ag@Au NPs exhibit the optical contributions of both the NP species. The diffuse reflectance spectrum in **Figure 10e** shows the LSPRl peak at 941 nm, redshifted for the presence of both the TiO_2 and the Ag NCs in close contact with the Au NRs surface and an additional lower absorbance peak at 531 nm that corresponds to the LSPRt peak of Au NRs and to the dipolar peak of Ag NCs.

Figure 11: Photograph of the Ag@Au NPs colloidal dispersion.

The analyzed optical properties also affect the functionalized anode appearance. Indeed, the typical pinkish hue of the Ag@Au NPs colloidal dispersion (**Figure 11**) is transferred to the functionalized anode through the eLbL method achieving a homogenous anode with a uniform pink tone indicating the loading of the NPs (**Figure 12a**).

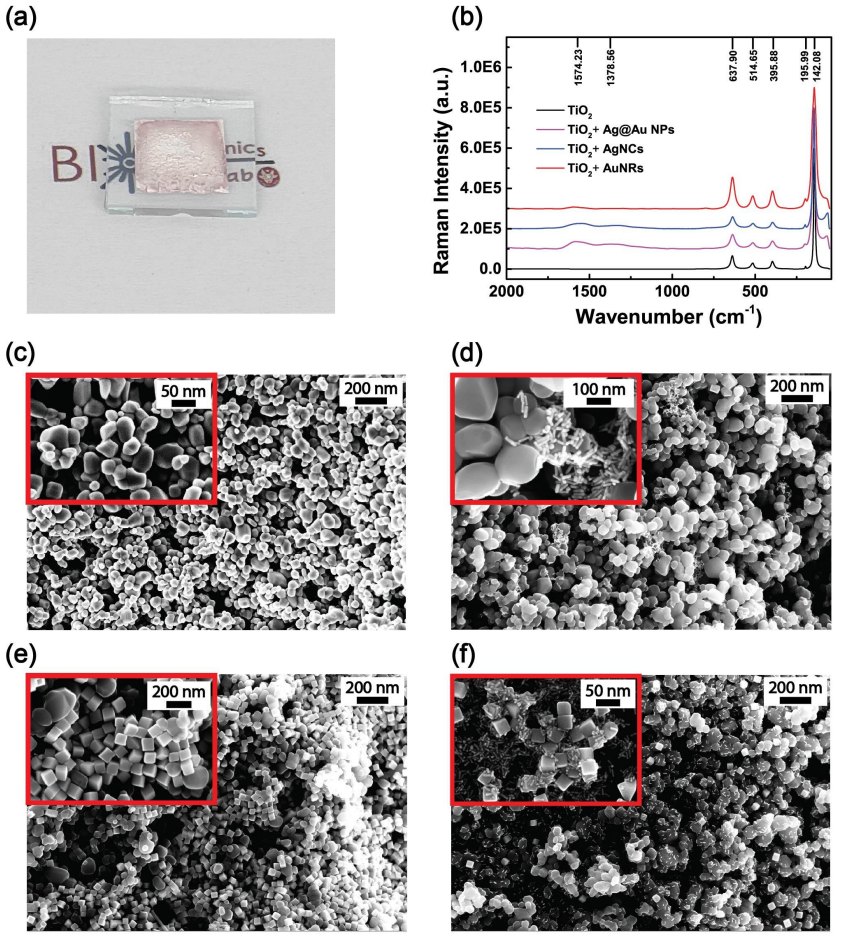

Figure 12: Spectroscopic and morphological characterization of the PSSC functionalized anodes. (a) Photo of the realized Ag@Au NP functionalized anode. (b) Raman spectra overlapping of the bare TiO_2 anode (black curve) and of the Au NRs- (red curve), Ag NCs- (blue curve) and Ag@Au NPs-functionalized (purple curve) anodes. Morphological characterization through SEM microscopy of the bare TiO_2 anode (c) and of the Au NRs- (d), Ag NCs- (e) and Ag@Au NPs-functionalized (f) anodes.

Further analysis were performed using Raman spectroscopy that shows the crystalline structure of the different anodes. The spectra are presented in **Figure 12b**. The presence of the TiO_2 anatase phase is characterized by the tetragonal space group of *I41/amd*, allowing six Raman-active modes (one A1g, two B1g and three Eg). Indeed, the presented Raman spectra show four prominent bands at 142 cm^{-1}, 396 cm^{-1}, 515 cm^{-1} and 638 cm^{-1} corresponding to the Eg, B1g, A1g and Eg vibrational modes of the anatase phase, respectively. [72, 73, 74] These vibrational modes are produced by the symmetric stretching (Eg) and bending (B1g) vibrations and by the antisymmetric bending (A1g) vibrations of the O-Ti-O bonds within the TiO_2 crystal lattice. Thus, these peculiar Raman shifts as well as their relative intensities suggest the TiO_2 pure anatase phase formation. Moreover, the functionalized anodes also present broad signals at ~1380 cm^{-1} and ~1570 cm^{-1}, corresponding to the D and G bands of amorphous carbon, respectively. The presence of the organic capping agents stabilizing the colloidal NPs can explain the appearance of these bands proving the loading of the NPs on the TiO_2 layers. The so-called D band is attributed to the disordered carbon or structural defects in the sp^2- hybridized carbon structure and is visualized at ~1380 cm^{-1} while the G band is attributed to the graphitic (C=C) stretching vibrations in sp^2 carbon domains and is located at ~1570 cm^{-1}.

The direct prove for the presence of the three NP species on the TiO_2 layers is given by the SEM miscroscopy that should confirm the collected data in UV-visible and Raman spectroscopies. The SEM micrograph of the bare TiO_2 layer (**Figure 12c**) points out the porous structure of the semiconductor characterized by spherical NPs having an average size of 194.0 nm ± 39.3 nm. Then, the functionalized anodes exhibit different NP arrangements according to their size and shape. Indeed, even if the SEM micrograph in **Figure 12d** illustrates the Au NRs binding the TiO_2 NPs in various areas, the regions more devoid of the semiconductor also exhibit dense distribution of Au NRs deposited on the ITO substrate due to

the reduced dimensions of Au NRs that enable their filtration through the free spaces among the TiO_2 NPs (**Figure 13**). The presence of Au NRs on both the ITO substrate and the TiO_2 NPs increases their effective density with respect to the evaluation performed through microscopy. On the contrary, the deposition of Ag NCs, shown in **Figure 12e**, mainly occurs on the TiO_2 NPs outer layer since the bigger dimension of Ag NCs (100 nm size) do not allow their filtration. The hybrid heterostructures array deposition, instead, produces a random arrangement of Au NRs, Ag NCs and Ag@Au NPs (**Figure 12f**). However, the heterostructure geometry is still preserved in different areas across the functionalized anode surface (see zoom in **Figure 12f**).

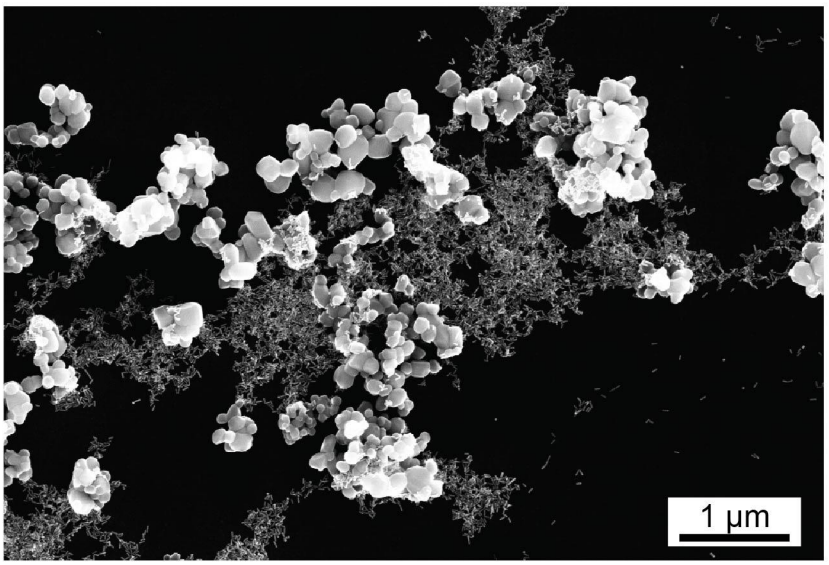

Figure 13: SEM micrograph of the TiO_2 anode external border functionalized with AuNRs.

4.1.4 Optical metasurfaces construction with optical and morphological characterization

Despite the high precision of lithography-based methods for the construction of optical metasurfaces, they also require high costs for the production process and maintenance as well as dedicated facilities hindering the scalability of the products that are limited to small patterning areas, due to the diffraction limit. For this reason, the promising opportunities of bottom-up techniques are important object of study for mass-scale production of metasurfaces.[18] They rely on the use and deposition of colloidal nanocrystals on dielectric or metal substrates. In particular, the deposition of plasmonic MNPs on thin metallic layers generates the SLR modes as the coupling of the SPR effect of the thin metallic layer and the LSPR phenomenon of the MNPs array. The fabrication of ordered plasmonic metasurfaces relies on template-assisted self-assembly methods that strongly depend on the structural properties and limitations of the templates usually constructed through lithography-based methods.[75] Recent studies focus on disordered metasurfaces that unlock new opportunities in terms of highly tunable and versatile novel fabrication methods. Among them, the eLbL method has been widely investigated for plasmonic and hybrid metasurfaces.[76] In this work, we exploit the immersive eLbL technique for the realization of a plasmonic disordered optical metasurface. The optimized protocol is schematized in **Figure 14a**. At first the polyelectrolyte multilayer is constructed on a Au-coated rigid substrate that was alternatively immersed in the positively and negatively charged polyelectrolytes, PAH and PSS for 5 min each with the sequence PAH/PSS/PAH/PSS/PAH. Intermediate washing steps were performed immersing the substrate in NaCl for 1 min. The final overnight incubation in the Ag NCs colloidal dispersion enabled the immobilization of the NPs. The depicted protocol enables the easy scalability of the device.

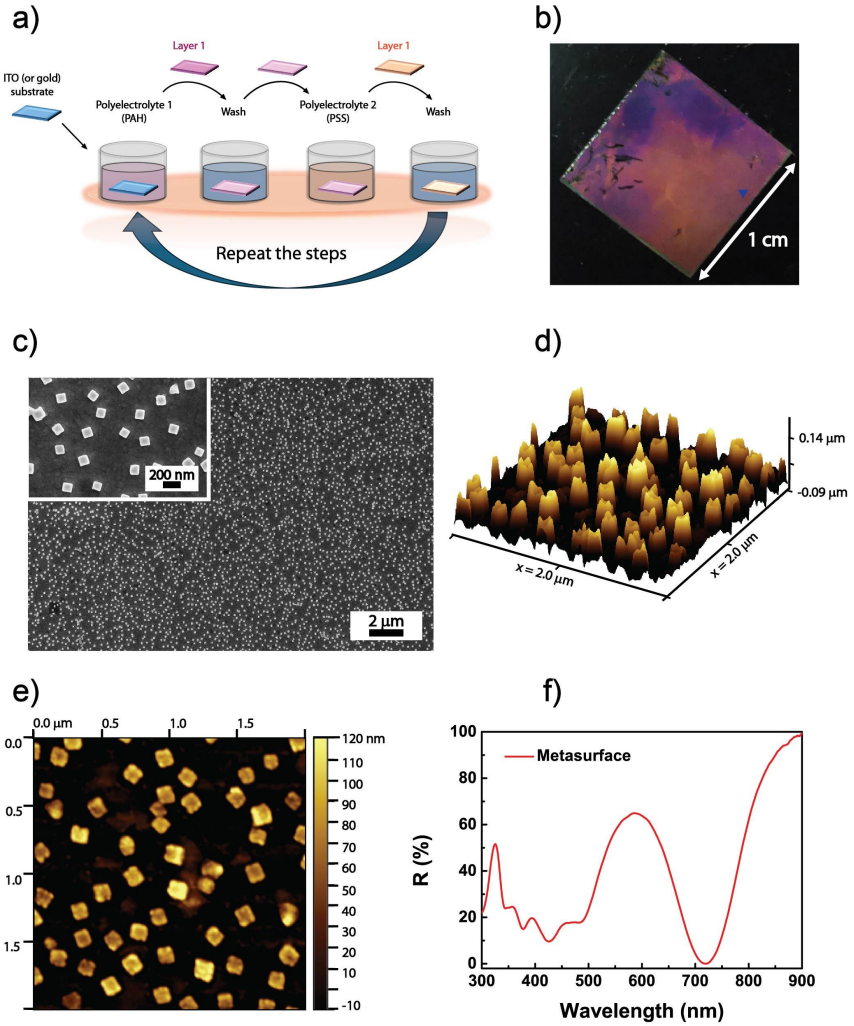

Figure 14: Fabrication process, morphological and optical characterization of the bottom-up disordered plasmonic metasurface. (a) Schematic of the immersive eLbL deposition method. (b) Representative photo of the realized plasmonic metasurfaces. Morphological characterization of the optical metasurface through (c) SEM, (d) 3D and (e) 2D AFM analysis. (f) Specular reflection spectrum of the metasurface. Reproduced under terms of the CC-BY 3.0 license. [77] 2025, Zaccagnini et al., published by Wiley-VCH GmbH.

Indeed, the representative photo of the obtained optical metasurface in **Figure 14b** highlights the relatively large dimensions of 1 cm x 1 cm and its bright pinkish hue that cover quite homogenously the entire surface. Additionally, the morphological characterization through SEM microscopy further reveals an even and dense distribution of Ag NCs on the Au thin layer (**Figure 14c**). The micrograph analysis reveals an interparticle distance of 412.0 nm ± 63 nm and a size of 105 nm ± 12 nm. Moreover, the fill fraction of 11.7 ± 0.4 assess the homogeneity of the NPs distribution. AFM micrographs (**Figure 14d, e**) exhibit the even distribution of Ag NCs and a heigh profile of 100 nm considered consistent with the NPs size. The optical features were analyzed through UV-visible spectroscopy (**Figure 14f**). The specular reflection spectrum was collected with a customized reflective fiber-coupled spectrophotometer. The metasurface spectrum presents a first absorption depth at 485 nm due to the absorbance of the Au NCs and a second stronger absorption depth at 719 nm due to the SLR mode. The calculated absorption efficiency of 65% is calculated as the intensity difference between the maximum reflected light and the reflection value at 719 nm.

The metasurface sensitivity to the surrounding medium variation was firstly evaluated through the construction of a glass cell on the top of the metasurface with 10 μm microbeads as a spacer. The realized metasurface cell was infiltrated via capillary forces with NOA-61. The variation of the refractive index from air (blue curve in **Figure 15a**, n~1) to NOA-61 (red curve in **Figure 15a**, n~1.56) produced a red shift of the metasurface absorption depth of 77 nm. This drastic and gradual colorimetric change is also visible to the naked eye. Indeed, the pinkish color of the bare metasurface (**Figure 15b**) gradually becomes yellow (**Figure 15d**) as the infiltration process continues. **Figure 15c** clearly shows the color alteration during the NOA-61 filling. Numerical simulations,

represented by the dashed curves in **Figure 15a**, further confirm the experimental results.

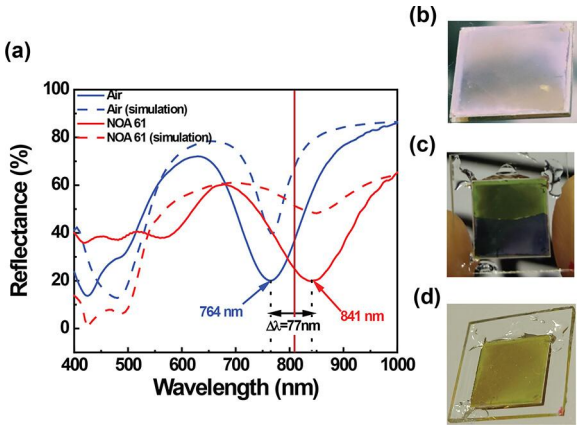

Figure 15: Sensitivity test of the bottom-up plasmonic metasurface. (a) Optical reflection spectroscopy of the metasurface cell before and after in glue NOA-61 infiltration with the corresponding numerical simulations. Photos of (b) the bare metasurface and of metasurface cell (c) before and (d) after the NOA-61 infiltration. Reproduced under terms of the CC-BY 4.0 license. [19] 2023, Petronella et al., published by American Chemical Society.

4.2 Photothermal and photoelectric characterizations of plasmonic nanostructures

The field of thermoplasmonics offers innovative opportunities in the biomedical field for applications such as the disinfection of pathogens through photo-induced heating, the implementation of smart PPE like next-generation face masks or the realization of cutting-edge PV systems. Indeed, many fields would take advantage of the localized heating generated by the so-called nanotransducers. IR thermography is an efficient tool to precisely monitor bulk temperature variations. For this reason, it will be largely employed during the following experiments.

4.2.1 Gold nanorods array photothermal response

The optical properties of Au NRs array depicted in **Section 4.1.1** reveal a significant LSPRl absorption peak at ~764 nm. Consequently, a strong photothermal energy conversion occurs at its resonant frequency in the NIR range.

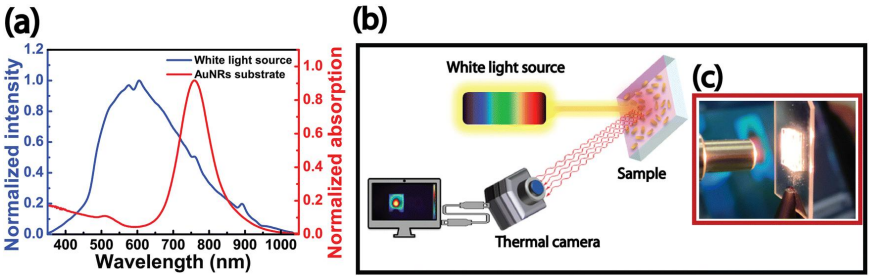

Figure 16: (a) Overlapping of the Au NRs substrate absorption spectrum (red curve) with the white light intensity emission spectrum (blue curve). (b) Schematics of the optical setup arranged for the white light photothermal characterization of the Au NR substrates. (c) Photo of a representative plasmonic platform entirely irradiated by the optical fiber of the white light source. Reproduced under terms of the CC-BY-NC 3.0 license. [62] 2023, Zaccagnini et al., published by Royal Society of Chemistry (RSC).

In previous work, we have demonstrated the ability of these plasmonic platforms to convert incident laser light into heating.[78] A two-color optical setup was used to monitor the photothermal response of Au NR substrates under 532 nm and 808 nm CW laser beam irradiations that were purposely selected to excite LSPRt and LSPRl modes, respectively. The light-to-heat conversion efficiency was evaluated by the temperature profiles that were collected by a high resolution thermal camera. The time-temperature profiles accounted for the higher photothermal efficiency of the LSPRl (excited with the NIR laser) than that of the LSPRt (excited with the green laser). In this work, we aim to take a step forward in the field of photothermal energy conversion by achieving a strong and localized heating effect through the use of a common white light

source for an innovative safer and facile method. Au NR substrates exhibit a significant LSPRl absorption peak in the NIR range (red curve in **Figure 16a**) that significantly overlaps the tail of the white light emission spectrum from 600 nm to 900 nm (blue curve in **Figure 16a**). To investigate the white light-triggered thermoplasmonic effect in Au NR substrates, an optical setup (**Figure 16b**) was implemented comprising a white light source that completely irradiates the surface of the functionalized glass substrates with the use of an optical fiber (**Figure 16c**). A fixed distance of illumination was set at 1 cm at normal incidence to maintain the convergence of the light beam. The temperature profile and the spatial heating distribution were recorded by a high resolution thermal camera on the platforms surface during the irradiations. The white light-triggered photothermal response of the plasmonic substrates was investigated irradiating the samples at different power density values (**Figure 17a**). The Au NRs platform was irradiated for 5 min and then the white light source was switched off allowing the sample to cool off for 2 min. The maximum temperature increase as a function of the irradiation time shows an exponential increase during the first 2 min and after the subsequent plateaux, the temperature gradually decreases with the shutdown of the light source. This behaviour is consistent with the experimental data of laser-driven photothermal analysis of Au NRs colloidal dispersion[79] or substrates.[78]

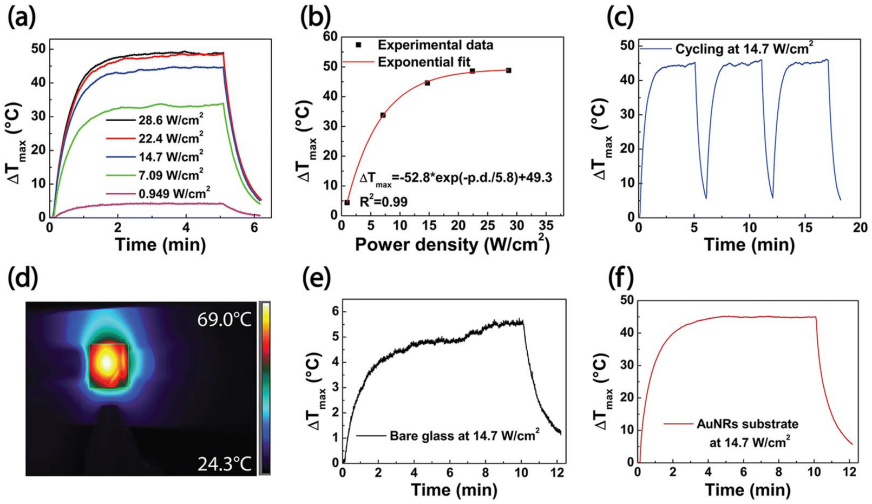

Figure 17: White light photothermal characterization of Au NR substrates. (a) Temperature variation as a function of the white light irradiation time at different power density values. (b) Maximum temperature increase as a function of the power densities corresponding values. (c) Maximum temperature increase as a function of the time irradiation interval during the cycling measurements performed irradiating the plasmonic substrates for three consecutive times. (d) Thermographic image of a Au NRs substrate irradiated under white light source for 10 min of time interval at a power density of 14.7 W cm^{-2}. Maximum temperature increase as a function of the irradiation time achieved by (e) a bare glass substrate and (f) a Au NRs substrate after 10 min at 14.7 W cm^{-2}. Reproduced under terms of the CC-BY-NC 3.0 license. [61] 2023, Zaccagnini et al., published by Royal Society of Chemistry (RSC).

It is clearly visible that the temperature rises with the power density of the white light source, ranging from 0.949 W cm^{-2} to 28.6 W cm^{-2}. Accordingly, the measured temperature variation (from 4.44 °C to 49.3 °C) rises exponentially (**Figure 17b**) with the power density. Further investigations were performed at a reference power density value of 14.7 W cm^{-2}, sufficient to achieve a maximum temperature of 69 °C. Cycling measurements were performed irradiating the sample for three consecutive cycles (**Figure 17c**) in the same experimental conditions previously

described. The irradiated plasmonic platform recorded the same temperature increase for each cycle proving the photothermal and structural stability of the realized substrates. Furthermore, the thermographic images (**Figure 17d**), collected by the high resolution thermal camera, recorded a homogenous heating distribution achieved on the entire area of the white light-irradiated platform, due to the use of the output optical fiber of the light source. An essential control experiment was performed to validate the Au NRs contribution to the heating increase. For this reason, a bare glass substrate (**Figure 17e**) and a Au NRs substrate (**Figure 17f**) were irradiated in the same experimental conditions, at 14.7 W cm^{-2} for 10 min. As a result, the recorded temperature increases were of 5 °C and 44.7 °C, respectively. The 87.3% higher temperature increase in the irradiated plasmonic platform confirms the exceptional ability of Au NRs as nanotransducers, capable to convert the absorbed light by a conventional white light source into heating. The thermoplasmonic effect of these nanostructures can be evaluated by calculating their photothermal conversion efficiency. This value states for the ratio of the increased internal energy to the total incident radiation (see **Appendix 6.1**). In conditions of constant room temperature and uniform light irradiation, the photothermal efficiency of 43.5% was calculated for Au NRs substrates compared to the 5.50% of the bare glass substrates.

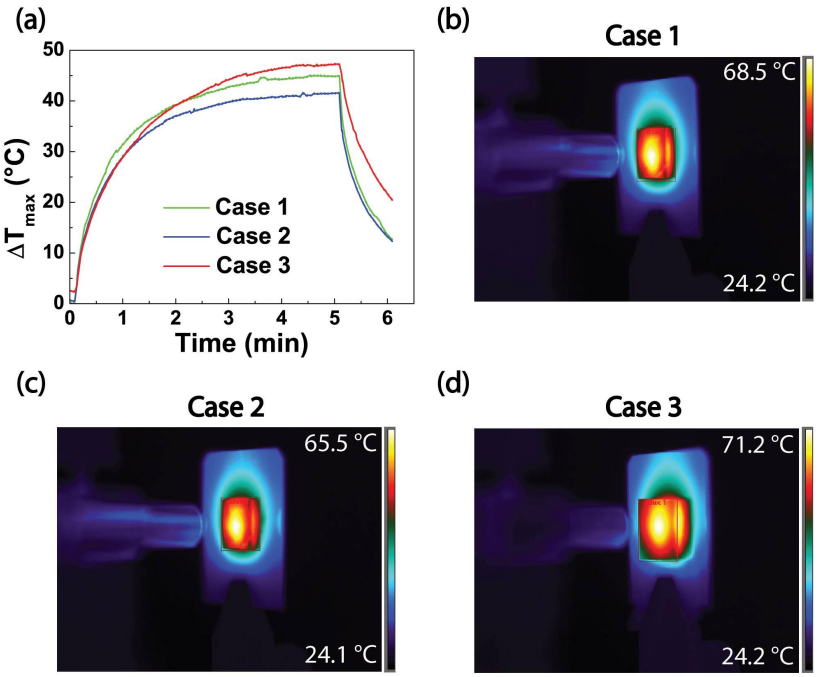

Figure 18: White light photothermal characterization of the Au NR substrate with glass cells realized to monitor the sensitivity of the plasmonic platforms. (a) Temperature increase as a function of the time of irradiation of the plasmonic platforms in the three distinguished Cases previously described in **Section 4.1.1**. Thermographic images of the irradiated substrate in (b) Case 1, (c) Case 2 and (d) Case 3. Reproduced under terms of the CC-BY-NC 3.0 license. [61] 2023, Zaccagnini et al., published by Royal Society of Chemistry (RSC).

Furthermore, we aimed to monitor the photothermal response of the plasmonic substrates as the refractive index of the medium surrounding the nanostructure changes. To do so, we characterized photothermally the Au NRs substrate in the three different conditions depicted in **Section 4.1.1**, properly selected to evaluate the sensitivity of the platforms: two glass cells were added on both the sides of the functionalized substrate that were filled, one at a time, with NOA-61. The UV-visible spectroscopy revealed that the LSPRl peak was redshifted from its initial state at 766 nm (Case 1)

to 780 nm (Case 2) with an evident shoulder located at 882 nm and to 882 nm (Case 3). These variations could significantly change the photothermal behaviour of the irradiated substrate. For this reason, the plasmonic platform was irradiated in the three different conditions (Case 1, 2 and 3) under white light source at 14.7 W cm^{-2} plus 1 min when the source was switched off for the substrate cooling. As the overlapped time-temperature plots show in **Figure 18a**, a higher temperature increase is recorded in Case 3 compared to Case 1. However, the mentioned temperature variation rises by only 2.3 °C while in Case 2 it gets lower of -3.4 °C. These experimental data can be explained by the occurrence of a competitive effect. On one hand the temperature becomes higher for larger dielectric constant values and thus, refractive index of the surrounding medium of Au NRs. On the other hand, this refractive index increase produces a significant redshift of more than 100 nm in the LSPRl peak from 766 nm to 882 nm. The white light intensity value corresponding to the absorbance of LSPRl at 882 nm is lower compared to the one for the LSPRl at 766 nm. The expected temperature increase due to the larger refractive index of NOA-61 is counterbalanced by the decreased intensity value of the white light source due to the redshift of the LSPRl peak. The thermographic images in **Figure 18b**, **c** and **d** highlight a homogeneous heating distribution on the entire area and an increased thickness due the addition of the glass cells on both the sides of the plasmonic substrate.

4.2.2 Plasmonic hybrid heterostructures photothermal response

The compelling optical properties of the realized hybrid heterostructures showcase excellent potential in terms of broadband light absorption. For this reason, it was necessary to investigate the contribution of the single wavelengths to the photothermal efficiency under a broadband source.

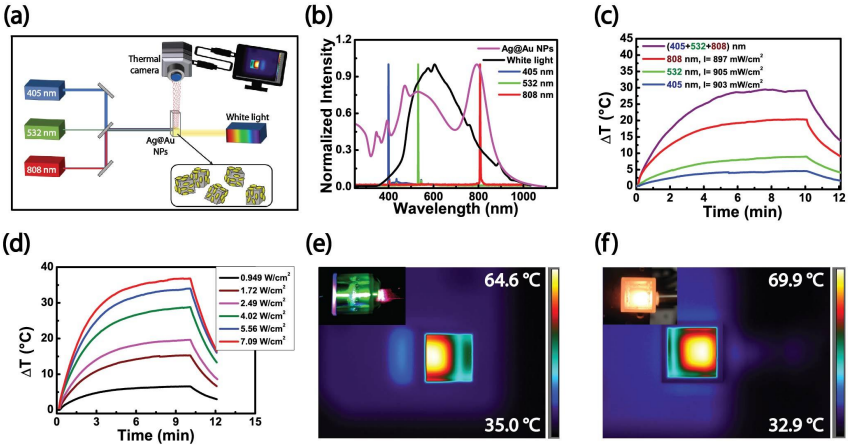

Figure 19: Photothermal characterization of the hybrid heterostructures dispersion. (a) Schematic of the optical setup implemented for the multicolour laser and white light photothermal characterization of the Ag@Au NPs dispersion. (b) UV-visible absorption spectrum of Ag@Au NPs dispersion overlapped with the intensity emission spectra of the lasers and white light sources. Temperature increase as a function of the time of the colloidal dispersion irradiated for 10 min (c) by three different laser source and (d) by the white light source at different power density values. Thermographic images of Ag@Au NPs dispersion in a quartz cuvette irradiated (e) by the three lasers and (f) by the white light source with their respective photos as inset. Reproduced with permission. [62] 2024, Wiley-VCH GmbH.

The schematic of the optical setup in **Figure 19a** shows that the Ag@Au NPs dispersion was irradiated by three different co-launched laser sources, namely CW laser beams working at 405 nm, 532 nm and 808 nm and by a collimated white light source. All these beams irradiate the side of the quartz cuvette containing the hybrid heterostructures dispersion. The intensity emission spectra of the depicted light sources were overlapped with the UV-visible absorption spectrum of the Ag@Au NPs dispersion in **Figure 19b**. It is worth noting that the laser beams were selected to specifically excite the resonant frequencies of the compound. The white light source, instead, overlaps the whole wavelengths range

given by the Ag@Au NPs absorbance. The photothermal characterization carried out with the multicolour setup was conducted irradiating the sample under the single laser sources and then co-launching all the lasers simultaneously. The recorded maximum temperature increases were of 5 °C, 9 °C, 20 °C and 29 °C for the laser emitting at 405 nm, 532 nm, 808 nm and for their simultaneous irradiation, respectively (**Figure 19c**). The corresponding photothermal efficiencies, calculated assuming a constant room temperature during the irradiations, were of 2.1%, 17.8%, 59.2% and 91.5% (see **Appendix 6.1**). These data not only reveal the different contributions of the investigated wavelengths in the absorption spectrum of the hybrid heterostructures but also prove the photothermal enhancement obtained by combining all the single laser wavelengths mimicking a broadband source irradiation. As a consequence, we also tested the photothermal behaviour of the Ag@Au NPs dispersion under the broadband white light source irradiating the compound at different power density values (**Figure 19d**), from 0.049 W cm^{-2} to 7.09 W cm^{-2} that produce temperature increases from 6 °C to 37 °C, achieving the maximum temperature of 69.9 °C. The thermographic images in **Figure 19e** and **f** are collected using a top view-thermal camera and show the quartz cuvette filled with the Ag@Au NPs dispersion when it is irradiated by the laser beams and by the white source respectively. The laser beams are aligned at the air-liquid interface so that it was possible to detect the heating profile on the 1 cm^2 area of the cuvette. The white light source, equipped with the optical fiber with a larger beam size, can easily irradiate almost the whole dispersion. As a result, a homogenous temperature distribution on the cuvette surface is obtained during the irradiation performed with the co-launched lasers and with the white light source (**Figure 19e** and **f**). A better photothermal output is obtained with the illumination under white light source since it can exploit all the wavelengths range belonging to the Ag@Au NPs absorption spectrum, leading to a 5.3 °C higher maximum temperature. However, the calculated photothermal efficiency for

the white light irradiation exhibits a low value of 6.0% due to the properties of the employed white light source such as the high intensity needed by the white light source that highly exceed the values of common lamps or LED whose values usually are ~1 W cm^{-2} and also the broader optical fiber output compared to the lasers. The thermal conductivity of the medium surrounding the NPs can also affect the photothermal efficiency. Indeed, bulk water still plays a significant role in heat transfer, even without the presence of NPs. It is worth noting that a great improvement of the photothermal efficiency would be possible depositing the Ag@Au NPs on a substrate with lower thermal conductivity.

4.2.3 Plasmon-sensitized solar cells photothermal and photoelectric responses

The optical and photothermal analysis depicted in the **Sections 4.1.2** and **4.2.2**, demonstrated the improved absorbance capabilities of the hybrid heterostructures under a broadband light source compared to the single wavelength lasers. In view of these results and of the optical characterization of the functionalized anodes in **Section 4.1.3**, we aim to verify if the hybrid plasmonic heterostructures can be selected to realize PSSCs achieving visible light energy harvesting and exceeding the output of DSSCs and of Au NRs and Ag NCs PSSCs.

The working mechanism of PSSCs is schematized in **Figure 20a** and begins with the absorption of incident light by plasmonic MNPs.

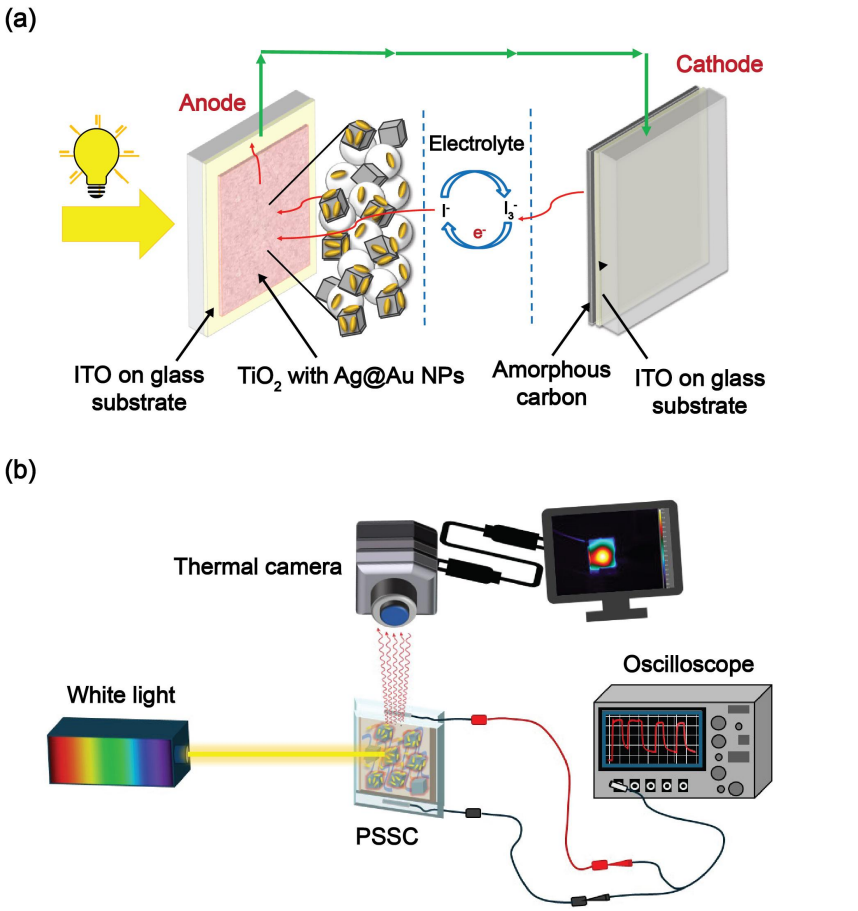

Figure 20: (a) Schematic of the PSSC working mechanism. (b) Schematic of the photothermal and photoelectric setup.

This photon absorption excites electrons from the ground state to higher energy levels, initiating collective oscillations of the free electrons, known as plasmons. These oscillations induce localized dipoles that facilitate plasmon-induced charge separation and enhance photoelectron transitions. Electron-hole pairs are generated in the metal through interband and intraband transitions,

leading to the formation of energetic, or 'hot,' charge carriers. These hot electrons can be injected into the conduction band of an adjacent n-type semiconductor, such as TiO_2, whose conduction band edge is positioned below the excited energy level of the MNPs. The excited electrons are then transported through an external circuit to the cathode electrode. Due to the presence of a Schottky barrier, the backflow of electrons into the MNPs is prevented. The oxidized MNPs are subsequently regenerated by electron donation from the redox species in the electrolyte, thereby completing the cycle.

PV cells convert incident light primarily into electrical energy, with a portion also dissipated as heat.[80, 81] An excessive high temperature may lead to the deterioration of the PV cells (safety threshold of 70 °C) and lower the operating voltage while increasing the reverse saturation current and reducing the energy gap.[82] For this reason, both the photothermal and photoelectric characterization were performed.

At first, the Au NRs, Ag NCs PSSCs and DSSCs were monitored by using the optical setup in **Figure 20b**. It shows the PV cell irradiated by the white light source and monitored by a high resolution thermal camera that record the heating distribution and by the oscilloscope to collect the generated output voltage.

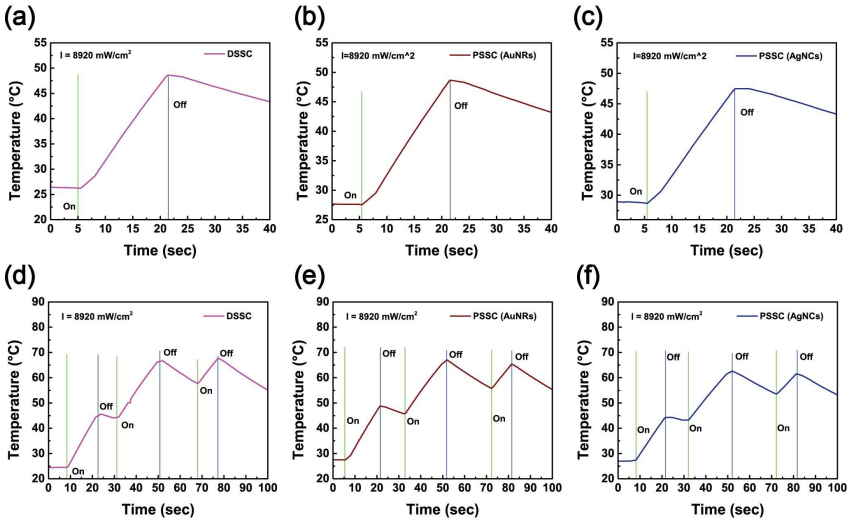

Figure 21: Photothermal characterization of Au NRs, Ag NCs PSSCs and DSSC. Temperature as a function of the time of the irradiate (a) DSSC, (b) Au NRs and (c) Ag NCs PSSCs under white light source. Cycling experiments of the photothermal response of (d) DSSC, (e) Au NRs and (f) Ag NCs PSSCs.

The white light-triggered photothermal response was evaluated irradiating the selected PV cell at 10 mm of distance with the use of an optical fiber, at the highest intensity of 8920 mW cm^{-2} for 20 sec and then switching off for other 20 sec to cool off the sample. The entire surface of the PV cell was irradiated and monitored. The recorded maximum temperatures reach 48.62 °C ± 2.4 °C, 47.48 °C ± 2.4 °C and 48.65 °C ± 2.4 °C for the DSSC (**Figure 21a**), Ag NCs (**Figure 21b**) and Au NRs (**Figure 21c**) PSSCs. Cycling measurements were collected to investigate the stability and reversibility of the heating distribution over time. Indeed, three irradiation cycles were performed increasing the temperature to 68.0 °C ± 3.4 °C (**Figure 21d**), 62.0 °C ± 3.1 °C (**Figure 21e**) and 65.0 °C ± 3.3 °C (**Figure 21f**), respectively. Even if the achieved

temperatures remain below the safety threshold, DSSCs reach the highest temperature, close to the threshold limit.

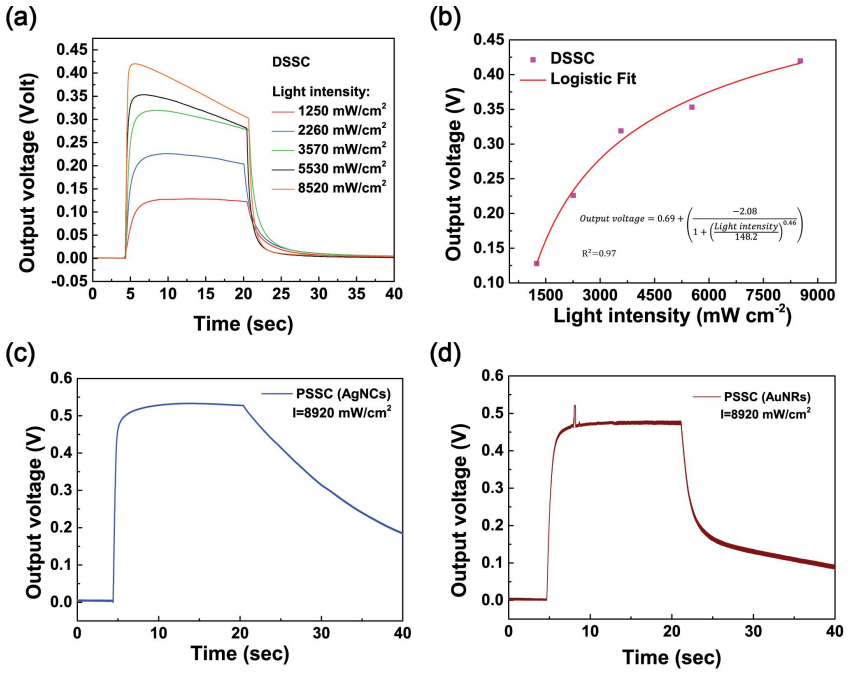

Figure 22: Photoelectric characterization of Au NRs, Ag NCs PSSCs and DSSC. (a) Output voltage as a function of the time for the DSSC at different light intensity values. (b) Output voltage as a function of the light intensity for the DSSC with logistic fit curve. Output voltage as a function of the time for the (c) AgNCs and (d) Au NRs PSSCs.

Similarly, the photoelectric characterization was performed monitoring the output voltage with an oscilloscope. At first the DSSC was irradiated under the same experimental conditions set for the photothermal characterization at different white light power density values, ranging from 1250 mW cm^{-2} to 8520 mW cm^{-2} (**Figure 22a**). The output voltage rises as a function of the light intensity (**Figure 22b**) reaching the maximum value of 0.42 V ±

0.02 V. The same measurements were recorded for the Ag NCs (**Figure 22c**) and Au NRs (**Figure 22d**) PSSCs at the maximum power density of 8920 mW cm^{-2} obtaining higher output voltages compared to DSSC, of 0.53 V ± 0.03 V and 0.48 V ± 0.03 V respectively.

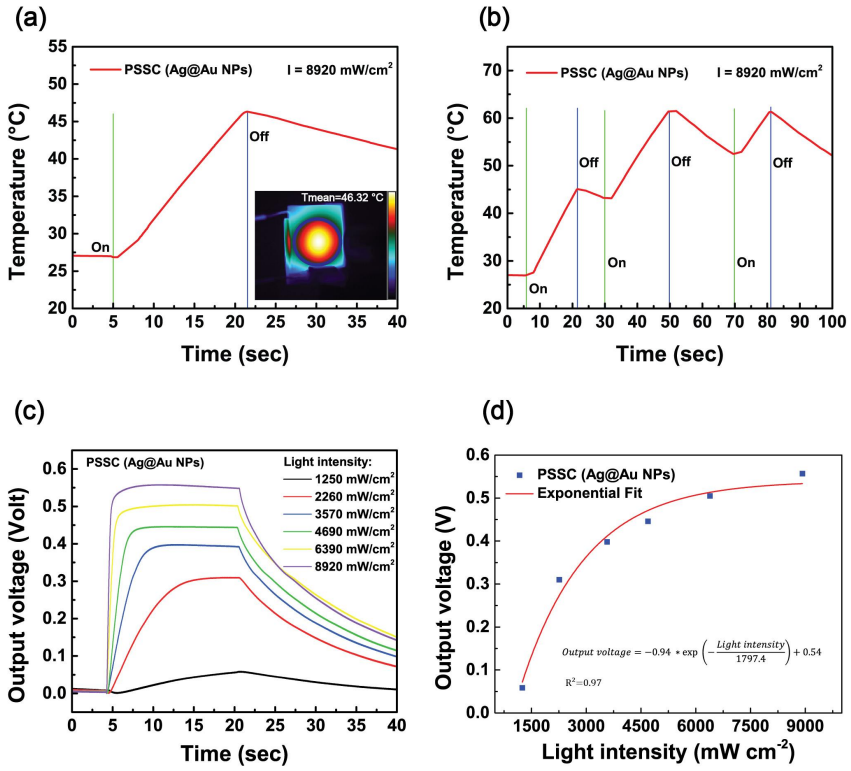

Figure 23: Photothermal and photoelectric characterization of Ag@Au PSSC. (a) Maximum temperature as a function of the time for the irradiated Ag@Au PSSC with thermal image as the inset. (b) Cycling measurements of the photothermal response. (c) Output voltage as a function of the time at different light intensity values for Ag@Au PSSC. (d) Exponential rising curve of the output voltage as a function of the light intensity.

The main novelty of this work is the introduction of the novel hyperbranched heterostructures into the PSSCs with the aim to improve visible light energy harvesting. The Ag@Au PSSCs photothermal and photoelectric responses were investigated in the same experimental conditions used for Au NR and Ag NC PSSCs and DSSC. Indeed, **Figure 23a** shows the thermographic image of the irradiated Ag@Au anode. The heating distribution covers the central active area of the sample. The recorded maximum temperature is of 46.32 °C ± 2.3 °C. Cycling measurements were collected to investigate the stability and reversibility of the heating distribution over time. After three irradiation cycles, the temperature increases to 61.27 °C ± 3.1 °C (**Figure 23b**). The achieved temperatures remain below the safety threshold and lower compared to the previously treated DSSC and PSSCs. Once the photothermal response has been verified, the photoelectric characterization was conducted. The PSSC was irradiated for 20 sec at different power density values from 1250 mW cm^{-2} to 8920 mW cm^{-2} (**Figure 23c**). Then the white light source was switched off to cool off the sample. The maximum output voltage of 0.56 V ± 0.03 V is recorded by the oscilloscope at 8920 mW cm^{-2} white light intensity exceeding the photoelectric performance of the previous DSSC and PSSCs. The output voltage as a function of the white light intensity shows an exponential rising curve in **Figure 23d**, highlighting a different behaviour compared to the logistic curve corresponding to the DSSC (**Figure 22b**). To summarize, Ag@Au PSSCs exhibit the best photoelectric response and the lowest heating production, under the investigated experimental conditions.

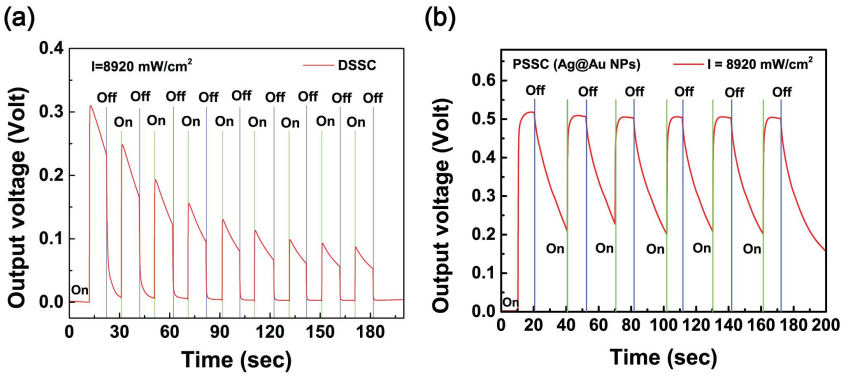

Figure 24: Cycling measurements of the photoelectric response of the (a) DSSC and (b) Ag@Au PSSC irradiated under white light source at 8920 mW cm^{-2}.

Further measurements were performed to compare the stability and the reversibility of the DSSCs and PSSCs photoelectric response. Indeed, cycling experiments were conducted on DSSC and Ag@Au PSSC. Cycling measurements conducted on the DSSC (**Figure 24a**) demonstrate the rapid degradation of the photoelectric activity over time due to the organic dye properties, namely photobleaching and degradation phenomena. Conversely, the Ag@Au PSSC cycling curve highlights the long-term stability and the reversibility of their photoelectric response (**Figure 24b**). Moreover, their photoelectric efficiencies were calculated as the ratio between the maximum power density produced by the illuminated cell and the power density of the light source (see **Appendix 6.2**). The calculated values are 7.91 x 10^{-5} % and 3.24 x 10^{-5} % for Ag@Au PSSC and DSSC, respectively. The functionalization with Ag@Au NPs improves the photoelectric efficiency of 2.4 times by replacing the easily degradable organic dye. It is worth noting that Au@Ag PSSCs exhibit enhanced photoelectric performance, low heating dispersion and long-term stability over time overcoming and resolving the structural limitations of DSSCs. For this reason, Ag@Au NPs may represent a new class of light absorbers for PV applications.

4.3 Plasmonic nanostructures for white light-triggered reusable devices

The exceptional photothermal and photoelectric conversion capabilities of the realized broadband light-sensitive hybrid nanostructures have been detailed. As a result, these nanostructures can be used for medical applications that exploit their properties to promote more efficient, sustainable and affordable methodologies. In the following paragraphs, broadband light-driven applications will be examined in detail. In particular, the on-demand photothermal disinfection of biomedical tools, the power supply of medical devices by PSSCs, the on-demand photothermal disinfection of smart PPE such as a FFP2 face mask and the integration of a tiny metasurface-based biosensor to confer multifunctionality to the FFP2 face mask.

4.3.1 Disinfection of surgical tools

The photothermal disinfection treatment presented in this work is a valuable alternative to the commonly used physical disinfection methods such as UV light irradiation, overcoming side effects related to healthcare and environmental safety. The often employed UV-C radiation sources emit at wavelengths between 200 and 280 nm that, despite the effective germicidal effect, may cause serious injuries from sunburn to retinal damages[83, 84] or skin cancer. Additionally, when these wavelengths are used for air disinfection, they may lead to ozone production or affect the respiratory system.[85] As a result, white light sources appear as a promising choice for cost-effective, sustainable and affordable photothermal disinfection.

The exceptional photothermal response of the Au NR substrates depicted in **Section 4.2.1**, reveals a great potential in on-demand thermal pathogens disinfection. For this reason, the white light-triggered photothermal disinfection on the plasmonic platforms

was evaluated selecting the *Escherichia coli* (*E. coli*) as model bacterium.

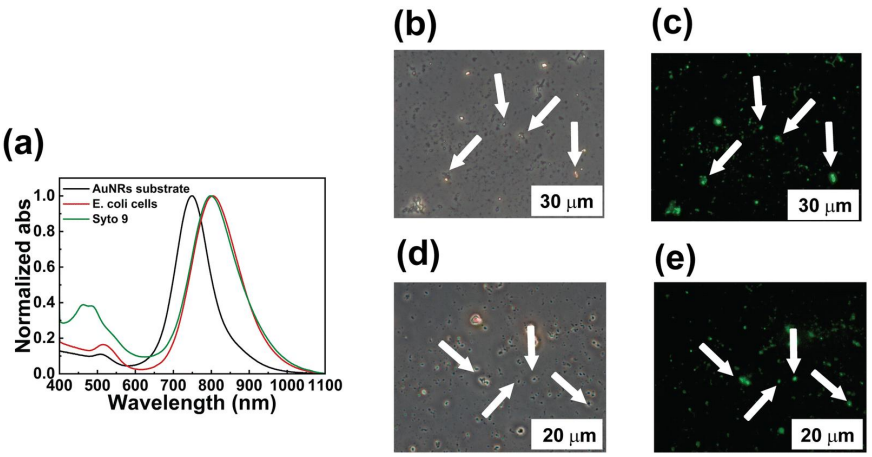

Figure 25: Biocompatibility test of the Au NR substrates. (a) UV-visible absorption spectroscopy of the Au NRs substrate in its initial state (black curve), after the E. coli contamination (red curve) and after the staining with SYTO 9 fluorescent dye (green curve). Contrast phase (b, d) and fluorescence micrographs (c, e) of two investigated areas on the contaminated plasmonic platforms at low (b, c) and high (d, e) magnification. Reproduced under terms of the CC-BY-NC 3.0 license. [61] 2023, Zaccagnini et al., published by Royal Society of Chemistry (RSC).

At first, a control experiment was performed to verify the biocompatibility of the functionalized substrates. Indeed, the Au NR platforms were intentionally contaminated by immersing them in a *E. coli* solution in Minimal E with high 10^4 CFU mL^{-1} concentration for 30 min. After that, the platforms were dried and immersed for 10 min in Minimal E with the fluorescent dye SYTO 9 that only binds to live bacteria cells. The optical characterization through UV-visible absorption spectroscopy in **Figure 25a** reveals a redshift of the LSPRl peak of 55 nm after the first immersion in *E. coli* solution (the black curve represents the initial absorption spectrum of the bare Au NR substrate and the red curve is the

spectrum after the platform soaking in *E. coli* solution). The subsequent immersion, instead, leaves the LSPRl peak position unaltered but the peak of the absorption of the green fluorescent dye appears at 450/500 nm (green curve of **Figure 25a**). Additionally, the morphological characterization of the Au NR substrates contaminated with the microbial solution was conducted with contrast phase (**Figure 25b** and **25d**) and fluorescent (**Figure 25c** and **25e**) microscopy. Indeed, the micrographs acquired at different magnifications show a distribution of live *E. coli* cells corresponding to the green and high contrast spots, thus demonstrating the biocompatibility of the realized plasmonic nanostructures.

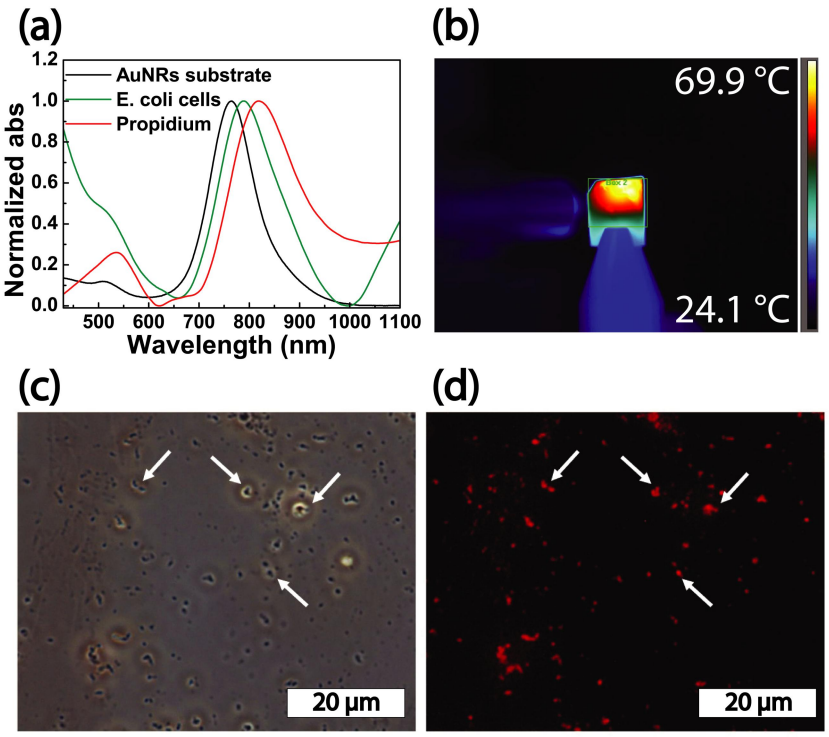

Figure 26: Photothermal disinfection of the Au NR substrates. (a) UV-visible absorption spectroscopy of the Au NRs substrate at its initial state (black curve),

after the *E. coli* contamination ()green curve and after the staining with Propidium Iodide fluorescent dye to verify the effect of the white light irradiation (red curve). (b) Thermographic image of the contaminated plasmonic platform irradiated under white light source at 14.7 W cm^{-2} at the higher maximum temperature. Contrast phase (c) and fluorescence (d) microscopy of the same investigated area on the disinfected substrates after the photothermal treatment. Reproduced under terms of the CC-BY-NC 3.0 license. [61] 2023, Zaccagnini et al., published by Royal Society of Chemistry (RSC).

Subsequently, the photothermal disinfection capability of the plasmonic platforms irradiated under white light source could be evaluated without attributing it to the mere contact with the Au NR substrate. After the intentional microbial contamination of the plasmonic platform with their immersion in 10^4 CFU mL^{-1} *E. coli* solution for 30 min, the substrates were irradiated under white light source at 14.7 W cm^{-2} for 10 min to induce the photothermal bacterial killing effect. The viability of *E. coli* cells was then monitored immersing the treated substrates in Minimal E medium with the fluorescent dye Propidium Iodide that only binds to dead cells and then visualizing the samples by contrast phase and fluorescence microscopy. The absorption spectroscopy performed after each step of the described experiment on the Au NRs substrate (**Figure 26a**, black curve), reveals a 10 nm redshift of the LSPRl peak after the microbial contamination (**Figure 26a**, green curve) due to the presence of *E. coli* cells on the sample. The second immersion, after the white light irradiation, produces a 35 nm redshift due to the presence of Propidium Iodide dye diluted in Minimal E that rises the refractive index of the medium and also produces an additional peak at ~500 nm. The white light irradiation of the contaminated Au NRs substrate was monitored through IR thermography. Indeed, the high resolution thermal camera recorded the heating distribution on the irradiated platforms revealing a maximum temperature of 69.9 °C achieved with the white light source working at 14.7 W cm^{-2} (**Figure 26b**). This temperature is sufficient to kill *E. coli* cells exceeding the minimum temperature of 60°C that is required for the rapid denaturation of proteins.[86]

After the white light disinfection treatment, contrast phase and fluorescence microscopy were used to investigate the viability of the bacterial cells on the irradiated platforms. Contrast phase micrograph with high magnification in **Figure 26c** shows high contrast spots characterized by elongated morphology typical of *E. coli* cells. The fluorescence micrograph collected investigating the same area (**Figure 26d**) shows red fluorescent spots located in the same arrangement of the high contrast spots. Therefore, they can be easily associated to dead *E. coli* cells stained with Propidium Iodide dye. These results highlight the Au NR substrate capability to achieve white light-triggered photothermal disinfection of their surface under the proper experimental conditions.

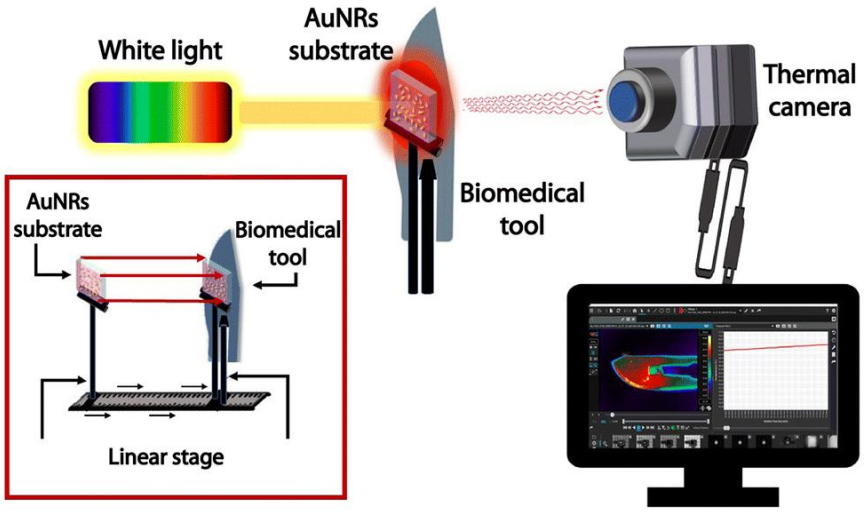

Figure 27: Optical setup for the white light triggered disinfection of biomedical tools using Au NRs substrate as a transducer. A high precision linear stage was used to maintain in close contact (few µm) the sample holders of the Au NRs substrate and of the biomedical tool. Reproduced under terms of the CC-BY-NC 3.0 license. [61] 2023, Zaccagnini et al., published by Royal Society of Chemistry (RSC).

In addition to the self-disinfectant ability of the Au NR substrates, our aim is to provide a valuable tool for biomedical tools disinfection. To do so, we exploit the light-to-heat conversion of the plasmonic platforms to disinfect metallic surfaces put in close contact with them through heat conduction. The Au NR substrates become photothermal nanotransducers that could enable the safe and efficient thermal disinfection of biomedical tools that frequently need indoor sterilization, such as surgical instruments.
The realized optical setup is shown in **Figure 27**. The Au NRs substrate was put in close contact with the selected biomedical tool and the thermoplasmonic effect of the plasmonic platform is exploited to achieve high temperature distribution also on the biomedical tool surface. This methodology avoids the deposition of Au NRs on each tool to be disinfected and provides a unique device for the disinfection of multiple surfaces. Indeed, the photothermal disinfection treatment was conducted on different tools, namely a bistoury, scissors and a spatula (**Figure 28a-c**).

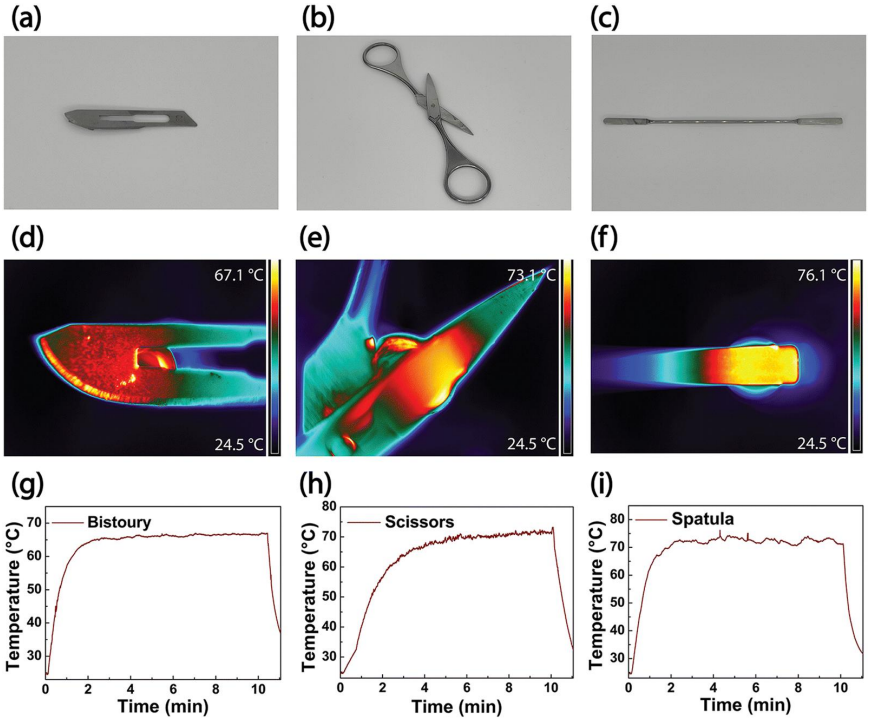

Figure 28: White light-triggered photothermal disinfection of biomedical tools using Au NRs substrate as a nanotransducer. Three metallic devices were used for the disinfection experiments: (a) a bistoury, (b) scissors and (c) a spatula. They were adhered to the plasmonic platform reaching high temperatures of (d) 69.9°C, (e) 65.4 °C and (f) 68.3 °C, respectively. (g-i) Time-temperature profiles are shown for the three corresponding devices. Reproduced under terms of the CC-BY-NC 3.0 license. [61] 2023, Zaccagnini et al., published by Royal Society of Chemistry (RSC).

The disinfection capability of the plasmonic platforms is transferred to the biomedical tools surface through heating conduction. Indeed, the Au NRs substrate was irradiated under white light source at 14.7 W cm^{-2} for 10 min while it was in close contact with the metallic surface to be disinfected. The thermal camera recordings show a uniform temperature distribution on the

back of the tools to verify the heat distribution through the thickness of the devices, varying based on their thickness and shape. High temperature values are recorded on all the monitored surfaces reaching 67.1 °C, 73.1 °C and 76.1 °C for the bistoury, the scissors and spatula disinfection, respectively (**Figure 28d-f**). The corresponding time-temperature profiles are depicted in **Figure 28g-i**: thicker tools require more time to rise the temperature. Indeed, while the irradiated bistoury and spatula reach the maximum temperature after 2 min of white light irradiation, the thicker scissors take almost 5 min. These experimental outputs prove the ability of Au NR substrates to achieve on-demand disinfection of biomedical tools: the maximum temperature values and the heating distribution are suitable for bacterial disinfection as previously demonstrated (**Figure 26**). Despite the efficiency, versatility and sustainability of the described mechanism (also suitable for viral thermal disinfection), the involved white light power density is relatively high thus aiming to improve the broadband light absorption and photothermal conversion exploiting the photothermal properties of the realized hybrid heterostructures (**Section 4.2.2**) for the construction of smart nanostructures.

4.3.2 Broadband light supplied medical devices

Section 4.2.2 and **4.2.3** highlight the crucial role of Ag@Au NPs in the visible range absorption as a colloidal dispersion and even when it is deposited on the PSSC anode giving rise to exceptional photothermal and photoelectric conversion throughput. The investigated relatively improved photoelectric efficiency of PSSCs opens up the possibility for their application in the biomedical field for the supply of electronic medical devices. To do so, a voltage of at least 1.5 V is required.

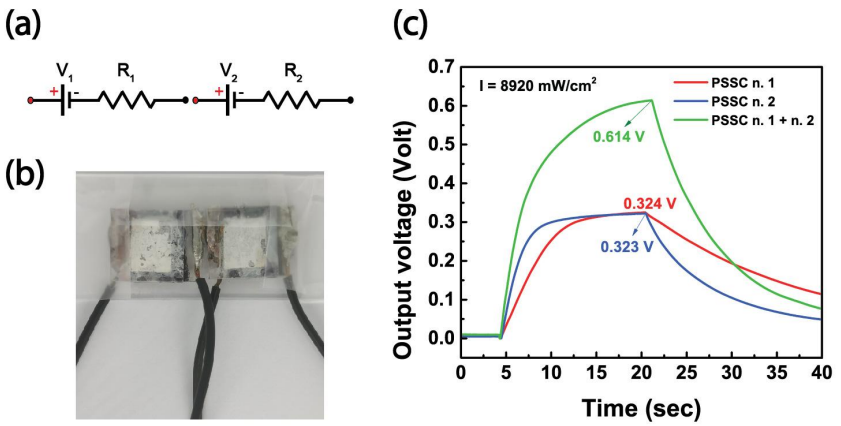

Figure 29: Photoelectric characterization of two PSSCs connected in series under white light irradiation. (a) Schematic of the equivalent circuit of the two PSSCs connected in series as in photo (b). (c) Output voltages as a function of time of the individual PSSCs (red and blue curve) and of their series combination (green curve) under white light source irradiation.

The first attempt involved the connection in series of multiple PSSCs allowing the combination of their output voltages. Indeed, the opposite charged terminals of the single PSSCs were linked together to realize the circuit depicted in **Figure 29a**. The white light irradiation was performed using the optical setup schematized in **Figure 20b**. The optical fiber output of the white light source is located at 25 mm of distance to irradiate both the PSSCs (**Figure 29b**) at 8290 mW cm^{-2} (instead of the 10 mm required for the single PSSC). The output maximum voltage of the single PSSCs in this experimental configuration were lowered to 0.323 V ± 0.015 V and 0.324 V ± 0.016 V while their combination provides 0.614 V ± 0.030 V which is almost the sum of the individual contributions (**Figure 29c**). These data point out that it is possible to enhance the total output voltage by integrating multiple PSSCs together but at the same time it is challenging to find the optimal distance of the PV cells from the white light optical fiber to achieve the highest possible voltage given by the complete irradiation of their active

areas. Considering these limitations of the white light photothermal setup and the lack of NIR wavelengths in the emission spectrum of the white light source, the performance of the PSSCs was evaluated under natural sunlight irradiation. The use of the solar renewable energy source could offer higher environmental sustainability and lower maintenance costs.

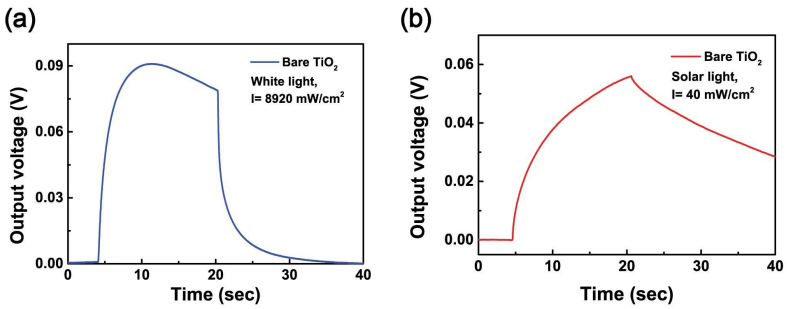

Figure 30: (a) White light and (b) sunlight irradiation of the realized PV cells having the anode composed of bare TiO_2 semiconductor layer.

At first, control experiments were performed to investigate the photoelectric response of the bare TiO_2 under both white light and sunlight irradiations. The semiconductor layer can absorb light in the UV range and its contribution must be evaluated. Maximum output voltages of 0.091 V ± 0.005 V and 0.056 V± 0.003 V were recorded for PSSC irradiation under white light (**Figure 30a**) and sunlight (**Figure 30b**), respectively. These values are 83.8% and 87.6% lower than those of the irradiated PSSCs in the same experimental conditions, thus proving their negligible role.

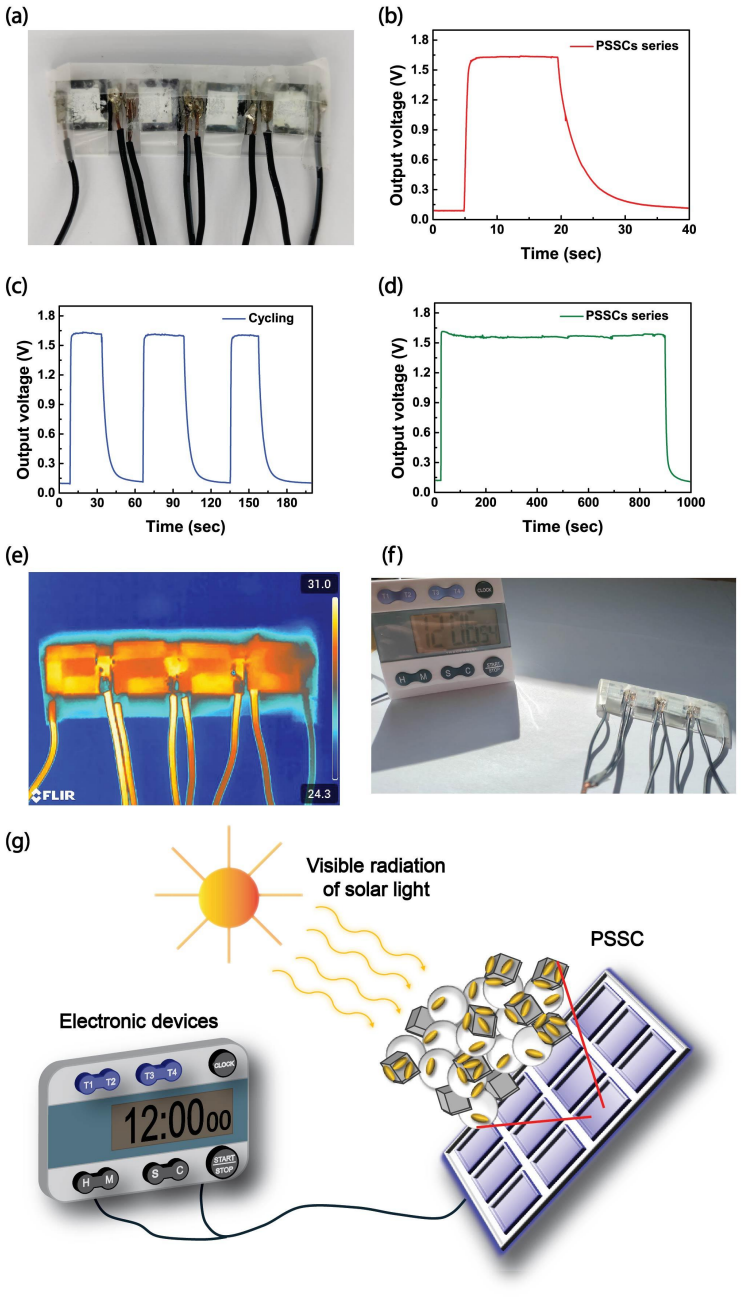
(a)
(b)
PSSCs series
Output voltage (V)
Time (sec)
(c)
Cycling
Output voltage (V)
Time (sec)
(d)
PSSCs series
Output voltage (V)
Time (sec)
(e)
31.0
24.3
FLIR
(f)
(g)
Visible radiation
of solar light
PSSC
Electronic devices
12:00

Figure 31: Photoelectric and photothermal response of PSSCs series under sunlight irradiation.
(a) Photo and (b) the obtained output voltages of the four PSSCs connected in series irradiated under solar light. (c) Cycling and (d) stability measurements of their photoelectric response. (e) Photo and (f) schematic of the PSSCs connected in series exploiting the sunlight irradiation to properly power an electronic device with a liquid crystal display.

Sunlight-triggered experiments were conducted on four PSSCs connected in series (**Figure 31a**) irradiated by natural solar light at 40 mW cm^{-2} corresponding to the 40% of AM1.5G solar irradiance and thus simulating conditions of reduced or diffuse sunlight. At first the cells were covered with a lid for 5 sec and then it was removed allowing sunlight irradiation of the PSSCs active areas. The maximum output voltage of 1.64 V ± 0.09 V was rapidly reached after 15 sec of irradiation (**Figure 31b**). Cycling experiments, performed by sequentially covering and uncovering the PSSCs with the lid, proved the reversibility of the system obtaining almost the same output voltage of ~1.64 V after each cycle (**Figure 31c**). Moreover, a long sunlight irradiation of 15 min proved the high stability of the photoelectric performance (**Figure 31d**). The collected thermographic images reveal a moderate temperature increase even after 15 min of sunlight irradiation to 31 °C (**Figure 31e**). PSSCs show enhanced stability and reversibility, high output voltages and a limited temperature increase that prove and preserve their outstanding performance. The PSSCs photoelectric efficiency was calculated considering a sunlight intensity of 40 mW cm^{-2}, an average output voltage of 0.45 V ± 0.03 V and a photocurrent of 25 μA. The value of 0.044% is obtained exceeding the efficiency of the literature of 0.016%.[87] The photoelectric efficiency of the realized system is 2.75 times higher than previous work due to the improved NPs deposition protocol and the absorption enhancement provided by the hybrid heterostructures.
As a proof of concept, the power supply of a medical device is simulated considering an electronic device with a liquid crystal

display as a model. As a result, the 1.5 V battery of a laboratory chronometer was removed and substituted with the PSSCs series shown in **Figure 31a**. In the initial state, when the PSSCs are covered by the lid the chronometer is turned off. Once the lid is removed, the PSSCs are irradiated by sunlight and reach an output voltage sufficient to power the electronic device. **Figure 31f** shows the proper functioning of the chronometer that displays accurate values. Furthermore, repeated cycles of covering and uncovering the PSSCs produce the switching off and on of the electronic device. These experimental results demonstrate the capability of the realized highly efficient and functional PSSCs to directly power electronic devices. The presented innovative, low cost and sustainable PV system enables the exploitation of renewable energy sources for the supply of medical instruments in healthcare facilities in extreme conditions such as field hospitals. This work paves the way for the employment of our technological capabilities in tandem PV systems or in power beaming applications[88] combining our system with laser wavelength sources at 1.06 μm.

4.3.3 Reusable FFP2 face mask

The outstanding properties of the realized hybrid heterostructures are here exploited to develop a new generation of photothermal-assisted and reusable face mask employing a common and safe white light source. The development of advanced PPE leveraging MNP properties necessitates the use of biocompatible dispersions to ensure both safety and functionality. For this reason, we evaluate the responsivity of epithelial cells interacting with hybrid heterostructure before depositing Ag@Au NPs on the fibers of an already highly efficient FFP2 face mask to achieve its white light-triggered photothermal disinfection. To do so, cytometric cytotoxic essay was performed on keratinocyte human cell line HaCaT exposed to different Ag@Au dilutions from 1:50 to 1:1650 starting from the initial 0.0378 mg mL^{-1} colloidal dispersion.

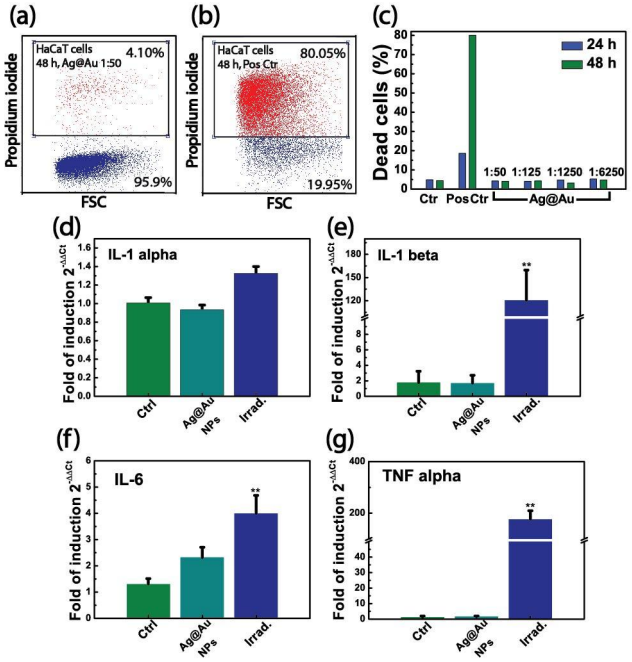

Figure 32: Effect of the hybrid heterostructures on keratinocytes in terms of viability and inflammatory response. Percentage of dead cells after 48 h of treatment with both (a) bare and (b) irradiated Ag@Au NPs. (c) Dead cells percentage after 24 h and 48 h of 1:50, 1:125, 1:1250, 1:6250 Ag@Au NPs treatment, freeze-thaw treatment used as positive control or left untreated as negative control. The production of proinflammatory cytokines (d) IL-1α, (e) IL-1β, (f) IL-6 and (g) TNF-α in HaCaT cells treated with irradiated (Irrad), not irradiated Ag@Au NPs or left untreated (Ctrl) was quantified by Real-Time RT PCR. The difference between groups was analyzed by One-way ANOVA test with Dunnett's multiple comparison test (** $p < 0.05$). Reproduced with permission. [62] 2024, Wiley-VCH GmbH.

The Propidium Iodide uptake revealed the percentage of dead cells 24 h and 48 h after the treatment. **Figure 32a-c** show that the presence of Ag@Au NPs in 1:50 dilution did not significantly affect the viability of the epithelial cells. Indeed, a mortal rate of 4% is achieved, comparable to the untreated cells (negative control). The positive control, given by freeze-thaw treatment,

provides a percentage of dead cells of 80.0%. **Figure 32c** summarizes these results highlighting the biocompatibility of Ag@Au NPs. Additionally, the induction of inflammatory response was evaluated by Real-Time RT-PCR by measuring the mRNA levels of the inflammatory cytokines IL-1α (interleukine-1 alpha), IL-1β, IL-6 and TNF-α (tumor necrosis factor) after the treatment with not irradiated and irradiated Ag@Au NPs. Apart from IL-1α response (**Figure 32d**) that is not upregulated in all the examined conditions, IL-1β, IL-6 and TNF-α present high values for the treatment with irradiated hybrid heterostructures proving an inflammatory response (**Figure 32e-g**). The cytokines inflammatory response indicates the release of Ag^+ ions that could further enhance the desired photothermal face mask disinfection and that can be effectively isolated from direct skin contact through specific structural modifications.

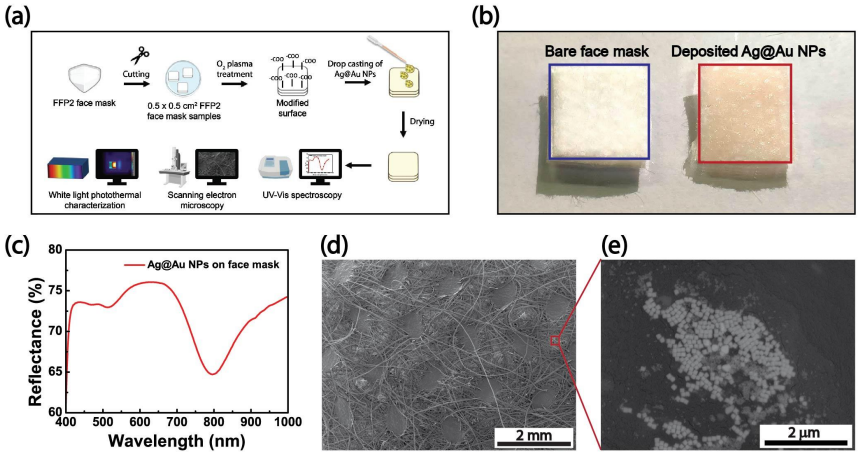

Figure 33: Functionalization of FFP2 face mask with Ag@Au NPs. (a) Schematics of the production process and of the optical and morphological characterization techniques. (b) Representative photos of specimens composed of bare FFP2 face mask (left) and of a functionalized one (right). (c) Diffuse reflectance spectrum of Ag@Au FFP2 face mask. (d) SEM micrographs of the plasmonic face mask with (e) a magnification of the hybrid heterostructures on its fibers. Reproduced with permission. [62] 2024, Wiley-VCH GmbH.

Next step involves the FFP2 functionalization with the Ag@Au NPs dispersion. The hydrophobicity of the FFP2 surface hinders the deposition of NPs. As a result, there is plenty of works focusing on nanomaterials on surgical face masks, easier to be treated. We overcame this challenge performing oxygen plasma treatment on the FFP2 face mask surface. As a result, its hydrophobicity lowers and the plasmonic colloidal dispersion can percolate.[89] The adopted protocol (**Figure 33a**) includes, at first, the cutting of the FFP2 face mask into 1 cm x 1 cm pieces, then they were treated with oxygen plasma and finally the Ag@Au NPs dispersion was deposited by drop casting covering homogeneously the entire surface. The obtained samples are left to dry at room temperature. The presence of MNPs on the functionalized face mask is at first visible to the naked eye since it acquires the typical reddish hue of the corresponding colloidal dispersion (**Figure 33b**) but further characterization is required for deeper investigation. The optical characterization of the plasmonic FFP2 face mask was conducted using UV-visible spectroscopy in diffuse reflectance mode: the Ag@Au NP absorption peaks are still visible with 11.35% intensity of the LSPRl peak of Au NRs and 3.11% intensity of the Ag NCs dipole peak (**Figure 33c**). Moreover, SEM micrographs reveal the presence of densely packed Ag@Au NPs on the fiber of the face mask still maintaining their geometry (**Figure 33d-e**).

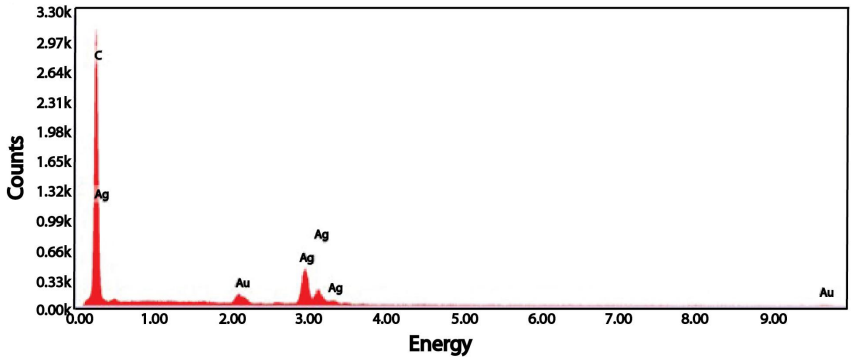

Figure 34: EDS spectroscopy of the Ag@Au FFP2 face mask. Reproduced with permission. [62] 2024, Wiley-VCH GmbH.

The chemical composition of the treated face mask is analysed by Energy Dispersive X-Ray Spectroscopy (EDS) that highlights the presence of Au and Ag strong and evident signals (**Figure 34**). Once the presence of Ag@Au NPs on the face mask fibers has been confirmed, it is necessary to assess the possibility of their accidental release. To do so, the structural stability of the plasmonic face mask was tested upon prolonged stress treatments. Indeed, two different techniques were considered.

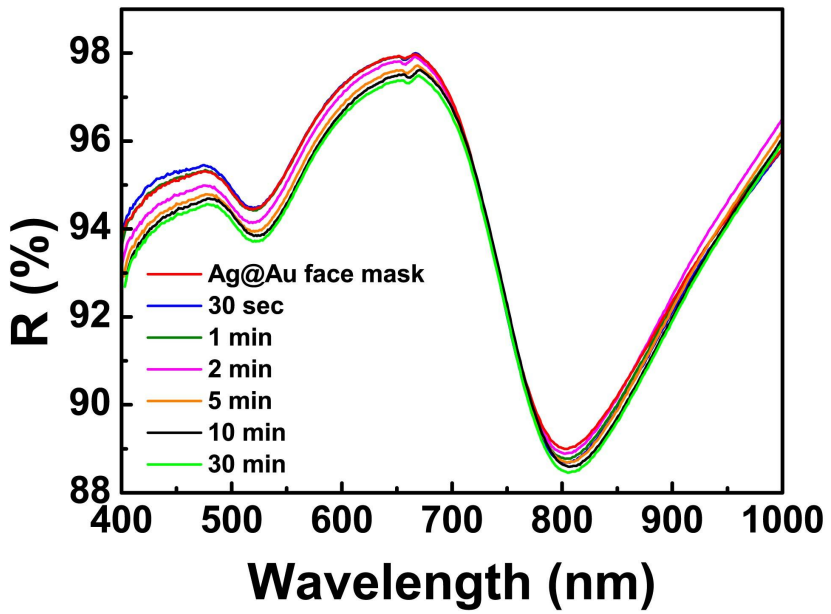

Figure 35: NPs leakage test from the functionalized face mask exposed to a flow of medical compressed air. Reproduced with permission. [62] 2024, Wiley-VCH GmbH.

At first the functionalized FFP2 face mask was fixed in a squared frame and sprayed with medical compressed air by a high quality dry compressor for different time intervals from 30 sec to 30 min. **Figure 35** shows the UV-visible absorption spectra acquired after each test performed on the sample to evaluate possible variation of the Au NRs spectroscopic features. The position and the intensity of the LSPRl peak remains unchanged even after the longer exposures to airflow. The second employed technique was more invasive since the Ag@Au face mask was immersed in MilliQ water for different time intervals from 10 sec to 2h. Different plasmonic specimens were used, one for each immersion, and were optically characterized before and after the treatment. The absorption spectra shown in **Figure 36** highlight that the spectrum

change after every immersion maintaining the plasmonic bands still visible.

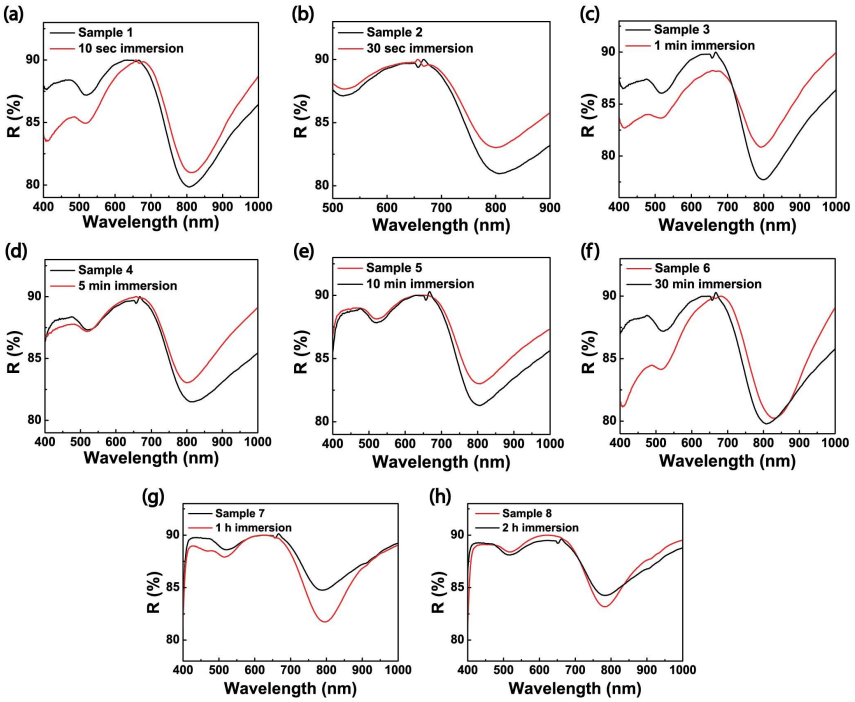

Figure 36: NPs leakage test from the functionalized face mask immersed in MilliQ water. Six different specimens were immersed in a volume of MilliQ water for (a) 10 sec, (b) 30 sec, (c) 1 min, (d) 5 min, (e) 10 min, (f) 30 min, (g) 1 h and (h) 2 h. Diffuse reflectance spectra were acquired before and after the treatment. Reproduced with permission. [62] 2024, Wiley-VCH GmbH.

However, the intensity change of the LSPRl band is not relatable to the time interval of immersion but rather to the deterioration caused by the treatment. The spectra of sample 6 in **Figure 36f**, acquired before and after 30 min of immersion, exhibit the same optical signal variation as the spectra of Sample 1 in **Figure 36a** acquired before and after 10 sec of immersion. They present 11.23% and 4.4% of reduction in the LSPRl band intensity, respectively. The samples that were immersed for 30 sec, 1 min, 5

min, and 10 min exhibit reductions of 22.9%, 25.3%, 18.2%, and 19.8%, higher than the cases previously described but always maintaining the plasmonic peaks still visible. In particular, the spectra of samples 2, 3 and 5, taken before and after the immersion, perfectly overlap. For the longest immersions in water of 1 h and 2h (**Figure 36g-h**), a significant change in the LSPRl intensity is noticeable. The spectrum uptick indicates a surface modification given by the removal of the outer surface layers that leads to the increased exposure of the Ag@Au NPs on the surface amplifying the percentage of reflectance. To summarize, the leakage tests validate the stability of the functionalized face mask and its resilience against prolonged mechanical stimuli.

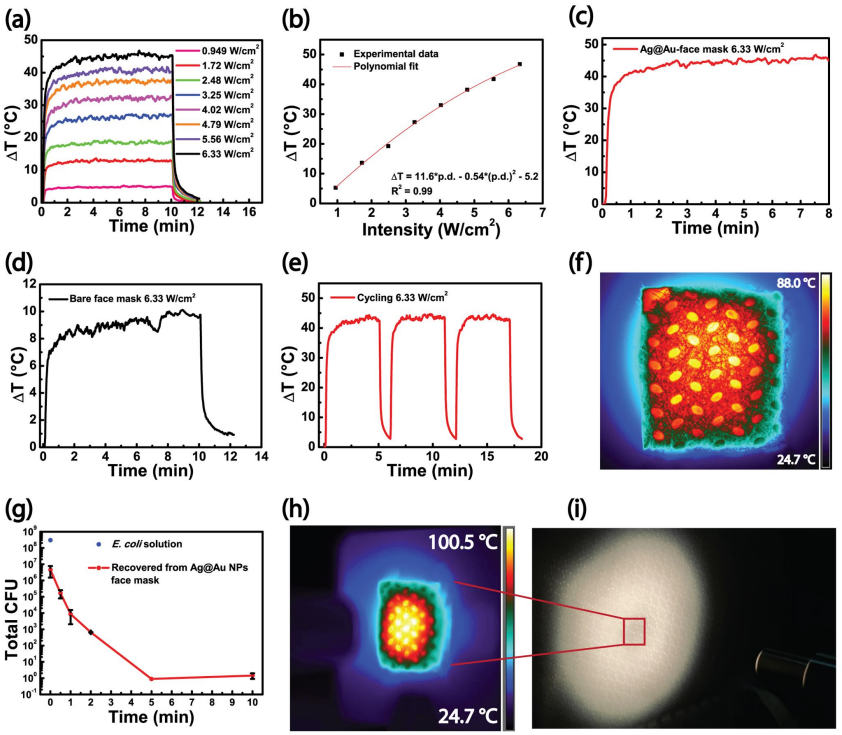

Figure 37: White light photothermal characterization and disinfection of the Ag@Au FFP2 face mask. (a) Time-temperature plots of the irradiated Ag@Au FFP2 face mask at different intensity values of the white light source. (b)

Temperature variation as a function of the intensity values ranging from 0.949 W cm^{-2} to 6.33 W cm^{-2}. Time-temperature plots of the (c) functionalized and of (d) the bare FFP2 face mask under white light irradiation at 6.33 W cm^{-2}. (e) Cycling measurements to investigate the stability and the reversibility of the photothermal response. (f) Thermographic image of the irradiated Ag@Au FFP2 face mask at the highest achieved temperature. (g) White light photothermal disinfection experiments performed on Ag@Au FFP2 face mask specimens contaminated with *E. coli* solution. They were irradiated by white light source for 0.5, 1, 2, 5 and 10 min at 6.33 W cm^{-2}. (h) Representative thermographic image of the Ag@Au FFP2 face mask at the highest achieved temperature. (i) Ag@Au FFP2 face mask irradiated by the white light source through the optical fiber that produces a highly uniform irradiation process. Reproduced with permission. [62] 2024, Wiley-VCH GmbH.

After the illustrated controls on the Ag@Au NPs biocompatibility with epithelial cells and on their proper immobilization on the FFP2 fibers, the photothermal response of the functionalized face mask was investigated under the white light source irradiation (**Figure 37a**). The time-temperature profile was recorded irradiating the Ag@Au face mask for 10 min at different intensity values ranging from 0.949 to 6.33 W cm^{-2}. Confirming the correlation between temperature increase and intensity of the light source (**Figure 37b**). Since an average temperature exceeding 70 °C was required to perform photothermal disinfection treatments, the white light intensity of 6.33 W cm^{-2} was selected for the following experiments. Indeed, the selected intensity lead to a temperature increase after 10 min of white light irradiation on the plasmonic FFP2 surface of 46 °C from 26 °C to 72 °C (**Figure 37c**). As a control, the bare face mask was irradiated in the same experimental conditions achieving a lower temperature increase of 10 °C (**Figure 37d**). Cycling measurements (**Figure 37e**) instead proved the face mask thermal stability and the process reversibility. The heating profile was analysed and recorded through the IR thermal camera. The thermographic image of the functionalized face mask irradiated under white light source at 6.33 W cm^{-2} reveals a homogeneous heating distribution due to the uniform deposition of the hybrid heterostructures (**Figure 37f**). These

results provide a high photothermal efficiency value of the Ag@Au FFP2 face mask of 68.8%.
The performance of this device for photothermal bacterial disinfection was then evaluated. *E. coli* was selected as model pathogen to simplify the experimental setting up, avoiding more dangerous microorganisms. It enables to build a process flow easily adaptable to a wide range of bacterial or virus types. At first, multiple specimens of the plasmonic face mask were fabricated and intentionally contaminated with a microbial solution of *E. coli* cells 3 x 10^8 CFU. After 10 min of immersion in the microbial solution, the average number of bacteria recovered from a single specimen at the initial state was 4.6 x 10^6 CFU. The contaminated Ag@Au face mask specimens were irradiated under white light source at 6.33 W cm^{-2} for different time intervals.

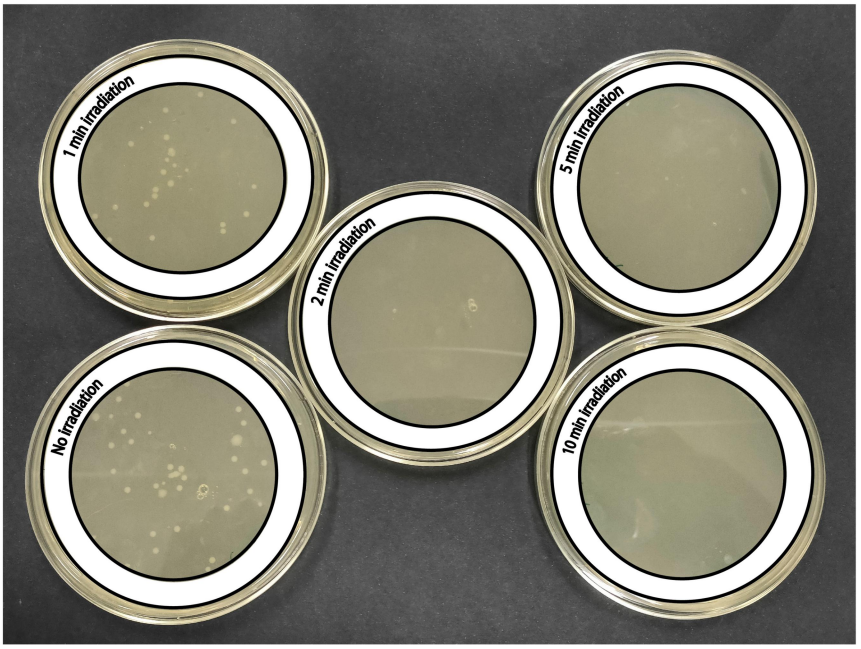

Figure 38: Photo of the plating on LB agar plates with the bacteria recovered from the contaminated and then irradiated face mask specimens, after 1 min, 2 min, 5 min and 10 min of treatment. Reproduced with permission. [62] 2024, Wiley-VCH GmbH.

Then, the plate counting method was employed to quantify the survival of the extracted bacterial cells (**Figure 38**). The CFU of the recovered *E. coli* cells were 1.6 x 10^5 CFU, 8.7 x 10^3 CFU, 0.6 x 10^3 CFU, 0.9 CFU and 1.45 CFU after 30 sec, 1 min, 2 min, 5 min and 10 min of white light irradiation, respectively (**Figure 37g**). To summarize, the number of recovered CFU decreases with the increase of irradiation time. After 5 min of thermal treatment, the cell viability dropped from 4.6 x 10^6 CFU to 1 CFU, six order of magnitude lower through the plate counting method. The thermographic image of the irradiated plasmonic face mask under white light source is depicted in **Figure 37h**. The photothermal disinfection treatment can be performed even on larger areas of functionalized FFP2 face mask using the optical fiber of an uncollimated white light source (**Figure 37i**). The achieved *E. coli* inactivation of 6 logs highly exceeds previous works employing MNPs for bacterial disinfection. Indeed, Annesi et al. reported a 2 log reduction in bacterial viability exploiting the photothermal effect of Au NPs under resonant light irradiation.[86] Our achievement is close to the effect induced by high intensity UV light pulses as reported by Rowen et al. However, they also found out different responses of gram-positive and gram-negative bacteria to UV light not enabling the same results on different strains.[90] In addition to its high efficacy against all bacterial and viral microorganisms, this novel technology allows for complete disinfection of the Ag@Au FFP2 face mask to be achieved within a timeframe of only a few minutes constituting a functional benefit for real-life applications.

During the photothermal disinfection treatments, IR thermography was used to monitor the plasmonic FFP2 face mask temperature. The thermal camera recorded the maximum temperature increases of 45.4 °C, 48.6 °C, 52.6 °C, 55.3 °C and 56.7 °C for each rising irradiation time interval on the face mask surface (**Figure 39a**).

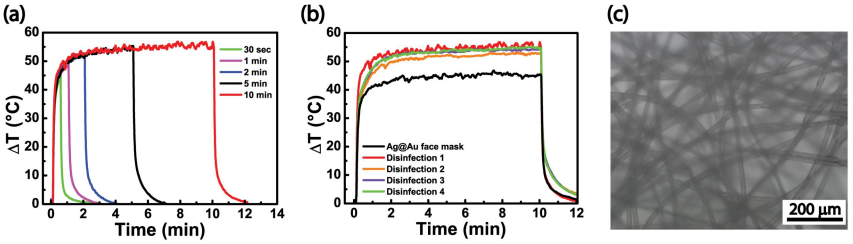

Figure 39: (a) Time-temperature plots recorded during the photothermal disinfection treatments. (b) Time-temperature plots recorded for the uncontaminated and for four consecutive contamination/disinfection cycles on Ag@Au FFP2 face mask. (c) Contrast phase microscopy of the contaminated Ag@Au FFP2 face mask. Reproduced with permission. [62] 2024, Wiley-VCH GmbH.

The depicted technology enables the reusability of the plasmonic FFP2 face mask. Indeed, four cycles of contamination and subsequent photothermal disinfection demonstrated to not compromise the photothermal properties of the plasmonic face mask providing long-term reusability (**Figure 39b**). Other techniques such as contrast phase microscopy were not used since they could not detect bacteria adsorbed by the inner layers (**Figure 39c**). Moreover, it is worth noting that after 10 min of white light irradiation the plasmonic FFP2 face mask reached average and maximum temperatures of 82.9 °C and 100.5 °C, respectively. Those values are 11.4 °C and 12 °C higher than the recorded ones on not contaminated specimens. These results can be explained by the change of the optical properties of the plasmonic face mask.

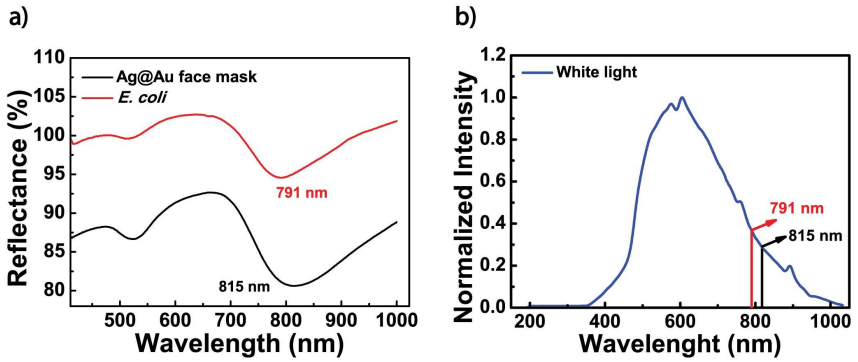

Figure 40: (a) Diffuse reflectance spectroscopy performed on Ag@Au face mask before (black curve) and after (red curve) the microbial contamination. (b) Emission intensity spectrum of the white light source highlighting the blueshift due to the microbial contamination of the plasmonic face mask and the corresponding higher light intensity to be absorbed. Reproduced with permission.[62] 2024, Wiley-VCH GmbH.

Indeed, the LSPRl peak blueshifts of 24 nm after the *E. coli* contamination (**Figure 40a**) which results in a higher intensity of the absorbed light (+23.9%, **Figure 40b**). As a result, the heating effect was increased of the 16%.

The paradigm change proposed in this work overcomes the common limitations not only of other face mask disinfection methods but also of the existing MNP technologies that usually require complex light sources, specialized staff and expensive production and maintaining procedures. Indeed, the realized Ag@Au FFP2 face mask is an environmentally sustainable device that can be reused after the non-hazardous white light-triggered disinfection procedure avoiding the dispersion of contaminated material in the environment. Our achievement represents a unique opportunity in healthcare facilities and for PPE at home.

4.3.4 Metasurface-based colorimetric biosensor integrated into FFP2 face mask

To enhance the functionality of the mask, we aim to incorporate a miniaturized biosensor onto its surface, capable of detecting hazardous agents upon contact and generating a real-time colorimetric warning signal visible to the naked eye. To do so, an optical metasurface biosensor was employed. The selected bottom-up plasmonic metasurface, whose production process and characterization are highly described in **Section 4.1.4**, exhibits higher sensitivity to the surrounding medium variation compared to more conventional plasmonic structures due to the SLRs.[91] It is possible to bioactivate the plasmonic metasurface with a monoclonal antibody to selectively recognize specific microorganisms interacting with its surface and convert this biological detection into an optical signal, namely the spectral shift of the SLR band, visible to the naked eye. The realized metasurface is composed by an array of Ag NCs separated from a thin Au layer only by an ultra-thin dielectric spacer, the polyelectrolyte multilayer. The SEM micrograph, in **Figure 41a**, reveals an even distribution of Ag NCs on the entire surface area due to the employed immersive eLbL method.

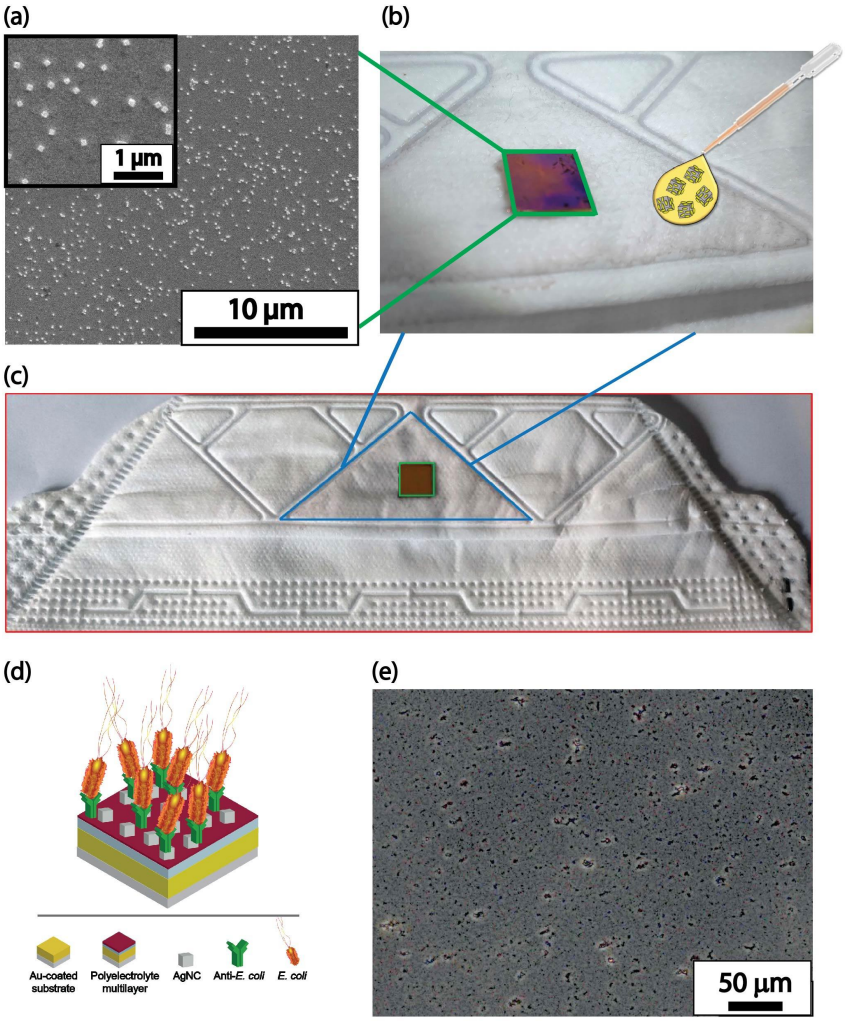

Figure 41: Integrated optical metasurface as colorimetric biosensor. (a) SEM micrograph of the plasmonic metasurface. (b) The bioactivated metasurface biosensor is integrated in the middle of the Ag@Au FFP2 face mask that exhibits a reddish appearance compared to the bare face mask (c). (d) Schematic of the working mechanism of the metasurface biosensor. (e) Contrast phase micrograph of the contaminated biosensor with *E. coli* cells. Reproduced with permission. [62] 2024, Wiley-VCH GmbH.

The realized multifunctional FFP2 face mask combines the properties of the Ag@Au NPs deposited on its fibers and of the optical metasurface (highlighted by green outlines in **Figure 41b**) integrated in the middle of the face mask (**Figure 41c**). The central triangular-shaped area of the functionalized Ag@Au face mask shows a reddish appearance compared to the bare face mask (highlighted by blue outlines in **Figure 41c**). The biosensor working mechanism relies on the antigen-antibody recognition mechanism (**Figure 41d**): the metasurface is bioactivated with a monoclonal antibody that univocally interacts with a specific target pathogen, producing a refractive index change in the metasurface surrounding medium. The microbial contaminations are analyzed though UV-visible specular reflection spectroscopy to quantify the SLR band shift due to the pathogens interaction.
The integrated metasurface immunosensor is bioactivated with anti-*E. coli* 1011 to selectively recognize *E. coli* cells, employed as model bacterium and sprayed on the metasurface biosensor. SEM micrograph in **Figure 41e** reveals the presence of bacteria on the analyzed samples. The microbial solution was sprayed on the metasurface to mimic respiratory droplet dispersion causing face mask infection (**Figure 42a**). The spectroscopy investigation shows an absorption deep corresponding to SLR mode at 773 nm (blue curves in **Figure 42b-f**). This value in then redshifted of ~14 nm after the physisorption of anti-*E. coli* 1011 to confirm the successful bioactivation of the metasurface (red curves in **Figure 42b-f**). The sensitivity of the realized biosensor is investigated spraying *E. coli* solutions with different concentrations and recording the corresponding shift of the SLR absorbance deep. Microbial concentration of 10^3 CFU mL^{-1} (**Figure 42b**), 10^2 CFU mL^{-1} (**Figure 42c**), 10 CFU mL^{-1} (**Figure 42d**), 10^0 CFU mL^{-1} (**Figure 42e**) and 10 CFU 100^{-1} mL^{-1} (**Figure 42f**) were used resulting in absorption peak redshifts of 13 nm, 11 nm, 9 nm, 7 nm and 4 nm, respectively (green curves in **Figure 42b-f**). These results are summarized in the calibration curve of **Figure 42g**,

reporting the spectral shift as a function of the used *E. coli* concentration. The calculated low detection limit (LOD) of 1 CFU 100^{-1} mL^{-1} exceeds by two orders of magnitude other optical metastructure biosensors found in literature.[92]

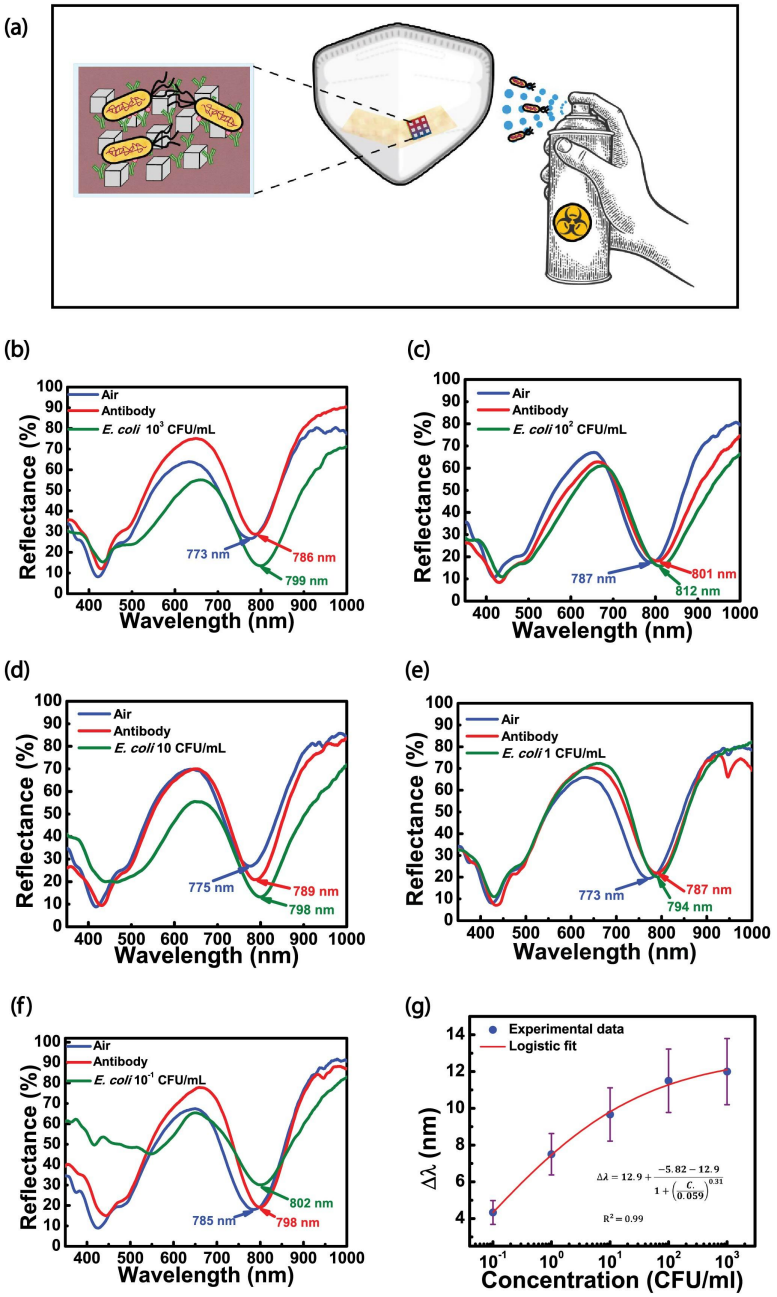
(a)
(b)
Air
Antibody
E. coli 10³ CFU/mL
773 nm
786 nm
799 nm
Reflectance (%)
Wavelength (nm)
(c)
Air
Antibody
E. coli 10² CFU/mL
787 nm
801 nm
812 nm
Reflectance (%)
Wavelength (nm)
(d)
Air
Antibody
E. coli 10 CFU/mL
775 nm
789 nm
798 nm
Reflectance (%)
Wavelength (nm)
(e)
Air
Antibody
E. coli 1 CFU/mL
773 nm
787 nm
794 nm
Reflectance (%)
Wavelength (nm)
(f)
Air
Antibody
E. coli 10⁻¹ CFU/mL
785 nm
802 nm
798 nm
Reflectance (%)
Wavelength (nm)
(g)
Experimental data
Logistic fit
Δλ = 12.9 + (−5.82 − 12.9) / (1 + (C / 0.059)^0.31)
R² = 0.99
Δλ (nm)
Concentration (CFU/ml)

Figure 42: Metasurface biosensor sensitivity to different concentrations of *E. coli* solution. (a) Schematic of metasurface biosensor working mechanism integrated on the FFP2 face mask. (b-f) Specular reflection spectroscopy revealed the absorption depth shifts due to the employed *E. coli* concentrations of 10^3 CFU mL^{-1}, 10^2 CFU mL^{-1}, 10 CFU mL^{-1}, 10^0 CFU mL^{-1} and 10^{-1} CFU mL^{-1}. (g) Calibration curve of the metasurface biosensor. Reproduced with permission. [62] 2024, Wiley-VCH GmbH.

Beyond its excellent sensitivity, the biosensor also demonstrates high specificity and versatility in detection.
The specificity of the metasurface biosensor is ascribable to the unique structure of monoclonal antibodies. Indeed, a monoclonal antibody is designed to recognize and bind a single epitope with high specificity and affinity. As a result, antigen epitope and antibody exhibit intense interacting forces.

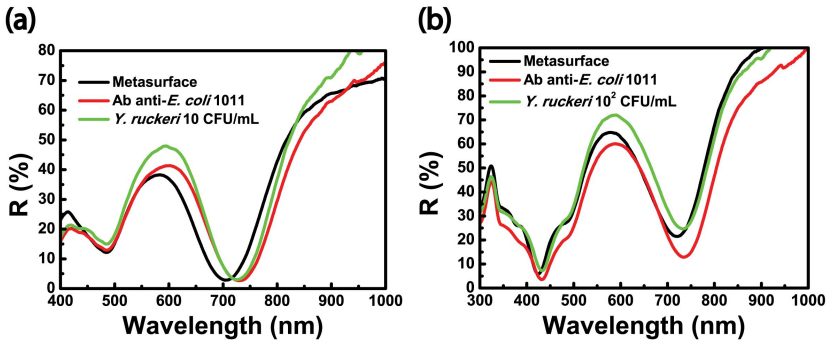

Figure 43: Selectivity test of the metasurface biosensor that was bioactivated with anti-*E. coli* 1011. The biosensor was tested against two bacterial concentrations of *Y. ruckeri*, (a) 10 CFU mL^{-1} and (b) 10^2 CFU mL^{-1}. The specular reflection spectra are reported. Reproduced with permission. [62] 2024, Wiley-VCH GmbH.

To demonstrate the ability of the metasurface biosensor to recognize exclusively the pathogen of interest, the metasurface was, at first, bioactivated with anti-*E. coli* 1011 through physisorption

and then tested with a solution of *Yersinia (Y.) ruckeri*. Indeed, *Y. ruckeri* cells were sprayed on the bioactivated metasurface analyzing two concentrations, 10 CFU mL^{-1} and 10^2 CFU mL^{-1}. The specular reflectance spectroscopy performed on the two investigated samples revealed thes fist redshift of 25 nm (red curve in **Figure 43a**) and 15 nm (red curve in **Figure 43b**) due to the bioactivation with the antibody. The subsequent contaminations with *Y. ruckeri* only produce a blueshift of 4.3 nm (green curve in **Figure 43a**) and 1.2 nm (green curve in **Figure 43b**) using 10 and 10^2 CFU mL^{-1}. These results assure experiments selectivity since anti-*E. coli* 1011 is unable to recognize other bacteria than the target pathogen.

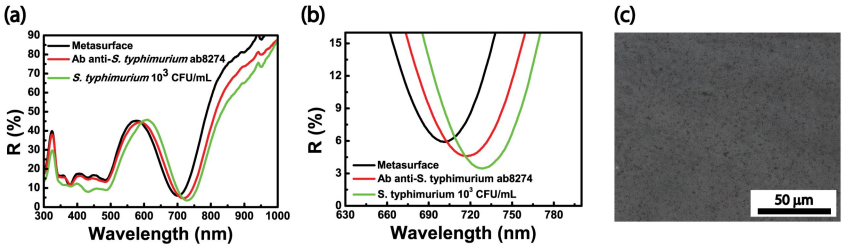

Figure 44: Versatility test of the metasurface biosensor. It was bioactivated with a different monoclonal antibody, Ab anti-*S. typhimurium ab8274* and then contaminated with 10^3 CFU mL^{-1} of *S. Typhimurium* solution. (a) The specular reflection spectra are reported with (b) a close-up of the reported deeps. (c) Contrast phase microscopy of the contaminated plasmonic metasurface. Reproduced with permission. [62] 2024, Wiley-VCH GmbH.

To evaluate the functional versatility of the proposed biosensor, we employed the physisorption method for antibody immobilization, taking advantage of its inherent adaptability to different biomolecular interfaces. Indeed, a different monoclonal antibody Ab anti-*Salmonella (S.) Typhimurium ab8274* was selected to bioactivate the plasmonic metasurface. The physisorption process produces a redshift of 16.2 nm (red curve in **Figure 44a**). Then, the *S. Typhimurium* solution 10^3 CFU mL^{-1} was sprayed on the

bioactivated metasurface producing a further redshift of 11 nm (green curve in **Figure 44a**). This optical signal, highlighted in the zooming of **Figure 44b**, along with the contrast phase micrograph (**Figure 44c**) of the contaminated metasurface highlight the ability of the biosensor to detect different bacterial strains at a given microbial concentration, paving the way for multiplexed analytical measurements.

The reported technology paves the way for rapid and facile detection of pathogens. The employed bottom-up eLbL technique reduces construction costs and eliminate the common scalability issues of lithography-based metasurfaces.

4.4 Conclusions

This thesis focuses on the remarkable capability of plasmonic nanomaterials to interact with broadband light sources and explores their applications in various healthcare fields. The primary idea is to develop innovative, sustainable and efficient technologies. The originality of this work lies in the paradigm shift from using monochromatic light sources, such as lasers, to conventional, broadband light sources, which are more sustainable and accessible. This compelling transition, paves the way for integrating nanotechnologies into the biomedical field by addressing challenges such as high costs, limited environmental sustainability, and the operational complexity of existing devices.

Anisotropic plasmonic NPs composed of noble metals such as Au and Ag were chosen for their excellent biocompatibility, which makes them suitable for biomedical applications, their friendly surface chemistry that promotes interaction with biomolecules, and their unique optical properties arising from the LSPR effect within the visible or NIR range. The controlled deposition of these plasmonic MNPs on rigid or flexible substrates allows us to create compact and multifunctional devices by transferring the chemical and optical properties of nanomaterials from the wet to the dry state. The role of properly realized bottom-up nanostructures was analyzed and discussed for four various healthcare applications.

An array of Au NRs was fabricated and characterized to be used for the facile and on-demand white light photothermal disinfection of metallic biomedical tools such as bistouries, spatulas, and scissors. The partial absorption of NIR photons by the Au NRs array under white light illumination triggers the thermoplasmonic process. It generates heat that efficiently propagates to the adjacent surface of the biomedical tool. The increase in temperature is suitable to eliminate the intentionally deposited harmful bacterial within minutes. To improve the performance of the system, a more efficient design was implemented to obtain a broader absorption range. Hybrid plasmonic heterostructures were fabricated to combine the chemical and optical properties of two different

species: Ag NCs surrounded by several layers of Au NRs. The geometry of the hyperbranched heterostructures facilitates light absorption across the NIR and visible range while preserving the distinctive features of the two constituent nanomaterials. Next, the achieved broadband absorption was exploited to improve both photoelectric and photothermal conversion mechanisms. At first, they were deposited onto a solar cell photoanode to develop innovative PSSCs, leading to superior photostability, output voltage, and overall efficiency compared to similar photovoltaic systems reported in the literature. Then, the heterostructures were also employed to functionalize the fibers of an FFP2 face mask, conferring reusability through white light photothermal self-disinfection. The excellent photothermal conversion efficiency enables facile and on-demand disinfection of pathogens on the surface within just a few minutes of white light exposure. We further highlight the versatility of nanomaterials by adding functionalities to the face mask. To this end, a compact biosensor consisting of a bottom-up optical metasurface was integrated enabling the specific recognition of bacteria by producing a real time variation in the metasurface colorimetric signal, visible to the naked eye. The biosensor's high sensitivity enables both qualitative and quantitative detection of pathogens, achieving a LOD that is two orders of magnitude lower than those reported for previous optical sensors in the literature.

This work discusses the fabrication of bottom-up metallic plasmonic nanostructures properly designed and realized for specific biomedical applications, highlighting the versatility of the employed nanomaterials and techniques used. The extraordinary design of the proposed medical devices highlights the significant potential of plasmonic nanoparticles in the biomedical field, enabling their safe and effective use in a wide range of reusable applications. The multifunctionality and versatility of nanomaterials are enhanced by the environmental sustainability of the employed light sources, such as white light lamps or sunlight, making them suitable for everyday use in homes and medical

facilities. Future developments will focus on the fabrication of advanced nanostructures and innovative geometries, with potential applications in precision and personalized medicine.

5. Materials and Methods

5.1 Materials

Citrate-capped AuNRs with size 55 nm x 15 nm and polyvinylpyrrolidone-capped AgNCs with 100 nm diameter were purchased from Nanocomposix. Indium Tin Oxide (ITO) -coated glass slides with a sheet resistance of 70-100 Ω/sq were purchased from Sigma-Aldrich. Gold-coated glass slides of 1 cm x 1 cm and 50 nm thickness were purchased from AMSBIO. Acetone, isopropanol, methanol, sodium hydroxide (NaOH), poly(sodium 4-styrenesulfonate)(PSS, Mw B70 kDa), and poly(allylamine hydrochloride)(PAH, Mw B50 kDa) were purchased from Merck. Deionized water was used to prepare the heterostructure. TiO_2 nanopowder, 100% Anatase, was purchased from Merck. Nitric acid (HNO3), 1.1 M. NOA (Norland Optical Adhesive) glue, from Norland Products. Rhodamine B (RhB) powder was purchased from Sigma-Aldrich. KI/I_2 dissolved in a glycol electrolyte solution. *E. coli* K12 MG1655 CGSC#7740 was obtained from the Coli Genetic Stock Centre (CGSC) collection. The minimal medium E supplemented with 0.40% glucose was used for bacterial growth. The chemicals required for preparing the bacterial growth medium were purchased from Merck or VWR International. LIVE/DEADTM BacLightTM Bacterial Viability Kit for microscopy was purchased from Thermo Fisher Scientific. 3 M VFlex 9152E, FFP2 face masks (provided by 3 M) were used in the experiments.

5.2 Methods

5.2.1 Au NR arrays enable the White light-triggered Photothermal Disinfection of Medical Tools

Immobilization of AuNRs on glass substrates: The incorporation of AuNRs on glass substrates was achieved following the procedure reported in ref. [78] Briefly, 1 cm x 1 cm sized glass substrates were thoroughly washed in an ultrasonic bath for 10 min by using, sequentially, methanol and acetone. An intermediate rinsing step in isopropanol was carried out between the two washing steps. Finally, the glass substrates were stored in isopropanol, rinsed, and dried under a stream of nitrogen before use. Before fabricating the polyelectrolyte multilayer, the substrates were immersed for 30 min in a 5 M NaOH solution to impart a negative charge triggering the electrostatic incorporation of the first positively charged PE. PEs were deposited using eLbL by following the sequence: PAH-PSS-PAH. Accordingly, the building of the PE multilayer was performed by sequentially immersing the glass substrate in PAH, PSS, and PAH solutions for 10 min. In particular, the concentration of the PE solution was 1.6 mg mL^{-1}, and the pH was 2 for the PAH solution and 8 for the PSS, respectively. In-between two consecutive immersion steps, an intermediate washing step was performed (2 min immersion in water) to remove the excess of PE molecules. Finally, a final step of a 2 min immersion in water was carried out to avoid the counterion effect. The substrates were then dried under a stream of nitrogen and stored in a refrigerator (+4 1C). Subsequently, the PE functionalized glass substrates were immersed for 16 h in a colloidal dispersion of AuNRs (suitably diluted to obtain an optical density of 1 at 790 nm). After this step, the AuNRs-modified substrates were washed with water and gently dried under a stream of nitrogen before their characterization.

Sensitivity to the refractive index variation and photo-thermal

characterization: A double-face glass cell was used to investigate the optical response of the AuNR-modified substrates to the alteration of the refractive index (n) of the infiltrating medium. This configuration was suitably selected to study the optical and the PT behavior of the AuNR-modified substrates in two different conditions: (i) when only one side of the substrate underwent a n variation, and (ii) when both sides of the AuNRs substrate experienced an n variation. To this end, a cell was fabricated, such that the AuNR substrate was sandwiched between two glass slides (1.2 cm x 1.2 cm). First, to ensure a uniform 10 mm gap between the plasmonic substrate and the two glass slides, the glue NOA-61 with 10 mm glass microbeads was deposited on the corners of the AuNRs substrate on both sides. Then the AuNRs substrate was placed in between the two glass slides. After that, the cell was sealed by exposing it to UV light radiation for 1 min. At this stage, the first side of the resulting cell was infiltrated with the NOA-61 as a representative medium with a known n. Subsequently, the absorption spectrum was collected, and the PT measurements were performed. The same procedure was performed after infiltrating the second side of the double face cell.

White light disinfection: The ability of the AuNR modified substrates to achieve surface disinfection, induced by white light irradiation, was investigated utilizing *E. coli* cells as a model bacterium. AuNR substrates were immersed in 500 mL of a 10^4 CFU mL^{-1} *E. coli* cells dispersion in minimal E (with no glucose). After 30 min, the substrate, contaminated with *E. coli* cells, was dried under a stream of nitrogen. The substrate was then characterized by absorption spectroscopy and irradiated with white light (14.7 W cm^{-2} for 10 min). After irradiation, the substrates were inspected by fluorescence microscopy using propidium iodide as a staining agent. The staining was realized by immersing the sample for 10 min in 500 mL minimal E with 2 mL fluorescent dye propidium iodide. The substrate was dried under a stream of

nitrogen before microscopy analysis. Control experiments used SYTO 9^{TM} as a staining agent for identifying viable cells.

5.2.2 PSSCs for medical devices supply

***Anodes preparation*:** The anodes of the PSSC were fabricated using a conductive ITO-coated layer and TiO_2 nanopowder (100% Anatase) as the semiconductor. The ITO-coated glass slides (ITOs) were cut into 1.5 cm x 1.5 cm squares using a diamond-tipped tool. In an ultrasonic bath, the resulting substrates were washed under a fume hood with sequential methanol and acetone for 10 min. Each washing step was followed by a rinsing step, performed with isopropanol. The clean ITOs were finally rinsed and stored in isopropanol. The ultrasonic bath was performed using a sonicator (Elmasonic P®) set at a frequency of 80- 90 kHz and maintained at a temperature of 30 °C-40 °C. The viscous TiO2 paste deposited on the ITOs was prepared by mixing approximately 65 mg of TiO2 powder with 30 µL of 1.1 M nitric acid (HNO3). The obtained paste can produce one anode under the investigated experimental conditions. The following steps were taken to deposit the semiconductor on the ITOs. ITOs were firmly fixed to a glass slide (2.5 cm x 5 cm) using adhesive tape, with their conductive side facing upwards. The adhesive tape was applied to delineate a square area suitable to host the TiO2 paste. At this stage, the paste was first used at the bottom of the ITOs and then evenly spread over the entire surface of the smaller square by a rolling motion of a glass pipette. The resulting anode was left to dry for 15 min and then placed on a heating plate set at 70°C for additional 15 min. The tape was then removed to obtain the anode for the DSSC. The Ag@Au NPs were deposited on the TiO_2-coated anodes (TiO2-anodes) through eLbL deposition following the protocol reported in ref [93]. Following these steps, the TiO_2-anodes underwent pre-treatment using a Zepto plasma cleaner purchased from Diener Electronic® for plasma cleaning. The PE multilayer (PEM) with the PAH(+)/PSS(-)/PAH(+) sequence was obtained by immersing the substrates for 10 min in 3 mL of PAH, 3 mL of PSS, and 3 mL

of PAH. A washing step of 2 min was performed after each immersion in the PE solutions and at the end of the PEM building process. Afterwards, the PEM-functionalized anodes were carefully dried with the nitrogen stream and stored for 1 h at 4 °C before the fabrication of the Ag@Au NPs array. For this final step, the PEM-functionalized anodes were immersed in an H dispersion for 16 h. The resulting H-functionalized anodes were then gently dried with a nitrogen stream.

***Cathodes preparation*:** The PSSC cathodes comprise ITOs coated with carbon black as a catalytic material. To prepare this component, 1.5 cm x 1.5 cm ITOs were positioned over a lit candle until the conductive side of the glass became entirely darkened. Finally, one side of the glass was cleaned of the carbon particles with a Q-tip to leave a clean surface for the subsequent sealing of the electrodes.

***PSSC cells assembly and electrolyte deposition*:** To seal the cells, four drops of NOA-61 photopolymer glue with microbeads were applied to the corners of the anodes on the TiO_2-coated sides, leaving 10 μm space between the anodes and cathodes for the electrolyte to infiltrate. The cathodes were positioned on top of the anodes, with the darkened side facing the inside of the cell, carefully leaving space for the electrodes to be sealed. The cells were placed into a UV oven for 1 min to cure and bond the adhesive rapidly. Afterwards, two electrodes were sealed on the two opposite sides of the cell using a tin filament and a soldering iron. The electrodes were then secured to the cell utilizing the NOA glue. The cell was then placed in the UV oven again for each electrode. The electrolyte used for the PSSC was a solution composed of potassium iodide (KI) and iodine (I_2) dissolved in glycol. Under the fume hood, the cells were filled by capillary action as the electrolyte solution was deposited on the sides of the cells using a spatula.

5.2.3 Hybrid Nanostructures on FFP2 Face Mask for white light photothermal disinfection

Fabrication of Hybrid Nanostructures: The first step of heterostructure preparation is to change the AgNCs dispersion medium from ethanol to water. To this end, 500 µL of commercial AgNCs, dispersed in ethanol were isolated by centrifugation (5000 rpm, 5 min, 18 °C). The pellet was washed with acetone and finally dispersed in a water volume suitable to obtain an AgNCs dispersion of 0.2 mg mL^{-1}. Next, a defined volume of AuNRs dispersion was pipetted to 400 µL of AgNCs 0.2 mg mL^{-1}. Subsequently, 3 volumes of AuNRs were introduced to get 3 heterostructures with different Au/Ag mass ratios. After that, MilliQ water was introduced to obtain a final volume of 2 mL. The pH was adjusted to 7 by adding a few NaOH 0.1 m and HCl 0.1 m drops. The dispersion was incubated for 2 h at the temperature of 28 °C (in a water bath) under vigorous stirring. Finally, the heterostructures were isolated by centrifugation (5000 rpm, 5 min, 18 °C), washed twice with acetone and water, and, in the end, dispersed in 2 mL of MilliQ water.

Face Mask Functionalization: The FFP2 face mask was cut into 1 cm x 1 cm samples fixed on a 2.5 cm x 2.5 cm glass substrate, taping their underside. To clean and increase the wettability of the hydrophobic surface of the pieces, they were subjected to 1 min of oxygen plasma treatment at 360 mW and almost 0.12 mbar. Two layers of the heterostructure were added by drop casting: the mask surface was homogenously coated twice with 12 colloidal solution drops, 5 µL each, with a drying pause between the two steps and before the characterization to let the solvent evaporate. Remarkably, ≈33 mL of Ag@Au NPs dispersion is required to cover the entire face mask.

White Light Disinfection: The functionalized face mask was analyzed in smaller samples having an area of (0.5 × 0.5) cm^2 to ensure the complete irradiation of the surface by the optical fiber of

the white light source working at 6.33 W cm^{-2}. Due to the heterostructures on the face mask fibers, the PT effect was tested, varying the treatment interval: 0.5, 1, 2, 5, and 10 min. The high-resolution thermal camera recorded the temperature profile during the light irradiation. The data were then collected and analyzed.

Bacterial Culture: A single colony of *E. coli* K12 strain MG1655, a well characterized strain routinely used in the laboratory,[94] was transferred from a freshly streaked plate into 2 mL of the chemically defined minimal medium E,[95] pH 7.0, supplemented with 0.4% glucose as carbon source. Cultures were prepared in duplicate, and growth was allowed to occur aerobically, overnight, at 37 °C, under orbital shaking. On the following day, the stationary phase cultures were centrifuged at 4300 rpm for 10 min at room temperature, and the bacterial pellet was resuspended in an equal volume (2 mL) of sterile saline solution (0.9% NaCl in water). The optical density at 600 nm (OD600) was read by diluting 100 µL into 900 µL of saline (dilution 1:10). The spectrophotometer used was an Agilent HP8453 UV–Vis diode array spectrophotometer. The approximate CFU mL^{-1} was calculated using the following conversion ratio: 1.0 OD600 = 5×10^8 CFU mL^{-1}. Based on the OD600, the CFU mL−1 of the resuspended bacteria was calculated to be between 8.0×10^8 and 1.1×10^9, depending on the experiment. The exact CFU mL^{-1} was then checked by plating dilutions of the resuspended bacteria, followed by colony counting after plating on an LB agar plate and incubation on at 37 °C to detect survivors. The same method consisting in plating and counting was also used to assess how many bacteria were retained by the face mask pieces (0.5 × 0.5 cm) activated with Ag@Au NPs and immersed in the saline solution with the resuspended bacteria.

Face Mask Treatment with Bacteria: A 48-multiwell plate was used the experiment. Each piece of face mask was immersed in 200 µL of the resuspended bacteria (at the CFU mL^{-1} indicated

above) and left to "contaminate" the face mask for 10 min. After the incubation, each piece of face mask was transferred to the sterile lid of the plate and allowed to dry for 40–45 min. The "contaminated" pieces of face masks were then subject to the white light PT treatment. After this later treatment, a bacteria recovery was performed by immersing each piece into 300 µL of physiological solution (again in a 48-multiwell plate) and leaving the plate for 20 min under shaking at room temperature.

Plating Out and Counting: Depending on the exposure time to the white light PT treatment, a 10 µL aliquot was used for plating out of the bacteria recovered from the "contaminated+treated" masks. The plating on LB agar plates was at 1:100 dilution for mask pieces without exposure, 1:10 dilution for the pieces exposed for 0.5 min, and no dilution for the pieces exposed for 1 min. The bacteria recovered after the exposure to the white light PT treatment for 2, 5, and 10 min were plated out after centrifuging at 6000 rpm for 10 min the 250 µL of saline solution used for recovering the bacteria; after discarding most of the supernatant, 20–30 µL were left and used to resuspend the pellet and do the plating. After overnight incubation at 37 °C, colony counting was performed, and the total CFU (in 300 µL) calculated was registered. Throughout the experiment, a negative control, i.e., mask not contaminated and not exposed, was used to check that no contamination occurred during the handling.

Cell Cultures: The spontaneously transformed aneuploid immortal keratinocyte HaCaT cell line was purchased from Cell Line Service GmBH and was cultured in Dulbecco's Modified Essential Medium (DMEM, Corning, New York, USA), 4.5 g L^{-1} glucose at 37 °C and 5.0% CO_2.

RNA Isolation and Real Time RT-PCR on Cells and EVs: HaCaT cells were seeded into a 6-well plate (2.5 × 105 cells per well, Corning/Falcon, Glendale, AZ, USA). After 24 h, cells were

washed with phosphate Buffer Saline (PBS), the medium was replaced, and cultures were stimulated with v:v dilution of Ag@Au NPs for an additional 24 h or left untreated. At the end of incubation, cells were washed twice with ice-cold PBS, and total RNA was extracted using the Total RNA Purification Kit (Norgen Biotek Corp., Ontario, Canada). 1 μg of total RNA was retro-transcribed using the Tetro cDNA synthesis kit (Meridian BioScience, Cincinnati, Ohio, USA), and cDNA products were analyzed by Real-Time RT-PCR using the SensiMix SYBR Hi-ROX Kit (Meridian Bioscience, Cincinnati, OH, USA). Data were normalized using HPRT-1 as endogenous control and expressed using the 2−ΔΔCT method using the untreated cells as reference.[96] Three independent experiments were performed in triplicate.

Cytometric Cytotoxic Assay: HaCaT cells were seeded into a 6-well plate (2.5 × 105 cells per well, Corning/Falcon, Glendale, AZ, USA). After 24 h, cells were washed with phosphate Buffer Saline (PBS), the medium was replaced, and cultures were incubated with Ag@Au NPs for 24 h or 48 h with 1:50 to 1:6250 v:v dilutions of irradiated NPs or left untreated. At the end of incubation, cells were washed twice with PBS, trypsinized, collected by centrifugation at 500xG, 5 min, RT, and resuspended in 500 μL of PBS. Propidium Iodide (1:100 dilution of a 1 mg mL−1 ready-to-use solution; Merck, Darmstadt, Germany) was added, and each sample was acquired on a FACsARIA II instrument using FACs DiVa software (v.6.1.1, both by Becton Dickinson, NJ, USA). Positive control was obtained by undergoing cells to repeated freeze-thaw cycles. At least 20.000 events were recorded and analyzed for every sample using Flowing software (v2.5.1, Turku Centre for Biotechnology, Turku, Finland).

5.2.4 Optical Metasurface for Pathogens Detection:

Metasurface Fabrication: The protocol used for constructing the metasurfaces is the one reported in ref. [19]. The glass slides having a 50 nm thick Au layer on the top were washed with water and dried

under nitrogen flow before their immersion in polyelectrolyte solutions having positive (PAH, 1.6 mg mL^{-1} in NaCl 0.5 m) and negative (PSS, 1.6 mg mL^{-1} in NaCl 0.5 m) charges alternatively for 5 min creating the PE multilayer composed by the sequence PAH/PSS/PAH/PSS/PAH that works as the dielectric spacer between the reflective Au surface and the AgNCs that is immobilized on its surface. Immersions in NaCl 0.5 M for 1 min are required among these steps. Finally, 5.6 mg mL^{-1} of AgNCs 0.9 mg mL^{-1} were drop cast on the PE multilayer. After 24 h incubation at 4 °C under the weight of a glass slide, this one was removed, rinsed with water, and dried under nitrogen flow.

Metasurface Bio-Activation and E. Coli Detection: The metasurface samples were bioactivated by immersing them in anti-*E. coli* antibody 1011 for 2 h. Then, they were washed, rinsed with water, and dried under nitrogen flow. Once the samples were characterized, they were tested using *E. coli* dispersions at different concentrations: from 10^{-1} CFU mL^{-1} to 10^{3} CFU mL^{-1}. To mimic the environmental biosensing experiments, an aerosolized liquid suspension of E. coli cells was directly sprayed for 10 min onto the metasurface biosensor at a constant flow rate of 13 L min^{-1} at a distance of 30 cm. The samples were characterized after drying them under nitrogen flow.

5.3 Characterization

UV-Visible optical spectrophotometry: A Lambda 365 spectrophotometer from PerkinElmer was employed to collect the absorption spectra of the AuNR modified substrates, the double-face AuNRs cell and of the colloidal dispersions and the diffuse reflection spectra of the functionalized face masks and of the PSSCs with the addition of the integrating sphere. A diode array spectrophotometer HP8453 (Agilent Technologies) was used for the OD600 measurement of the *E. coli* cultures. A customized reflective optical setup made of a USB spectrophotometer (USB 2000+XR1, Ocean Optics, FL, USA) equipped with a UV-visible

light source (CLS 100; Leica, Vienna, Austria) was used to acquire the reflectance spectra of the metasurface samples that were placed on a holder and controlled with x-y-z translation stages for the proper alignment.

Dynamic Light Scattering (DLS) Characterization: Size and zeta-potential experiments were conducted with a Malvern NanoZetaSizer spectrometer (Malvern, Herrenberg, Germany) equipped with a digital logarithmic correlator and a 5 mW He–Ne laser (= 632.8 nm). The Stokes-Einstein equation was used to estimate the nano composites' hydrodynamic radius (RH). The Smoluchowski equation calculated zeta potential. Malvern micro cuvettes (ZEN0040) were used for size measurements, while zeta potential measurements were obtained using a Dip Cell Kit (ZEN1002). Size measurements were performed on Ag@Au NP dispersions diluted with distilled water and phosphate saline buffer (PBS) at different dilution factors (i.e., 1:3, 1:5, and 1:10 vol/vol). Samples were exclusively diluted in distilled water for zeta potential experiments to ensure reliable and accurate measurements. Each experiment was performed at a fixed temperature (25 °C) with an automatic attenuator. For each sample, three independent measurements were averaged.

Raman scattering measurements: They were recorded at room temperature using a micro-Raman dispersive spectrometer (SENTERRA, Bruker Optics) equipped with a CW diode pumped solid state laser ($\lambda 0 = 532$ nm) and a 20x objective (Olympus B41). The spectra were recorded using a laser power of 5 mW, 10 coadditions, and an integration time of 1sec within the range from 50 to 2000 cm^{-1}.

Transmission Electron Microscopy: TEM was used to study the morphology of the colloidal NP (AuNRs and AgNCs) dispersions and the Ag@Au NPs heterostructure. The analysis was carried out using a JEM 1400-Plus JEOL microscope operating at an

acceleration voltage of 120 kV equipped with a LAB6 filament. A few drops of the composite suspension were coated onto copper grids with an amorphous carbon film layer and dried under air to allow solvent evaporation.

Scanning electron microscopy: The measurements to study the morphology of AuNR substrates were obtained by a field emission SEM (FE-SEM, Carl Zeiss, SUPRA 40VP) with an accelerating voltage of 2 kV. SEM micrographs of the anodes' surface morphology were obtained using a high-resolution electron microscope (AURIGA from Zeiss). Measurements were performed at the interdepartmental research center on nanotechnologies applied to engineering (C.N.I.S.— Sapienza University of Rome). Morphological analyses of the functionalized FFP2 face mask were conducted using a SEM (FE- SEM Mira3 by Tescan) equipped with an Octane Elect EDS System by EDAX-AMETEK Inc. Before the investigation, the samples were sputter coated with 20 nm chromium.

Atomic force microscopy: The topography of the AuNR substrates was analyzed by atomic force microscopy (AFM, Nanoscope Multimode system, Veeco Instruments). The measurements were performed in tapping mode with a vertical resolution of 0.1 Å and lateral resolution of 2 Å.

White light photothermal measurements: A broadband light source with an operating wavelength range from 400 to 1000 nm was used for the photothermal characterization. The power density was tunable and an optical fiber was used to irradiate the whole sample area uniformly. A high resolution thermal camera (FLIR, A655sc) was used to record the temperature variation during the irradiation and map the heating distribution. The thermal images are 640 x 480 pixels and have an accuracy of ±0.20 °C. The software FLIR ResearchIR Max was used to acquire and process data from the thermal camera.

Photoelectric characterization: It was performed using the Tektronix 3 Series MDO Mixed Domain Oscilloscope and an OSL2IR High-intensity fiber light source with 150 W, 3200 K halogen bulbs from Thorlabs. The photoelectric measurements exhibited high repeatability, with a standard deviation of less than 4%, confirming the robustness and stability of our measurements. This property highlights the high reproducibility of the DSSCs and PSSCs.

Contrast phase and fluorescence microscopy: A ZEISS Axiolab 5 fluorescent microscope, equipped with contrast phase objectives and fluorescence modules, was used to collect micrographs of the bioactive AuNR substrates.

Statistical Analysis: OriginLab software was used for data management and statistical analysis of the UV–visible absorption and diffusive reflection spectra. This software also facilitated the statistical analysis of the photothermal data. The efficacy of the statistical fits was assessed by determining the R2 coefficient. ResearchIR software is used to collect and analyze thermal camera recordings. The experiments involving the microbial solutions or the PV cells were performed for at least three replications; OriginLab software was used to analyze the data. Real-time RT-PCR data were normalized using HPRT-1 as endogenous control and expressed using the $2^{-\Delta\Delta CT}$ method using the untreated cells as reference. In the cytometric cytotoxic essay, at least 20.000 events were recorded and analyzed for every sample using Flowing software. Three independent experiments were performed in triplicate. One-way ANOVA test was used to analyze data with Dunnett's multiple comparison test; a p-value < 0.05 (**) was considered statistically significant. GraphPad Prism and OriginLab software were used to analyze the data.

6. Appendices

6.1 Photothermal efficiency

Under low continuous radiation conditions, the temperature difference between the NPs and their surrounding medium can be considered as negligible. As a result, we can assume they have the same temperature. Under the current experimental conditions, the photothermal conversion efficiency can be calculated as [97]

$$\eta = \frac{(c_{sm}m_{sm} + c_{NP}m_{NP})\,\Delta T}{IA\Delta t} \approx \frac{c_{sm}m_{sm}}{IA}\frac{\Delta T}{\Delta t}, \quad (1)$$

where c_{sm} and c_{NP} are the specific heat of the surrounding medium and NPs respectively; m_{sm} and m_{NP} are the mass of the surrounding medium and NPs respectively; ΔT is the temperature rise in the Δt time interval and A is the irradiated area at a proper light source power density I of the sample in the experiment. As the employed NPs concentration is small, we can simplify the equation of the photothermal conversion efficiency as shown. The efficiency can be calculated in conditions of negligible heat leak, namely the first seconds of the initial temperature rise gradient.

For the calculus of the photothermal conversion efficiency of Au NR substrates, we considered glass as surrounding medium of the MNPs. Indeed, we assumed the specific heat capacity of the borosilicate glass of 779.7 J kg^{-1} $°C^{-1}$ and the 1 cm x 1 cm substrate mass of 0.212 g irradiated under a white light source at 14.7 W cm^{-2} giving an average wavelength of 600 nm.

The same equation was also used to determine the photothermal efficiency of nanofluids such as the Ag@Au NPs dispersion. We considered water as surrounding medium with a specific heat capacity of 4.186 J g^{-1} $°C^{-1}$. The hybrid heterostructures (colloidal dispersion volume of 1 mL) were irradiated for 10 min under different CW laser sources working at 405 nm, 532 nm and 808 nm with the corresponding power densities of 903 mW cm^{-2}, 905 mW cm^{-2} and 897 mW cm^{-2}, and also under the combination of the three lasers together with an average power density of ~901.7 mW

cm^{-2}. The temperature variation was considered along the first 5 min of irradiation where the heat leak is negligible. However, the Ag@Au NPs photothermal efficiency calculated for white light irradiation is lower. It is ascribable to the higher values of light intensity (7.09 W cm^{-2}), to the broader optical fiber output (0.74 cm of diameter) and, primarly, for the considerable heating of the bare water (~56 °C). This issue was solved with a material having a lower thermal conductivity such the PP fibers of the FFP2 face mask.
The photothermal efficiency of the functionalized FFP2 face mask was calculated considering the lower specific heat capacity of the PP fibers (1700 J Kg^{-1} K^{-1}) compared to water, thus facilitating the temperature increase of the functionalized fibers and preventing the heating of the bare face mask. We assumed the white light power density of 6.33 W cm^{-2}, the sample mass of 0.5 g and an irradiated area of 1 cm^2. The rising temperature was calculated during the initial 60 sec of irradiation avoiding the heat leak contribution.

6.2 Photoelectric efficiency

The photoelectric efficiency of a PV cell can be calculated as the ratio between the maximum generated power and the electrical input power from the light source as the following equation:

$$\eta = \frac{P_{out}}{P_{in}} = \frac{V_{out}J_{out}}{P_{in}} = \frac{V_{out}I_{out}}{P_{in}A} = \frac{V_{out}^2}{P_{in}RA}, \quad (2)$$

where V_{out} and J_{out} are the output voltage and the current density produced by the cell. J_{out} is expressed in Amperes per unit area but can rewritten as the output current I divided by the active area of the cell A defined as a square with side length of l=0.8 cm and area A=0.64 cm^2. The resistances of the investigated cells were calculated with the use of a multimeter: R_{DSSC}=100 kΩ and R_{PSSC}=69.4 kΩ.

The calculus of the photoelectric efficiency under natural solar light also required the measurement of the sunlight intensity of 40 mW cm^{-2}. Moreover, an average output voltage of 0.45 V ± 0.03 V and a current of 25 μA are considered.

7. References

(1) Bhowmick, T. K.; Gayen, K.; Maity, S. K. *Nanobiotechnology: Applications of Nanomaterials in Biotechnology, Medicine and Healthcare*, 1st ed.; CRC Press: Boca Raton, 2024. https://doi.org/10.1201/9781003305583.
(2) Wang, L.; Hasanzadeh Kafshgari, M.; Meunier, M. Optical Properties and Applications of Plasmonic-Metal Nanoparticles. *Adv. Funct. Mater.* **2020**, *30* (51), 2005400. https://doi.org/10.1002/adfm.202005400.
(3) Ma, X.; Tian, Y.; Yang, R.; Wang, H.; Allahou, L. W.; Chang, J.; Williams, G.; Knowles, J. C.; Poma, A. Nanotechnology in Healthcare, and Its Safety and Environmental Risks. *J. Nanobiotechnology* **2024**, *22* (1), 715. https://doi.org/10.1186/s12951-024-02901-x.
(4) Yang, B.; Li, C.; Wang, Z.; Dai, Q. Thermoplasmonics in Solar Energy Conversion: Materials, Nanostructured Designs, and Applications. *Adv. Mater.* **2022**, *34* (26), 2107351. https://doi.org/10.1002/adma.202107351.
(5) Hutter, E.; Fendler, J. H. Exploitation of Localized Surface Plasmon Resonance. *Adv. Mater.* **2004**, *16* (19), 1685–1706. https://doi.org/10.1002/adma.200400271.
(6) Freestone, I.; Meeks, N.; Sax, M.; Higgitt, C. The Lycurgus Cup — A Roman Nanotechnology. *Gold Bull.* **2007**, *40* (4), 270–277. https://doi.org/10.1007/BF03215599.
(7) Azharuddin, M.; Zhu, G. H.; Das, D.; Ozgur, E.; Uzun, L.; Turner, A. P. F.; Patra, H. K. A Repertoire of Biomedical Applications of Noble Metal Nanoparticles. *Chem. Commun.* **2019**, *55* (49), 6964–6996. https://doi.org/10.1039/C9CC01741K.
(8) Nejati, K.; Dadashpour, M.; Gharibi, T.; Mellatyar, H.; Akbarzadeh, A. Biomedical Applications of Functionalized Gold Nanoparticles: A Review. *J. Clust. Sci.* **2022**, *33* (1), 1–16. https://doi.org/10.1007/s10876-020-01955-9.
(9) Sheikh, M.; Shekarchizadeh, H. Recent Advances in Localized Surface Plasmon Resonance (LSPR)-Based Colorimetric and

Fluorescent Nanosensors for the Detection of Organophosphorus Pesticides. *J. Food Compos. Anal.* **2025**, *144*, 107653. https://doi.org/10.1016/j.jfca.2025.107653.

(10) *Active Plasmonic Nanomaterials*, 0 ed.; De Sio, L., Ed.; Jenny Stanford Publishing, 2015. https://doi.org/10.1201/b18647.

(11) Dement'eva, O. V.; Kartseva, M. E. Noble Metal Nanoparticles in Biomedical Thermoplasmonics. *Colloid J.* **2023**, *85* (4), 500–519. https://doi.org/10.1134/S1061933X23700187.

(12) Kim, M.; Lee, J.; Nam, J. Plasmonic Photothermal Nanoparticles for Biomedical Applications. *Adv. Sci.* **2019**, *6* (17), 1900471. https://doi.org/10.1002/advs.201900471.

(13) Hang, Y.; Wang, A.; Wu, N. Plasmonic Silver and Gold Nanoparticles: Shape- and Structure-Modulated Plasmonic Functionality for Point-of-Caring Sensing, Bio-Imaging and Medical Therapy. *Chem. Soc. Rev.* **2024**, *53* (6), 2932–2971. https://doi.org/10.1039/D3CS00793F.

(14) Pearce, M. E.; Melanko, J. B.; Salem, A. K. Multifunctional Nanorods for Biomedical Applications. *Pharm. Res.* **2007**, *24* (12), 2335–2352. https://doi.org/10.1007/s11095-007-9380-7.

(15) Stone, J.; Jackson, S.; Wright, D. Biological Applications of Gold Nanorods. *WIREs Nanomedicine Nanobiotechnology* **2011**, *3* (1), 100–109. https://doi.org/10.1002/wnan.120.

(16) Zhang, L.; Wang, J.; Zhang, J.; Liu, Y.; Wu, L.; Shen, J.; Zhang, Y.; Hu, Y.; Fan, Q.; Huang, W.; Wang, L. Individual Au-Nanocube Based Plasmonic Nanoprobe for Cancer Relevant MicroRNA Biomarker Detection. *ACS Sens.* **2017**, *2* (10), 1435–1440. https://doi.org/10.1021/acssensors.7b00322.

(17) Hang, Y.; Wang, A.; Wu, N. Plasmonic Silver and Gold Nanoparticles: Shape- and Structure-Modulated Plasmonic Functionality for Point-of-Caring Sensing, Bio-Imaging and Medical Therapy. *Chem. Soc. Rev.* **2024**, *53* (6), 2932–2971. https://doi.org/10.1039/D3CS00793F.

(18) Petronella, F.; Zaccagnini, F.; Sforza, M. L.; De Mei, V.; De Sio, L. Bottom–Up Metasurfaces for Biotechnological Applications. *Adv. Sci.* **2025**, *12* (9), 2413679. https://doi.org/10.1002/advs.202413679.
(19) Petronella, F.; Madeleine, T.; De Mei, V.; Zaccagnini, F.; Striccoli, M.; D'Alessandro, G.; Rumi, M.; Slagle, J.; Kaczmarek, M.; De Sio, L. Thermoplasmonic Controlled Optical Absorber Based on a Liquid Crystal Metasurface. *ACS Appl. Mater. Interfaces* **2023**, *15* (42), 49468–49477. https://doi.org/10.1021/acsami.3c09896.
(20) Mohapatra, S. Sterilization and Disinfection. In *Essentials of Neuroanesthesia*; Elsevier, 2017; pp 929–944. https://doi.org/10.1016/B978-0-12-805299-0.00059-2.
(21) Bäumler, W.; Eckl, D.; Holzmann, T.; Schneider-Brachert, W. Antimicrobial Coatings for Environmental Surfaces in Hospitals: A Potential New Pillar for Prevention Strategies in Hygiene. *Crit. Rev. Microbiol.* **2022**, *48* (5), 531–564. https://doi.org/10.1080/1040841X.2021.1991271.
(22) Verma, D. K.; Sharma, A.; Awasthi, L.; Singh, H.; Kumar, P.; Rajput, P.; Sinha, A.; Chaubey, K. K.; Kumar, A.; Rai, N.; Bachheti, R. K. Recent Development and Importance of Nanoparticles in Disinfection and Pathogen Control. In *Nanomaterials for Environmental and Agricultural Sectors*; Bachheti, R. K., Bachheti, A., Husen, A., Eds.; Smart Nanomaterials Technology; Springer Nature Singapore: Singapore, 2023; pp 83–106. https://doi.org/10.1007/978-981-99-2874-3_5.
(23) Vasilyak, L. M. Physical Methods of Disinfection (A Review). *Plasma Phys. Rep.* **2021**, *47* (3), 318–327. https://doi.org/10.1134/S1063780X21030107.
(24) Weber, D. J.; Rutala, W. A.; Anderson, D. J.; Chen, L. F.; Sickbert-Bennett, E. E.; Boyce, J. M. Effectiveness of Ultraviolet Devices and Hydrogen Peroxide Systems for Terminal Room Decontamination: Focus on Clinical Trials.

Am. J. Infect. Control **2016**, *44* (5), e77–e84. https://doi.org/10.1016/j.ajic.2015.11.015.

(25) Giannakis, S.; Le, T.-T. M.; Entenza, J. M.; Pulgarin, C. Solar Photo-Fenton Disinfection of 11 Antibiotic-Resistant Bacteria (ARB) and Elimination of Representative AR Genes. Evidence That Antibiotic Resistance Does Not Imply Resistance to Oxidative Treatment. *Water Res.* **2018**, *143*, 334–345. https://doi.org/10.1016/j.watres.2018.06.062.

(26) De Pasquale, I.; Lo Porto, C.; Dell'Edera, M.; Petronella, F.; Agostiano, A.; Curri, M. L.; Comparelli, R. Photocatalytic TiO2-Based Nanostructured Materials for Microbial Inactivation. *Catalysts* **2020**, *10* (12), 1382. https://doi.org/10.3390/catal10121382.

(27) Birgand, G.; Ahmad, R.; Bulabula, A. N. H.; Singh, S.; Bearman, G.; Sánchez, E. C.; Holmes, A. Innovation for Infection Prevention and Control—Revisiting Pasteur's Vision. *The Lancet* **2022**, *400* (10369), 2250–2260. https://doi.org/10.1016/S0140-6736(22)02459-X.

(28) Santos, G. M.; Ferrara, F. I. D. S.; Zhao, F.; Rodrigues, D. F.; Shih, W.-C. Photothermal Inactivation of Heat-Resistant Bacteria on Nanoporous Gold Disk Arrays. *Opt. Mater. Express* **2016**, *6* (4), 1217. https://doi.org/10.1364/OME.6.001217.

(29) Maity, S.; Downen, L. N.; Bochinski, J. R.; Clarke, L. I. Embedded Metal Nanoparticles as Localized Heat Sources: An Alternative Processing Approach for Complex Polymeric Materials. *Polymer* **2011**, *52* (7), 1674–1685. https://doi.org/10.1016/j.polymer.2011.01.062.

(30) Guan, G.; Win, K. Y.; Yao, X.; Yang, W.; Han, M. Plasmonically Modulated Gold Nanostructures for Photothermal Ablation of Bacteria. *Adv. Healthc. Mater.* **2021**, *10* (3), 2001158. https://doi.org/10.1002/adhm.202001158.

(31) Fang, C.; Shao, L.; Zhao, Y.; Wang, J.; Wu, H. A Gold Nanocrystal/Poly(Dimethylsiloxane) Composite for Plasmonic

Heating on Microfluidic Chips. *Adv. Mater.* **2012**, *24* (1), 94–98. https://doi.org/10.1002/adma.201103517.
(32) Yang, L.; Yan, W.; Wang, H.; Zhuang, H.; Zhang, J. Shell Thickness-Dependent Antibacterial Activity and Biocompatibility of Gold@silver Core–Shell Nanoparticles. *RSC Adv.* **2017**, *7* (19), 11355–11361. https://doi.org/10.1039/C7RA00485K.
(33) World Health Organization. *WHO Guidance for Climate Resilient and Environmentally Sustainable Health Care Facilities*; World Health Organization, 2020.
(34) Badanta, B.; Porcar Sierra, A.; Fernández, S. T.; Rodríguez Muñoz, F. J.; Pérez-Jiménez, J. M.; Gonzalez-Cano-Caballero, M.; Ruiz-Adame, M.; de-Diego-Cordero, R. Advancing Environmental Sustainability in Healthcare: Review on Perspectives from Health Institutions. *Environments* **2025**, *12* (1), 9. https://doi.org/10.3390/environments12010009.
(35) Liang, Z.; Zhang, Y.; Xu, H.; Chen, W.; Liu, B.; Zhang, J.; Zhang, H.; Wang, Z.; Kang, D.-H.; Zeng, J.; Gao, X.; Wang, Q.; Hu, H.; Zhou, H.; Cai, X.; Tian, X.; Reiss, P.; Xu, B.; Kirchartz, T.; Xiao, Z.; Dai, S.; Park, N.-G.; Ye, J.; Pan, X. Homogenizing Out-of-Plane Cation Composition in Perovskite Solar Cells. *Nature* **2023**, *624* (7992), 557–563. https://doi.org/10.1038/s41586-023-06784-0.
(36) Ren, Y.; Zhang, D.; Suo, J.; Cao, Y.; Eickemeyer, F. T.; Vlachopoulos, N.; Zakeeruddin, S. M.; Hagfeldt, A.; Grätzel, M. Hydroxamic Acid Pre-Adsorption Raises the Efficiency of Cosensitized Solar Cells. *Nature* **2023**, *613* (7942), 60–65. https://doi.org/10.1038/s41586-022-05460-z.
(37) Zheng, D.; Prado, Y.; Pauporté, T.; Coolen, L. Deciphering the Effects of Plasmonic Nanoparticles Doping in Hybrid Perovskite Photovoltaic and Photodetector Devices. *Adv. Opt. Mater.* **2025**, *13* (2), 2401964. https://doi.org/10.1002/adom.202401964.
(38) Ishak, N. N.; Mohamed Ali, M. S.; Bsoul, A. Nanostructured Materials for Highly Efficient Dye-Sensitized

Solar Cells: A Review. *Adv. Mater. Technol.* **2025**, *10* (11), 2401519. https://doi.org/10.1002/admt.202401519.

(39) Shi, J.; Li, H.; Xu, F.; Tao, X. Materials in Advanced Design of Personal Protective Equipment: A Review. *Mater. Today Adv.* **2021**, *12*, 100171. https://doi.org/10.1016/j.mtadv.2021.100171.

(40) Tuñón-Molina, A.; Takayama, K.; Redwan, E. M.; Uversky, V. N.; Andrés, J.; Serrano-Aroca, Á. Protective Face Masks: Current Status and Future Trends. *ACS Appl. Mater. Interfaces* **2021**, *13* (48), 56725–56751. https://doi.org/10.1021/acsami.1c12227.

(41) Wang, L.; Li, S.; Ahmad, I. M.; Zhang, G.; Sun, Y.; Wang, Y.; Sun, C.; Jiang, C.; Cui, P.; Li, D. Global Face Mask Pollution: Threats to the Environment and Wildlife, and Potential Solutions. *Sci. Total Environ.* **2023**, *887*, 164055. https://doi.org/10.1016/j.scitotenv.2023.164055.

(42) Pandit, P.; Maity, S.; Singha, K.; Annu; Uzun, M.; Shekh, M.; Ahmed, S. Potential Biodegradable Face Mask to Counter Environmental Impact of Covid-19. *Clean. Eng. Technol.* **2021**, *4*, 100218. https://doi.org/10.1016/j.clet.2021.100218.

(43) Crespo, C.; Ibarz, G.; Sáenz, C.; Gonzalez, P.; Roche, S. Study of Recycling Potential of FFP2 Face Masks and Characterization of the Plastic Mix-Material Obtained. A Way of Reducing Waste in Times of Covid-19. *Waste Biomass Valorization* **2021**, *12* (12), 6423–6432. https://doi.org/10.1007/s12649-021-01476-0.

(44) Wang, D.; Sun, B.-C.; Wang, J.-X.; Zhou, Y.-Y.; Chen, Z.-W.; Fang, Y.; Yue, W.-H.; Liu, S.-M.; Liu, K.-Y.; Zeng, X.-F.; Chu, G.-W.; Chen, J.-F. Can Masks Be Reused After Hot Water Decontamination During the COVID-19 Pandemic? *Engineering* **2020**, *6* (10), 1115–1121. https://doi.org/10.1016/j.eng.2020.05.016.

(45) Liao, L.; Xiao, W.; Zhao, M.; Yu, X.; Wang, H.; Wang, Q.; Chu, S.; Cui, Y. Can N95 Respirators Be Reused after

Disinfection? How Many Times? *ACS Nano* **2020**, *14* (5), 6348–6356. https://doi.org/10.1021/acsnano.0c03597.

(46) Valdez-Salas, B.; Beltran-Partida, E.; Cheng, N.; Salvador-Carlos, J.; Valdez-Salas, E. A.; Curiel-Alvarez, M.; Ibarra-Wiley, R. Promotion of Surgical Masks Antimicrobial Activity by Disinfection and Impregnation with Disinfectant Silver Nanoparticles. *Int. J. Nanomedicine* **2021**, *Volume 16*, 2689–2702. https://doi.org/10.2147/IJN.S301212.

(47) De Sio, L.; Ding, B.; Focsan, M.; Kogermann, K.; Pascoal-Faria, P.; Petronela, F.; Mitchell, G.; Zussman, E.; Pierini, F. Personalized Reusable Face Masks with Smart Nano-Assisted Destruction of Pathogens for COVID-19: A Visionary Road. *Chem. – Eur. J.* **2021**, *27* (20), 6112–6130. https://doi.org/10.1002/chem.202004875.

(48) Haghighat Bayan, M. A.; Rinoldi, C.; Rybak, D.; Zargarian, S. S.; Zakrzewska, A.; Cegielska, O.; Põhako-Palu, K.; Zhang, S.; Stobnicka-Kupiec, A.; Górny, R. L.; Nakielski, P.; Kogermann, K.; De Sio, L.; Ding, B.; Pierini, F. Engineering Surgical Face Masks with Photothermal and Photodynamic Plasmonic Nanostructures for Enhancing Filtration and On-Demand Pathogen Eradication. *Biomater. Sci.* **2024**, *12* (4), 949–963. https://doi.org/10.1039/D3BM01125A.

(49) Rozin, M. J.; Rosen, D. A.; Dill, T. J.; Tao, A. R. Colloidal Metasurfaces Displaying Near-Ideal and Tunable Light Absorbance in the Infrared. *Nat. Commun.* **2015**, *6* (1), 7325. https://doi.org/10.1038/ncomms8325.

(50) Mann, M. E.; Yadav, P.; Kim, S. Colloidal Plasmonic Nanocubes as Capacitor Building Blocks for Multidimensional Optical Metamaterials: A Review. *ACS Appl. Nano Mater.* **2021**, *4* (10), 9976–9984. https://doi.org/10.1021/acsanm.1c02211.

(51) Fajri, M. L.; Kossowski, N.; Bouanane, I.; Bedu, F.; Poungsripong, P.; Juliano-Martins, R.; Majorel, C.; Margeat, O.; Le Rouzo, J.; Genevet, P.; Sciacca, B. Designer Metasurfaces via Nanocube Assembly at the Air–Water

Interface. *ACS Nano* **2024**, acsnano.4c06022. https://doi.org/10.1021/acsnano.4c06022.

(52) Shrivastav, A. M.; Cvelbar, U.; Abdulhalim, I. A Comprehensive Review on Plasmonic-Based Biosensors Used in Viral Diagnostics. *Commun. Biol.* **2021**, *4* (1), 70. https://doi.org/10.1038/s42003-020-01615-8.

(53) Wang, Z.; Chen, W.; Liu, X.; Lin, S.; Deng, B.; Shen, J.; Li, F.; Zhu, J. Plasmonic Metasurface Enhanced by Nanobumps for Label-Free Biosensing of Lung Tumor Markers in Serum. *Talanta* **2023**, *264*, 124731. https://doi.org/10.1016/j.talanta.2023.124731.

(54) Qiu, G.; Yue, Y.; Tang, J.; Zhao, Y.-B.; Wang, J. Total Bioaerosol Detection by a Succinimidyl-Ester-Functionalized Plasmonic Biosensor To Reveal Different Characteristics at Three Locations in Switzerland. *Environ. Sci. Technol.* **2020**, *54* (3), 1353–1362. https://doi.org/10.1021/acs.est.9b05184.

(55) Cheng, P.; Wang, D.; Schaaf, P. A Review on Photothermal Conversion of Solar Energy with Nanomaterials and Nanostructures: From Fundamentals to Applications. *Adv. Sustain. Syst.* **2022**, *6* (9), 2200115. https://doi.org/10.1002/adsu.202200115.

(56) Borah, R.; Verbruggen, S. W. Silver–Gold Bimetallic Alloy versus Core–Shell Nanoparticles: Implications for Plasmonic Enhancement and Photothermal Applications. *J. Phys. Chem. C* **2020**, *124* (22), 12081–12094. https://doi.org/10.1021/acs.jpcc.0c02630.

(57) Karam, T. E.; Smith, H. T.; Haber, L. H. Enhanced Photothermal Effects and Excited-State Dynamics of Plasmonic Size-Controlled Gold–Silver–Gold Core–Shell–Shell Nanoparticles. *J. Phys. Chem. C* **2015**, *119* (32), 18573–18580. https://doi.org/10.1021/acs.jpcc.5b05110.

(58) Hu, B.; Wang, N.; Han, L.; Chen, M.-L.; Wang, J.-H. Core–Shell–Shell Nanorods for Controlled Release of Silver That Can Serve as a Nanoheater for Photothermal Treatment

on Bacteria. *Acta Biomater.* **2015**, *11*, 511–519. https://doi.org/10.1016/j.actbio.2014.09.005.

(59) Liu, W.; Wang, Y.; Wang, Y.; Li, X.; Qi, K.; Wang, J.; Xu, H. Black Silver Nanocubes@Amino Acid-Encoded Highly Branched Gold Shells with Efficient Photothermal Conversion for Tumor Therapy. *ACS Appl. Mater. Interfaces* **2023**, *15* (1), 236–248. https://doi.org/10.1021/acsami.2c14436.

(60) Yang, X.; Liang, J.; Fu, H.; Ran, X.; An, X. Fabrication of Au-Ag@TiO2 Ternary Core-Shell Nanostructures with Enhanced Sunlight Photocatalytic Activity. *Powder Technol.* **2022**, *404*, 117463. https://doi.org/10.1016/j.powtec.2022.117463.

(61) Zaccagnini, F.; Radomski, P.; Sforza, M. L.; Ziółkowski, P.; Lim, S.-I.; Jeong, K.-U.; Mikielewicz, D.; Godman, N. P.; Evans, D. R.; Slagle, J. E.; McConney, M. E.; De Biase, D.; Petronella, F.; De Sio, L. White Light Thermoplasmonic Activated Gold Nanorod Arrays Enable the Photo-Thermal Disinfection of Medical Tools from Bacterial Contamination. *J. Mater. Chem. B* **2023**, *11* (29), 6823–6836. https://doi.org/10.1039/D3TB00865G.

(62) Zaccagnini, F.; De Biase, D.; Bovieri, F.; Perotto, G.; Quagliarini, E.; Bavasso, I.; Mangino, G.; Iuliano, M.; Calogero, A.; Romeo, G.; Singh, D. P.; Pierini, F.; Caracciolo, G.; Petronella, F.; De Sio, L. Multifunctional FFP2 Face Mask for White Light Disinfection and Pathogens Detection Using Hybrid Nanostructures and Optical Metasurfaces. *Small* **2024**, 2400531. https://doi.org/10.1002/smll.202400531.

(63) Jia, Z.; Li, J.; Gao, L.; Yang, D.; Kanaev, A. Dynamic Light Scattering: A Powerful Tool for In Situ Nanoparticle Sizing. *Colloids Interfaces* **2023**, *7* (1), 15. https://doi.org/10.3390/colloids7010015.

(64) Novo, C.; Mulvaney, P. Charge-Induced Rayleigh Instabilities In Small Gold Rods. *Nano Lett.* **2007**, *7* (2), 520–524. https://doi.org/10.1021/nl062649t.

(65) Lee, A.; Ahmed, A.; Dos Santos, D. P.; Coombs, N.; Park, J. I.; Gordon, R.; Brolo, A. G.; Kumacheva, E. Side-by-Side Assembly of Gold Nanorods Reduces Ensemble-Averaged SERS Intensity. *J. Phys. Chem. C* **2012**, *116* (9), 5538–5545. https://doi.org/10.1021/jp3010597.

(66) Perfilieva, O. A.; Pyshnyi, D. V.; Lomzov, A. A. Molecular Dynamics Simulation of Polarizable Gold Nanoparticles Interacting with Sodium Citrate. *J. Chem. Theory Comput.* **2019**, *15* (2), 1278–1292. https://doi.org/10.1021/acs.jctc.8b00362.

(67) Sharma, K.; Sharma, V.; Sharma, S. S. Dye-Sensitized Solar Cells: Fundamentals and Current Status. *Nanoscale Res. Lett.* **2018**, *13* (1), 381. https://doi.org/10.1186/s11671-018-2760-6.

(68) Makuła, P.; Pacia, M.; Macyk, W. How To Correctly Determine the Band Gap Energy of Modified Semiconductor Photocatalysts Based on UV–Vis Spectra. *J. Phys. Chem. Lett.* **2018**, *9* (23), 6814–6817. https://doi.org/10.1021/acs.jpclett.8b02892.

(69) Möls, K.; Aarik, L.; Mändar, H.; Kasikov, A.; Niilisk, A.; Rammula, R.; Aarik, J. Influence of Phase Composition on Optical Properties of TiO2: Dependence of Refractive Index and Band Gap on Formation of TiO2-II Phase in Thin Films. *Opt. Mater.* **2019**, *96*, 109335. https://doi.org/10.1016/j.optmat.2019.109335.

(70) Bottomley, A.; Ianoul, A. Reflection and Absorption Spectra of Silver Nanocubes on a Dielectric Substrate: Anisotropy, Angle, and Polarization Dependencies. *J. Phys. Chem. C* **2014**, *118* (47), 27509–27515. https://doi.org/10.1021/jp508629d.

(71) Movsesyan, A.; Muravitskaya, A.; Castilla, M.; Kostcheev, S.; Proust, J.; Plain, J.; Baudrion, A.-L.; Vincent, R.; Adam, P.-M. Hybridization and Dehybridization of Plasmonic Modes. *J. Phys. Chem. C* **2021**, *125* (1), 724–731. https://doi.org/10.1021/acs.jpcc.0c08570.

(72) Yan, J.; Wu, G.; Guan, N.; Li, L.; Li, Z.; Cao, X. Understanding the Effect of Surface/Bulk Defects on the Photocatalytic Activity of TiO2: Anatase versus Rutile. *Phys. Chem. Chem. Phys.* **2013**, *15* (26), 10978. https://doi.org/10.1039/c3cp50927c.
(73) Taudul, B.; Tielens, F.; Calatayud, M. On the Origin of Raman Activity in Anatase TiO2 (Nano)Materials: An Ab Initio Investigation of Surface and Size Effects. *Nanomaterials* **2023**, *13* (12), 1856. https://doi.org/10.3390/nano13121856.
(74) Sekiya, T.; Ohta, S.; Kamei, S.; Hanakawa, M.; Kurita, S. Raman Spectroscopy and Phase Transition of Anatase TiO2 under High Pressure. *J. Phys. Chem. Solids* **2001**, *62* (4), 717–721. https://doi.org/10.1016/S0022-3697(00)00229-8.
(75) Mayer, M.; Schnepf, M. J.; König, T. A. F.; Fery, A. Colloidal Self-Assembly Concepts for Plasmonic Metasurfaces. *Adv. Opt. Mater.* **2019**, *7* (1), 1800564. https://doi.org/10.1002/adom.201800564.
(76) Richardson, J. J.; Cui, J.; Björnmalm, M.; Braunger, J. A.; Ejima, H.; Caruso, F. Innovation in Layer-by-Layer Assembly. *Chem. Rev.* **2016**, *116* (23), 14828–14867. https://doi.org/10.1021/acs.chemrev.6b00627.
(77) Zaccagnini, F.; Petronella, F.; McConney, M. E.; Slagle, J.; Jeong, K.; Bunning, T. J.; De Sio, L. Thermoplasmonic-Controlled Optical Filters Based on the Combination of Chiral Liquid Crystals and Metasurfaces. *Macromol. Rapid Commun.* **2025**, e00339. https://doi.org/10.1002/marc.202500339.
(78) Petronella, F.; De Biase, D.; Zaccagnini, F.; Verrina, V.; Lim, S.-I.; Jeong, K.-U.; Miglietta, S.; Petrozza, V.; Scognamiglio, V.; Godman, N. P.; Evans, D. R.; McConney, M.; De Sio, L. Label-Free and Reusable Antibody-Functionalized Gold Nanorod Arrays for the Rapid Detection of *Escherichia Coli* Cells in a Water Dispersion. *Environ. Sci. Nano* **2022**, *9* (9), 3343–3360. https://doi.org/10.1039/D2EN00564F.

(79) Huang, X.; El-Sayed, M. A. Gold Nanoparticles: Optical Properties and Implementations in Cancer Diagnosis and Photothermal Therapy. *J. Adv. Res.* **2010**, *1* (1), 13–28. https://doi.org/10.1016/j.jare.2010.02.002.

(80) Farajollahi, A. Nanotechnology in Solar Energy: From Active Systems to Advanced Solar Cells. *Front. Energy Res.* **2025**, *13*, 1560718. https://doi.org/10.3389/fenrg.2025.1560718.

(81) De Sio, L.; Placido, T.; Comparelli, R.; Lucia Curri, M.; Striccoli, M.; Tabiryan, N.; Bunning, T. J. Next-Generation Thermo-Plasmonic Technologies and Plasmonic Nanoparticles in Optoelectronics. *Prog. Quantum Electron.* **2015**, *41*, 23–70. https://doi.org/10.1016/j.pquantelec.2015.03.001.

(82) Cui, Y.; Zhu, Q. Study of Photovoltaic/Thermal Systems with MgO-Water Nanofluids Flowing over Silicon Solar Cells. In *2012 Asia-Pacific Power and Energy Engineering Conference*; IEEE: Shanghai, China, 2012; pp 1–4. https://doi.org/10.1109/APPEEC.2012.6307203.

(83) Alvarenga, M. O. P.; Veloso, S. R. M.; Bezerra, A. L. C. A.; Trindade, B. P.; Gomes, A. S. L.; Monteiro, G. Q. D. M. COVID-19 Outbreak: Should Dental and Medical Practices Consider Uv-c Technology to Enhance Disinfection on Surfaces? – A Systematic Review. *J. Photochem. Photobiol.* **2022**, *9*, 100096. https://doi.org/10.1016/j.jpap.2021.100096.

(84) Dai, T.; Vrahas, M. S.; Murray, C. K.; Hamblin, M. R. Ultraviolet C Irradiation: An Alternative Antimicrobial Approach to Localized Infections? *Expert Rev. Anti Infect. Ther.* **2012**, *10* (2), 185–195. https://doi.org/10.1586/eri.11.166.

(85) California Air Resources Board. *Air Cleaners & Ozone Generating Products*, accessed 8 June 2023.; Vol. Hazardous Ozone-Generating Air Purifiers.

(86) Annesi, F.; Pane, A.; Losso, M. A.; Guglielmelli, A.; Lucente, F.; Petronella, F.; Placido, T.; Comparelli, R.; Guzzo, M. G.; Curri, M. L.; Bartolino, R.; De Sio, L. Thermo-

Plasmonic Killing of Escherichia Coli TG1 Bacteria. *Materials* **2019**, *12* (9), 1530. https://doi.org/10.3390/ma12091530.

(87) Su, Y.-H.; Ke, Y.-F.; Cai, S.-L.; Yao, Q.-Y. Surface Plasmon Resonance of Layer-by-Layer Gold Nanoparticles Induced Photoelectric Current in Environmentally-Friendly Plasmon-Sensitized Solar Cell. *Light Sci. Appl.* **2012**, *1* (6), e14–e14. https://doi.org/10.1038/lsa.2012.14.

(88) Jaffe, P.; Nugent, T.; Strassner Ii, B.; Szazynski, M. *Power Beaming: History, Theory, and Practice*; World Scientific Series on Emerging Technologies; WORLD SCIENTIFIC, 2024; Vol. 05. https://doi.org/10.1142/12438.

(89) Mandolfino, C. Polypropylene Surface Modification by Low Pressure Plasma to Increase Adhesive Bonding: Effect of Process Parameters. *Surf. Coat. Technol.* **2019**, *366*, 331–337. https://doi.org/10.1016/j.surfcoat.2019.03.047.

(90) Rowan, N. J.; MacGregor, S. J.; Anderson, J. G.; Fouracre, R. A.; McIlvaney, L.; Farish, O. Pulsed-Light Inactivation of Food-Related Microorganisms. *Appl. Environ. Microbiol.* **1999**, *65* (3), 1312–1315. https://doi.org/10.1128/AEM.65.3.1312-1315.1999.

(91) Zhang, S.; Wong, C. L.; Zeng, S.; Bi, R.; Tai, K.; Dholakia, K.; Olivo, M. Metasurfaces for Biomedical Applications: Imaging and Sensing from a Nanophotonics Perspective. *Nanophotonics* **2020**, *10* (1), 259–293. https://doi.org/10.1515/nanoph-2020-0373.

(92) Wang, Z.; Chen, J.; Khan, S. A.; Li, F.; Shen, J.; Duan, Q.; Liu, X.; Zhu, J. Plasmonic Metasurfaces for Medical Diagnosis Applications: A Review. *Sensors* **2021**, *22* (1), 133. https://doi.org/10.3390/s22010133.

(93) Sforza, M. L.; Petronella, F.; De Biase, D.; Zaccagnini, F.; Lim, S.; Butt, U. A.; d'Alessandro, A.; Godman, N. P.; Evans, D. R.; McConney, M.; Jeong, K.; De Sio, L. Cascade Structured Plasmonic Liquid Crystal Biosensor for the Rapid Detection of Harmful Bacteria Dispersed in Potable Water.

Adv. Sens. Res. **2024**, *3* (8), 2300201. https://doi.org/10.1002/adsr.202300201.

(94) Pennacchietti, E.; D'Alonzo, C.; Freddi, L.; Occhialini, A.; De Biase, D. The Glutaminase-Dependent Acid Resistance System: Qualitative and Quantitative Assays and Analysis of Its Distribution in Enteric Bacteria. *Front. Microbiol.* **2018**, *9*, 2869. https://doi.org/10.3389/fmicb.2018.02869.

(95) Vogel, H. J.; Bonner, D. M. ACETYLORNITHINASE OF ESCHERICHIA COLI: PARTIAL PURIFICATION AND SOME PROPERTIES. *J. Biol. Chem.* **1956**, *218* (1), 97–106. https://doi.org/10.1016/S0021-9258(18)65874-0.

(96) Livak, K. J.; Schmittgen, T. D. Analysis of Relative Gene Expression Data Using Real-Time Quantitative PCR and the 2−ΔΔCT Method. *Methods* **2001**, *25* (4), 402–408. https://doi.org/10.1006/meth.2001.1262.

(97) Zhang, H.; Chen, H.-J.; Du, X.; Wen, D. Photothermal Conversion Characteristics of Gold Nanoparticle Dispersions. *Sol. Energy* **2014**, *100*, 141–147. https://doi.org/10.1016/j.solener.2013.12.004.

8. List of Publications

F. Zaccagnini, F. Petronella, M. E. McConney, J. Slagle, K.-U. Jeong, T. J. Bunning, L. De Sio, Thermoplasmonic-Controlled Optical Filters Based on the Combination of Chiral Liquid Crystals and Metasurfaces. *Macromol. Rapid Commun.* (IF=4.3) 2025, e00339, with **front cover**.

F. Petronella, F. Zaccagnini, V. De Mei, & L. De Sio. (2025). Liquid crystal metasurfaces. *Liquid Crystals Reviews* (IF=4.2), 13(2), 83–101.

A. Koulali, P. Ziółkowski, P. Radomski, F. Petronella, F. Zaccagnini, W. Szczecińska, D. De Biase, U. A. Butt, J. Zieliński, L. De Sio & D. Mikielewicz et al. (2025). Enhancing Bacteria Inactivation: Computational Insights Into the Use of Laser-Irradiated Gold Nanoparticles. In: De Sio, L., Turmus, E.K. (eds) Biotechnology and Human Enhancement. NATO 2023. NATO Science for Peace and Security Series A: Chemistry and Biology. Springer, Dordrecht.

F. Petronella, F. Zaccagnini, M. L. Sforza, V. De Mei, L. De Sio, Bottom–Up Metasurfaces for Biotechnological Applications. *Adv. Sci.* (IF=14.1) 2025, 2413679

F. Petronella, D. De Biase, C. Santini, A. Avitabile, M. L. Sforza, F. Zaccagnini, A. d'Alessandro and L. De Sio, Logic-OR gate gold nanorod-based plasmonic biosensor for multipathogen detection and photothermal disinfection, *Materials Advances* (IF=4.7) 2025, 6, 1107

F. Zaccagnini, D. De Biase, F. Bovieri, G. Perotto, E. Quagliarini, I. Bavasso, G. Mangino, M. Iuliano, A. Calogero, G. Romeo, D. P. Singh, F. Pierini, G. Caracciolo, F. Petronella, L. De Si. Multifunctional FFP2 Face Mask for White Light Disinfection and

Pathogens Detection using Hybrid Nanostructures and Optical Metasurfaces, *Small* (IF=12.1) 2024, 2400531

M. L. Sforza, F. Petronella, D. De Biase, F. Zaccagnini, S. I. Lim, U. A. Butt, A. d'Alessandro, N. P. Godman, D. R Evans, M. McConney, K. U. Jeong, L. De Sio. Cascade Structured Plasmonic Liquid Crystal Biosensor for the Rapid Detection of Harmful Bacteria Dispersed in Potable Water, *Advanced Sensor Research* (IF=3.5) 2024, 2300201

P. Radomski, F. Zaccagnini, P. Ziółkowski, F. Petronella, L. De Sio, A. Koulali, D. Mikielewicz. Investigations of Energy Conversion and Surface Effect for Laser-Illuminated Gold Nanorod Platforms, *Energies* (IF=3.2), 2024, 17, 11, 2587

P. Ziółkowski, A. Koulali, P. Radomski, D. De Biase, F. Zaccagnini, J. Zielinski, M. Pikuła, K. Jeong, F. Petronella, L. De Sio, D. Mikielewicz, Bacterial inactivation via laser-driven gold nanoparticle heating: simulation and analysis, *Proceedings of the Thermal and Fluids Engineering Summer Conference* 2024, 715-726.

F. Petronella, D. Stoia, Y. Ziai, F. Zaccagnini, V. Scognamiglio, D. Maniu, C. Rinoldi, M. Focsan, A. Antonacci, F. Pierini, L. De Sio (2023). Plasmonic-based Biosensors for the Rapid Detection of Harmful Pathogens, *Novel Optical Materials*. December 2023, 155-194

F. Petronella, T. Madeleine, V. De Mei, F. Zaccagnini, M. Striccoli, G. D'Alessandro, M. Rumi, J. Slagle, M. Kaczmarek**,** and L. De Sio. Thermoplasmonic Controlled Optical Absorber Based on a Liquid Crystal Metasurface. *Applied Materials & Interfaces* (IF=8.2), 2023, 15, 42, 49468-49477

F. Zaccagnini, P. Radomski, M. L. Sforza, P. Ziolkowski, S. I. Lim, K. U. Jeong, D. Mikielewicz, N. P. Godman, D. R. Evans, J. E. Slagle, M. E. McConney, D. De Biase, F. Petronella and L. De Sio (2023). White light thermoplasmonic activated gold nanorod arrays enable the photo-thermal disinfection of medical tools from bacterial contamination. *Journal of Materials Chemistry B (IF=6.1)*, **11**, 6823-6836, with **front cover**.

9. Contributions to national and international conferences

F. Zaccagnini, S. Valdivieso, I. Bavasso, M. P. Bracciale, A. Tabiryan, N. V. Tabiryan, F. Petronella, L. De Sio. Development of next-generation solar cells for environmentally sustainable energy production. Poster presentation to the *SPS ARW Split 2025*, *International Workshop on Advanced Technologies and Mobile Laboratories for Countering Chemical Threats*, Hotel Radisson Blu Split, Croatia. 3-5 November 2025. https://www.fkit.unizg.hr/CroCerS/SPS_ARW_Workshop_Split2025

F. Zaccagnini, D. De Biase, V. De Mei, F. Bovieri, G. Perotto, E. Quagliarini, I. Bavasso, G. Mangino, M. Iuliano, A. Calogero, G. Romeo, D. Singh, F. Pierini, G. Caracciolo, F. Petronella and L. De Sio. Multifunctional FFP2 facemask enables pathogens detection and white light-triggered disinfection through hybrid nanomaterials. Selected for oral presentation to *Younginnovation* session in *Nanoinnovation 2025*, Faculty of Civil and Industrial Engineering, Sapienza University of Rome, via Eudossiana 18, September 15-19, 2025, https://www.nanoinnovation2025.eu/home/index.php/featured-events/younginnovation

F. Zaccagnini, D. De Biase, V. De Mei, F. Bovieri, G. Perotto, E. Quagliarini, I. Bavasso, G. Mangino, M. Iuliano, A. Calogero, G.

Romeo, D. Singh, F. Pierini, G. Caracciolo, F. Petronella and L. De Sio. Simultaneous pathogen detection and white-light disinfection in FFP2 face masks using hybrid nanomaterials. Poster presentation at *17th Mediterranean Workshop and Topical Meeting Novel Optical Materials and Applications*, Grand Hotel San Michele, Cetraro, Italy, June 08-14, 2025 with **best poster award** for the paper. https://www.nomameeting.com/index.php/noma-2025/scientific-program

Transforming healthcare through nanotechnology. Oral contribution to *Webcast di Divulgazione Ricerche Eccellenti dei Giovani della Facoltà di Farmacia e Medicina*. 31 March 2025. https://farmed.web.uniroma1.it/it/webcast-di-divulgazione-ricerche-eccellenti-trasformare-la-sanita-attraverso-le-nanotecnologie

F. Petronella, M. L. Sforza, F. Zaccagnini, A. Masi, D. D. Biase, E. D. Marinis, C. Nervi, A. d'Alessandro, L. D. Sio. Plasmonic biosensors for real-time monitoring of harmful pathogens and biomolecules, presented at 2024 IEEE Research and Applications of Photonics in Defense Conference (RAPID), 14-16 Aug. 2024.

L. D. Sio, F. Zaccagnini, F. Petronella, J. Slagle, T. Bunning. Controlling Light With Optical Metasurfaces and Chiral Liquid Crystals, presented at 2024 IEEE Research and Applications of Photonics in Defense Conference (RAPID), 14-16 Aug. 2024.

F. Zaccagnini, F. Petronella, J. Slagle, T. J. Bunning, L. De Sio. "Thermoplasmonic control of a chiral liquid crystal reflector using an array of gold nanorods".
Oral contribution to "*15th National SICL Meeting*", May 26-28, 2024, Sirolo, Ancona, Italy, https://www.sicl.it/congresso2024/program

F. Zaccagnini, D. De Biase, F. Bovieri, G. Perotto, E. Quagliarini, I. Bavasso, G. Mangino, M. Iuliano, A. Calogero, G. Romeo, D. Singh, F. Pierini, G. Caracciolo, F. Petronella, and L. De Sio. "Multifunctional FFP2 face mask for the simultaneous white light disinfection and detection of pathogens using hybrid nanostructures and metasurface-based optical absorbers".
Oral contribution to "*Plasmonica, Workshop on Plasmonics and Nano-optics*", July 10-12, 2024, Messina, Italy, https://www.plasmonica.it/2024/

F. Zaccagnini, D. De Biase, F. Bovieri, G. Perotto, E. Quagliarini, I. Bavasso, G. Mangino, M. Iuliano, A. Calogero, G. Romeo, D. Singh, F. Pierini, G. Caracciolo, F. Petronella, and L. De Sio. "Multifunctional FFP2 face mask for the simultaneous white light disinfection and detection of pathogens using hybrid nanostructures and metasurface-based optical absorbers".
Poster presentation to the workshop "*Light-responsive nanomaterials for biomedical applications*", June 3-4, 2024, Polish Academy of Sciences Scientific Center in Vicolo Doria 2, Rome

F. Zaccagnini, D. De Biase, F. Bovieri, G. Perotto, E. Quagliarini, I. Bavasso, G. Mangino, M. Iuliano, A. Calogero, G. Romeo, D. Singh, F. Pierini, G. Caracciolo, F. Petronella, and L. De Sio. "Multifunctional FFP2 face mask for the simultaneous white light disinfection and detection of pathogens using hybrid nanostructures and metasurface-based optical absorbers",
Member of the local organizing committee with Poster presentation for the *Advanced Research Workshop (ARW)*, October 3-5, 2023, San Felice Circeo (LT), Italy. https://www.arwsps2023.org/

F. Zaccagnini, D. De Biase, G. Mangino, I. Bavasso, G. Perotto, G. Caracciolo, E. Quagliarini, F. Pierini, D. P. Singh, F. Petronella and L. De Sio. "Hybrid nanostructures for white light-triggered and thermoplasmonic-based healthcare applications".

Poster presentation to "*Biophotonics at the nanoscale: from smart nanomaterials to advanced optical technologies for life, environmental science and nanomedicine*", August 26-31, 2023, Erice (TP), Italy, with **best poster award** for the paper.

F. Zaccagnini, D. De Biase, S. I. Lim, K. U. Jeong, S. Miglietta, V. Scognamiglio, N. Godman, D. R. Evans, M. McConney, F. Petronella and L. De Sio. "Gold nanorods-based biosensor with photo-responsive liquid crystals enables the detection of harmful pathogens in potable water"
Oral contribution to "*16th European Conference on Liquid Crystals*", July 10-14, 2023, Rende (CS), Italy, https://www.eclc2023.eu/index.php/program/detailed-program